ISSN 1977-5296

ESARDA

European Safeguards Research and Development Association

Bulletin

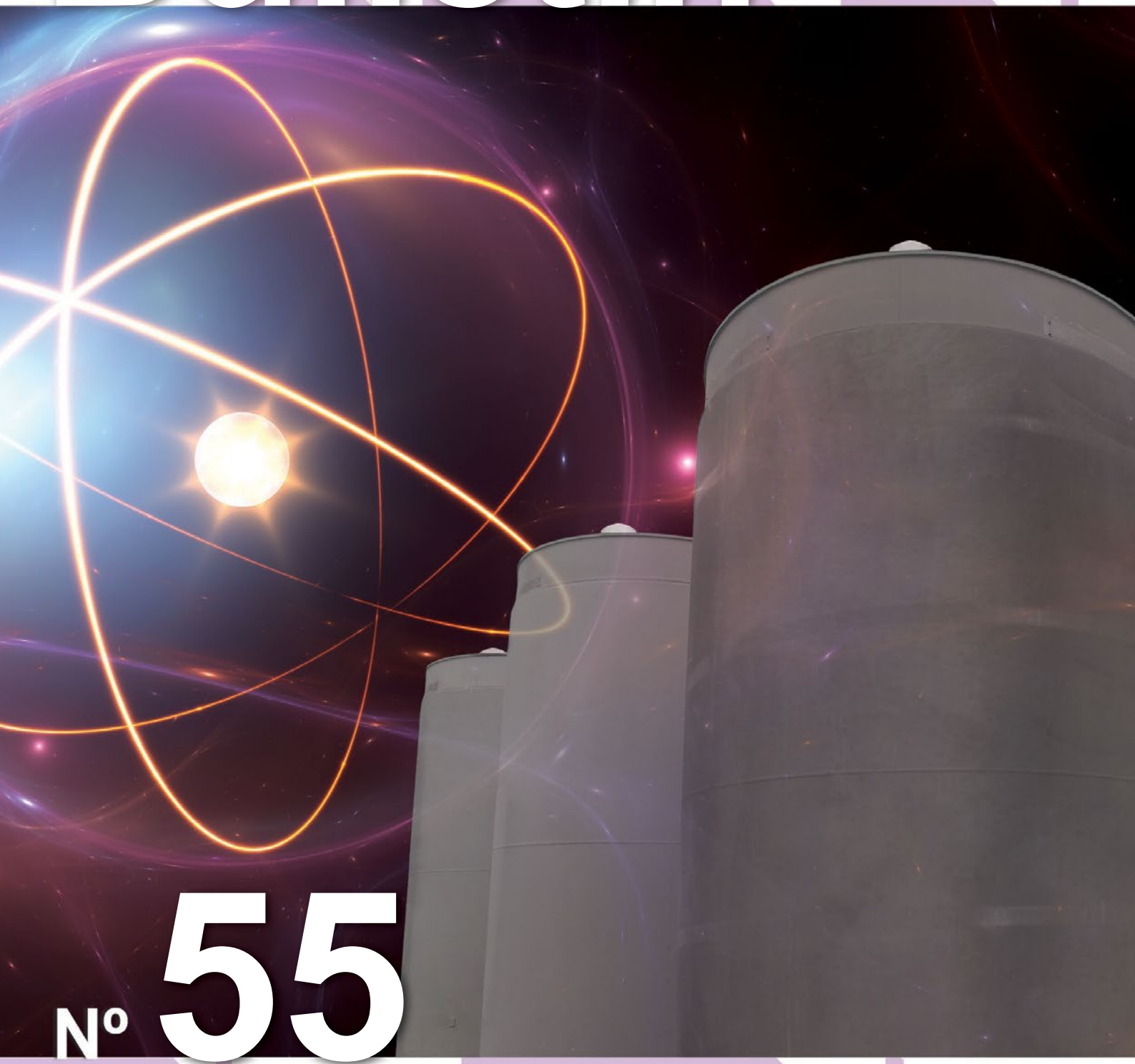

Nº 55

December 2017

ISSN 1977-5296

Number 55
December 2017

European Commission, Joint Research Centre,
ITU - Nuclear Security Unit
T.P. 800, I-21027 Ispra (VA), Italy
Tel. +39 0332-786182
EC-ESARDA-BULLETIN@ec.europa.eu
Elena Stringa@ec.europa.eu
Hamid.Tagziria@ec.europa.eu

Printed by
IMPRIMERIE CENTRALE, Luxembourg

ESARDA
European Safeguards Research and Development Association

Bulletin

Table of Content Issue n° 55

Editorial

Elena Stringa

Dear readers,

I'm pleased to provide you the 55th edition of the ESARDA Bulletin, containing some relevant papers selected by the chairpersons of the 49th ESARDA Symposium, held in Dusseldorf on May 2017, that, for editorial reasons, were not published in Issue 54. All the articles have been reviewed by at least two independent reviewers, selected from authors and expert, guaranteeing the high standard of the publication. On behalf of the Editorial Committee, I would like to thank authors and reviewers for the time and energy they have dedicated to the tasks, allowing to publish in the current Bulletin high quality articles that are of big interest to ESARDA.

After the 2016 gap, we have now started again to publish regularly the ESARDA Bulletin. Each issue will be organised in two sections: one with peer reviewed contributions, reviewed by at least two expert and independent reviewers, and a Section containing other papers that do not meet standard criteria for being peer reviewed contribution, but are relevant for the ESARDA community.

I encourage ESARDA researchers to publish their work any time so that all the ESARDA community can benefit from the latest relevant research novelties. In order to submit a contribution you are kindly asked to follow the instructions reported in the ESARDA website. At the moment, we are collecting articles for the ESARDA Bulletin n. 56 (June 2018). In occasion of the ESARDA working group meeting held in November 2017 in Ispra, a big interest on the topic related to encapsulation plants and geological repositories emerged from several working groups' presentations. Given the interest and the need of exchanging updates on encapsulation plants and geological repositories, in issue 56 priorities will be given to contributions dealing with this topic but also articles on different topics are very welcome. The deadline to submit contributions to appear in Issue 56 is February, 7th, 2018: we are looking forward to receive the results of your highly appreciated work.

I would like to use this opportunity to introduce new members of the Editorial Board: Irene Popovici, senior expert at the National Commission for Nuclear Activity Control (CNCAN Romania) and Joshua Rutkowsky, researcher in the International Safeguards Group, Institute of Energy and Climate Research at Forschungszentrum Jülich, Germany: thank you very much for your interest and willingness to maintain and increase the quality of the ESARDA publications. Irene and Joshua replace Paolo Peerani and Eileen Radde, who could not continue to be part of the Editorial board due to professional reasons: we are grateful for the good work that Paolo and Eileen carried out for the ESARDA bulletin and we wish them all the best in their new job positions.

I am very pleased to remind you of the following ESARDA events coming in spring 2018:

- The 17th ESARDA Course on Nuclear Safeguards and Non Proliferation will be held on 9-10 April 2018, at the Joint Research Centre, Ispra (Italy). Information can be found in the ESARDA website (https://esarda.jrc.ec.europa.eu) under the ESARDA course section
- The ESARDA Non-Destructive Assay (NDA) Working Group is organising an international workshop on the topics of computer simulation applied to the modelling of NDA instrumentation and methods for nuclear safeguards applications. The workshop will be held on 17-18 May at Euroforum Complex in Luxembourg City. Detailed information are reported in the 'Other events' section of the ESARDA website

Regarding the ESARDA website, on behalf of the Editorial Board, I would like to address sincere thanks to Andrea De Luca, webmaster and essential assistant for the ESARDA Bulletin preparation: thank you very much for your engagement, for the pertinent suggestions and fruitful ideas in supporting our work.

I wish you all a successful, fruitful and happy 2018.

Dr. Elena Stringa
Editor and member of the Editorial Committee

https://esarda.jrc.ec.europa.eu/
ec-esarda-bulletin@ec.europa.eu
Elena.Stringa@.ec.europa.eu

Hybrid Gamma Emission Tomography for the Verification of Unirradiated Fuel: A Viability Study

E.A. Miller[1], L.E. Smith[1], V. Mozin[2], R.S. Wittman[1], L.W. Campbell[1], M.A. Zalavadia[1], N.S. Deshmukh[1]

[1] Pacific Northwest National Laboratory
[2] Lawrence Livermore National Laboratory

Abstract:

Current International Atomic Energy Agency (IAEA) methodologies for the verification of fresh low-enriched uranium (LEU) and mixed oxide (MOX) fuel assemblies are volume-averaging methods that lack sensitivity to individual pins. Further, as unirradiated fuel assemblies become more and more complex (e.g., heavy gadolinium loading, high degrees of axial and radial variation in fissile concentration), the accuracy of current IAEA instruments degrades and measurement time increases. Particularly in light of the fact that no special tooling is required to remove individual pins from modern fuel assemblies, new capabilities for the verification of unirradiated (i.e., fresh LEU and MOX) assemblies are needed to ensure that fissile material has not been diverted. Passive gamma emission tomography has demonstrated potential to provide pin-level verification of spent fuel, but gamma-ray emission rates from unirradiated fuel emissions are significantly lower, precluding purely passive tomography methods. The work presented here introduces the concept of Hybrid Gamma Emission Tomography (HGET) for verification of unirradiated fuels, in which a neutron source is used to actively interrogate the fuel assembly and the resulting gamma-ray emissions are imaged using tomographic methods to provide pin-level verification of fissile material concentration. This paper describes the status of a viability study on the HGET concept, including: envisioned use-case scenarios and corresponding definitions of fuel assemblies; modeling framework based on Monte Carlo and deterministic transport methods, and its validation; quantitative assessment of candidate HGET signatures with a focus on prompt fission gamma rays and delayed fission gamma rays; a nominal HGETv1 instrument design; candidate HGET-specific tomographic reconstruction methods that fully incorporate declared information; and examples of simulation-based predictions of HGET performance.

Keywords: safeguards; fuel verification; gamma emission tomography

1. Introduction

Current IAEA methodologies for the verification of fresh LEU assemblies at fuel fabrication facilities utilize active neutron interrogation with neutron coincidence counting; verification of fresh MOX fuel utilizes passive neutron coincidence counting with gamma-ray spectroscopy for Pu isotopics. These volume-averaging methods are not capable of individual-pin sensitivity and as fuel assemblies become more complex (e.g., heavy gadolinium loading, and axial variation in boiling water reactors [BWRs]), their accuracy degrades and measurement times increase. Particularly in light of the fact that no special tooling is required to remove individual pins from modern fuel assemblies, the IAEA needs new capabilities for the verification of unirradiated fuel assemblies that can provide high-precision fissile-mass quantification, ideally at the single-pin level. The IAEA has documented the need for new unirradiated-fuel verification tools in the IAEA Department of Safeguards Long-Term R&D Plan [1]. Other potential users of a new fuel verification tools include EURATOM, and State regulators.

Passive gamma-ray emission tomography (GET) is a promising candidate for verification of item integrity in fuel assemblies because it has the potential to directly image the spatial distribution of the active fuel material, without the need for operator-declared information [2]. In this sense, it is an absolute, rather than comparative verification method. In addition, the relative intensity of gamma-ray signatures can be used to verify declared attributes on a pin-by-pin basis (e.g., burnup in irradiated fuels; uranium enrichment or plutonium isotopics in unirradiated fuels). The viability of GET for the detection of missing pins in irradiated fuels, where relatively intense, higher-energy gamma emissions are available, appears promising based on findings of a recent IAEA study [3] and ongoing testing of a prototype passive GET instrument by the IAEA.

For unirradiated fuels with relatively weak and lower-energy emissions, the ability to see interior pins with purely passive tomography is less clear. The use of active neutron interrogation to stimulate gamma-ray emission can provide additional signal intensity for emission tomography, here referred to as Hybrid Gamma Emission Tomography (HGET). There are several candidate signatures for hybrid (i.e., tomographic imaging of an active interrogation signature) assay of unirradiated fuels, including prompt capture gamma rays in the isotopes of interest (e.g., 1.28 MeV from ^{235}U); prompt fission gamma rays (continuum peaked at ~ 1 MeV); and delayed gamma rays from short-lived fission products (discrete lines generally from 1 to 7 MeV).

Each of the candidate signatures above has been studied previously, and sometimes in combination, for the assay of both irradiated and unirradiated fuels. For example, delayed-gamma methods have been studied for the direct assay of fissile isotopes in irradiated fuels [4, 5], but the delayed-gamma methods studied to date provide no spatial information about the origin of the signatures and therefore, localized neutron moderation effects and self-attenuation can produce biases in fissile isotope quantification. In addition, the high passive background in spent fuel forces the use of only the higher-energy (> 3 MeV) delayed-gamma signatures, while the most intense signatures are presented at lower energies. In unirradiated fuels, these more-intense, lower-energy delayed-gamma signatures are accessible, but information about their location of origin in the fuel assembly is needed.

To the authors' knowledge, no prior work has demonstrated the ability to provide spatial information about the origin of the candidate signatures and therefore, verify fuel characteristics at the pin level. In the HGET concept, it is postulated that the collection of these candidate signatures through a tomographic lens will support pin-by-pin verification of fissile materials in the assembly.

Here we describe an ongoing modeling-based viability study of the HGET concept. This paper discusses potential IAEA use cases and implementation approaches, a novel method for modeling instrument response that couples Monte Carlo and deterministic transport methods, candidate signatures, and a method for extracting fissile isotope concentrations on a pin-by-pin basis. Example results for pin-level verification of fissile isotope concentrations in MOX fuel assembly are presented. The paper concludes with a discussion of the ongoing and planned analyses that are needed to more fully assess the viability of the HGET concept for safeguards verification.

2. Potential Use Cases in International Safeguards

The use case for an HGET instrument by safeguards inspectorates is presumed to be consistent with how current IAEA instrumentation is used for the verification of unirradiated fuels. For fresh LEU fuel, the IAEA uses the Uranium Neutron Coincidence Collar (UNCL); for MOX fuel the Passive Neutron Coincidence Collar (PNCL). Both instruments use neutron coincidence signatures to verify the total uranium or plutonium in the assembly--additional information about each method can be found in [6], with IAEA's International Target Values (ITVs) for verification of unirradiated assemblies in [7].

For fresh LEU fuel, the UNCL is used to measure the mass density of ^{235}U at a given axial location of the assembly. It is assumed that the ^{235}U is the only fissile isotope in the assembly and therefore, that all induced fission comes from ^{235}U. This localized ^{235}U mass density is translated to total ^{235}U mass for the assembly using an active length measurement (e.g., gamma scanning). The ITV for determination of total ^{235}U mass in an LEU assembly is 4.5% (one-sigma relative), assuming relatively low gadolinium (Gd) content. Count times are not specified in the ITV document, but other reports indicate thatfor fuels with Gd, count times for UNCL can approach one hour to reach the desired statistical uncertainty. Systematic uncertainties for high-Gd assemblies can be 10 or more times higher [8].

For MOX fuel, the PNCL is used to measure the mass density, at a given axial location, of the Pu isotopes with appreciable spontaneous fission yields (^{240}Pu dominates). High-resolution gamma-ray spectroscopy on exterior pins of the assembly is then used to infer the linear density of total Pu. An active length measurement (e.g., gamma scanning) is employed to translate that value to total Pu for the assembly. The ITV for determination of total Pu mass in a MOX assembly is 3.2% (one-sigma relative).

The use cases and ITVs for UNCL and PNCL provide useful context for the HGET viability study, and are the basis for the assumptions that were adopted to guide the first phase of this study:

- Verification of unirradiated fuel will occur in an air environment and the operator will position the fuel assembly in such a way that the HGET collar will assay one or more vertical segments of the assembly. As with UNCL and PNCL, it is assumed that some form of active-length measurement will inform the translation from the HGET-measured ^{235}U and total Pu linear densities to a ^{235}U and total Pu assembly mass value. Note that the HGET gamma-spectrometer array, operating in purely passive mode, could provide an active-length measurement similar to what is performed today using a handheld gamma-ray detector. (This assumes that the operator moves the fuel assembly through the HGET collar.)
- Total measurement time for HGET verification of unirradiated fuel assemblies should be on the order of 1-2 hours. While today's measurements may be shorter in duration for many fuel types, the fact that HGET will provide pin-by-pin verification of fissile content encourages a broader window of assay-time acceptability for the first phase of the study.
- The physical dimensions and mass of HGET should be comparable to existing IAEA instruments: for example, the JCC-71 PNCL/UNCL instrument sold by Canberra weighs approximately 40 kg [9]. A maximum neutron moderator/reflector weight of 100 kg was enforced during the design study, on the logic that this represented a reasonable size for a mobile instrument deployed at a fuel fabrication or reactor facility.

3. MOX Fuel Assembly as Initial Case Study

While the HGET study is also investigating low-enriched uranium (LEU) fuels with and without burnable poisons, an initial use case was defined for a pressurized water reactor (PWR) assembly of 17x17 pins with mixed oxide (MOX) fuel. PWR fuel is at the more-challenging end of the continuum of fuel types under safeguards in terms of neutron and gamma-ray attenuation, due to its relatively dense pin-array geometry and overall large dimension. The age since separation for the reactor-grade Pu was assumed to be 5 years, an upper limit in terms of occupational health hazards (after about 5 years enough ^{241}Am has grown in to make handling difficult; this process has little impact on the amount of fissionable material for the HGET measurement), and the composition is shown in Table 1.

Generally speaking, the composition of MOX fuel pins varies with pin position. An IAEA technical report, provides Pu concentrations of each pin type in an example MOX assembly, as shown in Figure 1 [10]. Note that the overall Pu concentration varies from pin to pin but the relative Pu isotopics, as defined in Table 1 is consistent across all pins.

		MOX	LEU
Atom	Isotope	Atom Fraction (X3)	Atom Fraction (X3)
U	234	5.20×10^{-5}	3.12×10^{-3}
U	235	6.81×10^{-4}	4.05×10^{-2}
U	238	9.39×10^{-1}	9.60×10^{-1}
Pu	238	1.36×10^{-3}	
Pu	239	3.21×10^{-2}	
Pu	240	1.52×10^{-2}	
Pu	241	7.06×10^{-3}	
Pu	242	4.21×10^{-3}	
O	16	2	2
	density (g/cc)	10.4538	10.4538

Table 1: Initial composition (before decay) of the fuel assembly definitions used in the HGET viability study (atom fractions displayed are 3x the total atom fraction, such that the U/Pu isotopes add to approximately 1).

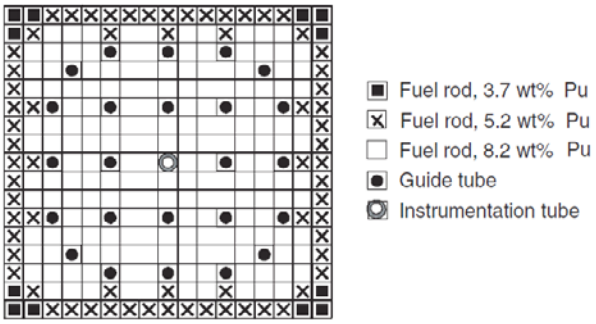

Figure 1: PWR MOX assembly design of the 17x17—24 type with assembly averaged plutonium concentration of 7.2 wt% Pu. (From [10])

4. Overview of HGET Modeling Methods

An overview of the HGET modeling methods is given in Figure 2 below. Neutron transport was performed using MCNP6 and the calculated fission rates in the fuel pins were used to generate the prompt- and delayed-gamma source terms. Those gamma-ray source terms were then used as input to a separate calculation for the transport of the photons out of the assembly and into the detector. Gamma-ray transport through a highly attenuating assembly can be prohibitively time-consuming with pure Monte Carlo methods. The gamma-ray transport was performed using a deterministic transport by the discrete-ordinates package Attila [11]. More detail on the HGET modeling method and validation can be found in [12].

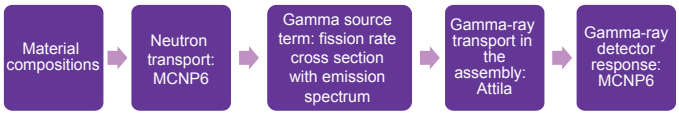

Figure 2: Schematic of HGET modeling approach for modeling neutron-induced gamma-ray signatures and detector response functions.

5. Candidate HGET Signatures

Gamma emission tomography is based on detecting gamma emissions selectively, sensitive to both their location and their angle of incidence. Detection of inner pins can be very difficult, since radiation from these pins must pass through a considerable distance of dense fuel. Gamma rays with energies of less than 500 keV have a very low probability of escaping from inner pins to the outside. Penetration increases with increasing energy to a broad maximum at around 3 MeV to 4 MeV, beyond which the pair production mechanism of absorption causes penetration to decrease. Isotopic specificity is also desirable; if a gamma-ray emission is uniquely tied to a given isotope (e.g., fissile isotope or fission product), it will likely be more useful in characterizing the fissile content of the assembly. Finally, methods based on excessively complex signatures may be difficult to implement, limiting their utility.

An order-of-magnitude comparison of typical spent-fuel assay signatures, to the candidate signatures for HGET assay of a nominal MOX fuel assembly is given in Table 2. The actively induced count rates were estimated using the neutron-gamma modeling methods described in the previous section, and the nominal HGETv1a design described later that employs a commercial, off-the-shelf deuterium-tritium (D-T) neutron generator producing approximately 10^8 n/s at 14.1 MeV.

Technique	Emission rate (γ/pin/cm/s)
Spent fuel, 1 year CT, ^{154}Eu 1274 keV	1 x 10^{8}
Spent fuel, 30 year CT, ^{137}Cs 662 keV	5 x 10^{9}
^{239}Pu 414 keV	5 x10^{3}
Prompt fission > 1000 keV	1 x10^{4}
Delayed gamma individual lines	< 2 x10^{1}
Delayed gamma at 1 s, > 1000 keV	4 x 10^{2}
Delayed gamma at 1000s, > 1000 keV	5 x 10^{3}
Prompt capture gamma, U	Uncertain, ~1 x10^{2}
Prompt capture gamma, Pu	<1 x10^{3}
Activation gammas > 500 keV	Uncertain, small

Table 2: Order-of-magnitude comparison of signal intensities from passive tomography of PWR spent fuel variants (top three entries) and HGET for unirradiated MOX fuel. HGET signatures highlighted in gray are the most promising in terms of absolute emission intensity.

Clear from Table 2 is that the passive Pu emissions from unirradiated MOX fuel are many orders of magnitude less than from spent fuel, and have low penetrating power. The actively induced signatures offer somewhat higher intensities and importantly, their higher energies offer the promise of greater penetrability through the fuel assembly. Delayed gamma signatures are more complex, due to their time dependence, and no individual lines are observed with sufficiently high emission intensity for tomography. It is possible that a delayed gamma-ray signature summed over broad energy windows could be imaged – but fissile-isotope specificity would be lost. The assay of other activation products to infer fuel composition offers little promise both because of low intensity and limited direct connection to the fissile material that is the focus of IAEA verification. Given that no isotope-specific signatures are high enough in intensity for direct fissile isotope assay, the most useful signature for verifying the integrity of fuel assemblies and total fissile content appears to be the prompt fission gamma rays, possibly in combination with the delayed gamma rays. The relatively high production of these signatures at energies above 1 MeV is key, although still four orders of magnitude below emission rates typical of spent fuel.

This large gap in emission intensity points to the need for the development of HGET-specific tomographic designs and methods, for example neutron moderation and reflector designs that are efficient for inducing fission in the assembly, detector and collimator designs that balance gamma-ray collection efficiency with spatial resolution for imaging, and tomographic reconstruction methods that wring as much information as possible from the collected data by relying heavily on the declared, *a priori* information about the pin assembly geometry. These topics are discussed in the sections below.

6. Nominal HGET Design

A wide range of source/moderator/reflector designs and materials (e.g., poly, graphite, hydrided DU) were considered in the early stages of the HGET v1 design study. Both a D-D and a D-T neutron generator were considered; the lower energy neutrons from D-D produce a smaller background of ^{238}U fissions but D-D generators are generally significantly lower in achievable intensity, given similar form factors. The metrics for evaluating the various designs were: 1) uniformity of thermal and epithermal flux across the assembly cross-section, 2) total fission rate induced in the MOX fuel definition, and 3) relative contributions of fissile and ^{238}U fission. Several of the early designs were discarded based on these metrics; Figure 3 (left) depicts the design that demonstrated considerable promise: HGET-v1a. Figure 3 (right) shows the low-energy fission rate distributions for the HGETv1a designs, with an assembly present (each pixel in the image corresponds to an individual pin). Immediately evident is a relatively high fission rate on the generator side of the assembly, in the outer row of pins. The neutron self-shielding effect, which depresses the fission rate on the interior of the assembly due to interactions between the neutrons and the fuel pins, is also clear. The overall effect is a gradient of approximately 10X between the fission rates at the outermost to innermost pins – although if the outer row of pins is neglected, the fission rate in the rest of the assembly is within a factor of ~3X and has a predictable gradient structure, with no highly localized changes on the interior of the assembly.

For the collection of the prompt and delayed gamma rays produced by the induced fissions, an array of highly collimated gamma detectors is rotated around the assembly to build up the tomographic projection data, as a function of both energy and angle. A number of potential collimator/detector combinations are possible, but the nominal HGET design assumes a configuration founded on the IAEA's original Passive Gamma Emission Tomographer (PGET), as described more fully in [3] and depicted in Figure 4 below. Though PGET is intended for verification of spent fuel, a variant on PGET tailored for unirradiated fuels would benefit from a high degree of familiarity among tomography practitioners and the potential for leveraging of hardware components (e.g., detector arrays, pulse-processing electronics).

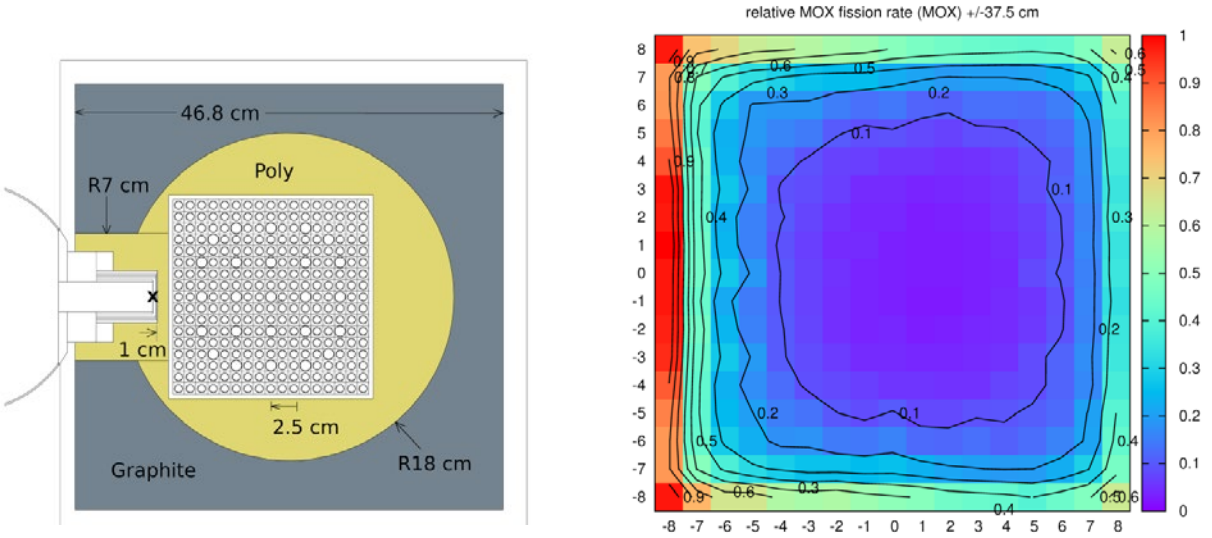

Figure 3: Left: Cross-section of the HGETv1a instrument geometry including a D-T generator (far left, with neutrons generated at the location of the x), a PWR assembly, and a combination of poly and graphite moderator/reflector. Right: Mapping of fission rate induced by low-energy neutrons, assuming the HGETv1a design (each pixel represents one fuel pin).

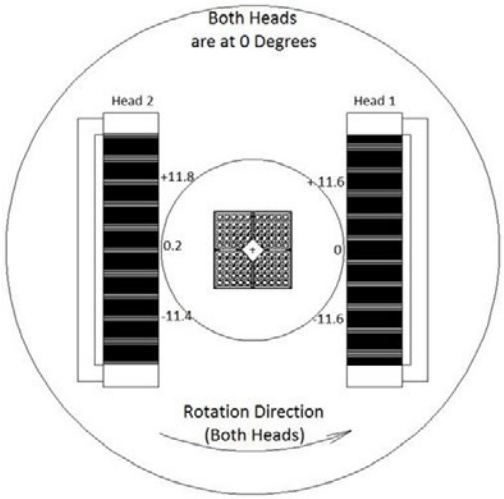

Figure 4: Rendering of the IAEA's PGET instrument design showing a vertical view of the detector heads containing 104 CdTe detectors in each head [3].

The central challenge in designing the HGET collimator/detector combination is to increase the collection efficiency significantly while preserving sufficient spatial resolution to resolve individual pins. To increase the collection efficiency for HGET gamma-ray signatures, the aperture's field of view was opened significantly in the horizontal and vertical directions. These adaptations produce an increase in the count rate at the detectors of approximately 30X compared to the PGET collimator.

The initial feasibility studies focused on a nominal design where the neutron generator and the gamma detectors lie in the same plane. Tests were also performed with designs that split the neutron reflector and placed the gamma detectors and staging in between, and with a stacked design with gamma detectors on a plane beneath the neutron reflector; both these configurations will result in lower count rates at the detector. An optimized design is expected to be intermediate between the ideal case shown here and the non-optimized tests.

$Bi_4Ge_3O_{12}$ (BGO) was chosen as the nominal gamma-ray spectrometer material for the HGETv1a design. Although it has significantly poorer energy resolution than other candidates such as NaI(Tl), CZT or $LaBr_3$, energy resolution is not expected to be critical for the broad energy windows for collection of prompt-fission and delayed-gamma signatures. BGO's high density and atomic number translate to high stopping power for higher-energy gamma rays, whilst maintaining a relatively small form factor that can support a highly arrayed detector arrangement like the one used in PGET. Importantly, BGO is a very common material for positron emission tomography systems used in nuclear medicine, which means that large arrays of relatively small voxels are readily available in the commercial market. The BGO detector is observed to give a factor of three improvement in intrinsic efficiency for the collection of gamma-rays above 1 MeV, when compared to the CdTe detectors employed in the original PGET device.

The combination of higher collimator efficiency (~30 X) and greater intrinsic detector efficiency (~3X) results in an overall HGET gamma-ray collection efficiency that is approximately two orders of magnitude higher than the original PGET design, thereby helping to recover a significant portion of the signal discrepancy (several orders of magnitude) between the spent fuel applications for which PGET was originally designed and the HGET scenarios for unirradiated fuels.

7. Reconstruction and Analysis Methods for HGET

The simplest approach to tomographic reconstruction is filtered backprojection, which solves analytically for the distribution of emissions, assuming that measurements are spaced at equal angles and that attenuation is minimal. This approach has the advantage of being both fast and requiring few assumptions about the system [13], and has been successfully used to locate missing pins in spent nuclear fuel [3]. However, since FBP in its simplest form makes no assumptions about attenuation, it cannot correct for the highly attenuating pins that block emissions from the center of the assembly. This leads to a reconstructed image which is systematically lower in intensity inside the assembly.

The case of fresh fuel is different from the spent fuel application in two important ways. First, the emission intensity is much lower, as previously noted. Second, emission intensity is a function not only of fuel composition, but also of illumination by the neutron field. Achieving a high and relatively uniform flux of thermal neutrons in the center of a large assembly is difficult, as discussed previously. The difference in counts at the detector from inner pins to outer pins is already large in passive emission tomography, but neutron interrogation adds another significant gradient, on the order of 10X, between inner and outer pins. Reconstructing a dataset with such an extreme gradient results in poor image quality.

While the HGET application is challenging from the reconstruction standpoint, it is decidedly different from other tomographic applications (e.g., nuclear medicine) in that it is fundamentally a confirmatory measurement of the operator's declaration about the assembly (as opposed to a blind test in which nothing about the object is known). This means that *a priori* information about a declared assembly, perhaps after initial verification via FBP, can be used to extract as much information as possible from each collected gamma ray and thereby improve the quality of the resulting image reconstruction. There are a number of ways to incorporate this information, but one straightforward approach is to assume a declared assembly geometry and solve for average emission values for each pin. Mathematically, this is phrased as measurement data (g_α) with α as the sinogram angle/offset index according to

$$g_\alpha = \sum_k H_{\alpha k} f_k \tag{1}$$

where f_k is the reconstructed activity estimate, here with k as the pin index, and $H_{\alpha k}$ is the model-based system response matrix, in this case the detector response to each possible emitting pin in the presence of attenuation due to the whole assembly. This approach is described more fully in [3][12]. Reconstructing at the level of individual pins, rather than over a series of pixels, incorporates the assembly geometry and greatly decreases the number of unknowns, regularizing the inverse problem. This results in much lower relative statistical error, but contingent upon the accuracy of the model.

The model-based tomographic reconstruction methods translate the collected gamma-ray signature into the emission intensity of prompt and delayed fission gammas in each pin, and therefore the pin-wise fission rate. Next, the pin-by-pin fission rate produced by the tomographic inverse problem must be translated to the verification parameter of interest: fissile-material concentration. De-tangling the fissile concentration from the fission rate must recognize that fission from non-fissile isotopes, most notably ^{238}U, can contribute significantly to the total induced fission rate, but the concentration of the non-fissile isotopes is not the IAEA verification parameter of interest. Such a translation can be complex since the fission cross-sections for the fissile and fissionable isotopes are highly dependent on incident neutron energy (including resonance structures and threshold reactions), and the neutron energy spectrum varies by pin location—due to attenuation from surrounding pins and attenuation within the pin of interest due to its own fissile loading. The methods used to translate total fission rate in a pin into fissile-isotope concentrations in that pin are beyond the scope of this paper but are described fully in [12].

8. Example Performance Prediction Results

In the early rounds of performance prediction studies, only the prompt-fission gamma-ray signal has been considered, and a straightforward model-based reconstruction on a pin-by-pin basis was used to bound the tomography inversion problem. The primary question to be addressed was: Based on the HGET v1a design, the "MOX A" assembly definition, anticipated operator declarations, and simulated prompt-gamma signatures, can reasonable statistical uncertainties be achieved for fissile-mass concentration on a pin-by-pin basis within 1-2 hours? The end-to-end HGET analysis process is shown in Figure 5 for this MOX A case study and reflects the discussions in the previous sections of this paper. In the example case-study results presented in Figure 6, it is assumed the operator declares the Pu isotopics for each pin.

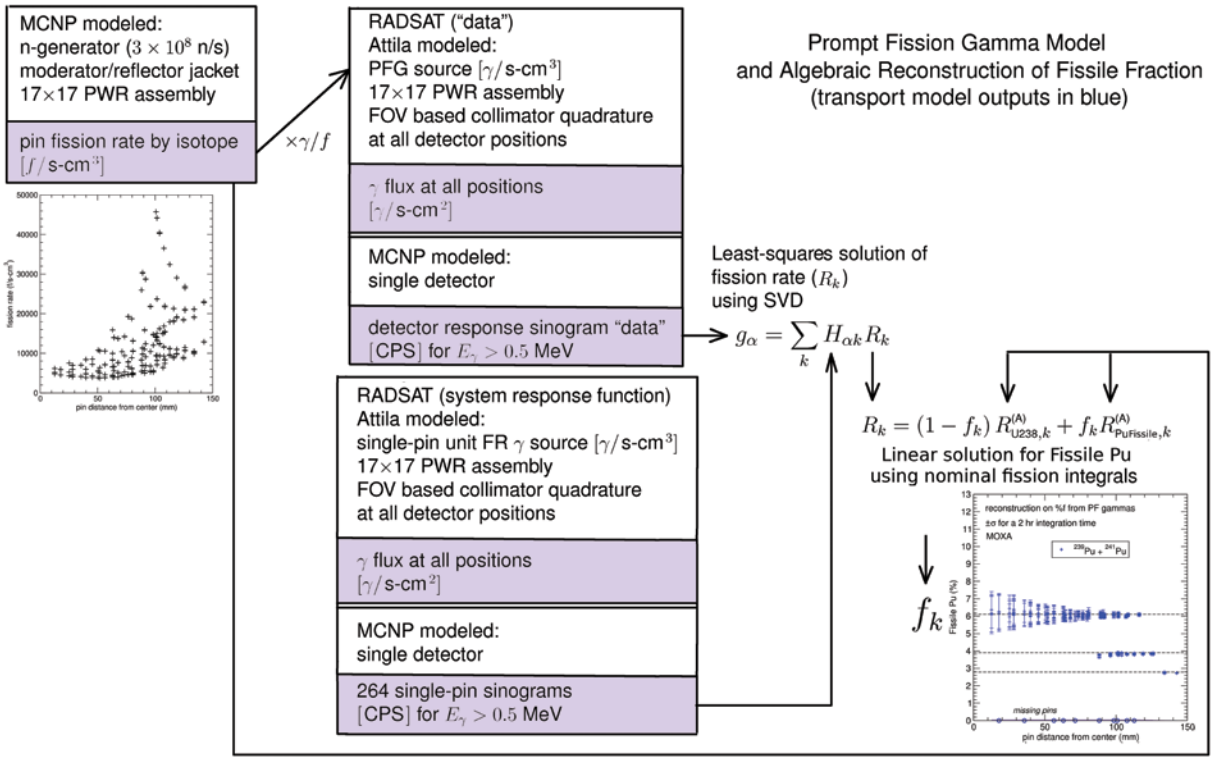

Figure 5: Overview of HGET performance-prediction methodology (assuming a PWR MOX assembly) that begins with forward calculations of induced fission rate (upper left) and culminates in quantification of fissile Pu concentration in each pin (lower right). Starting from left, MCNP calculates pin fission rates by isotope, which is used as a source term for gamma transport models (top center) and for interpreting pin-by-pin fission rates as fissile isotope fractions f_k (bottom right). Top center: sinogram data as a function of lateral position and angle g_α is calculated in counts per second (CPS) using RADSAT. Bottom center: RADSAT is used to calculate a pin-by-pin system response function using unit fission rates (FR) and a monte carlo detector response function (DRF). Singular value decomposition (SVD) is used to provide a least squares solution to invert the transport equation and recover individual pin fission rates R_k, which in turn provide fissile isotope fractions in each pin.

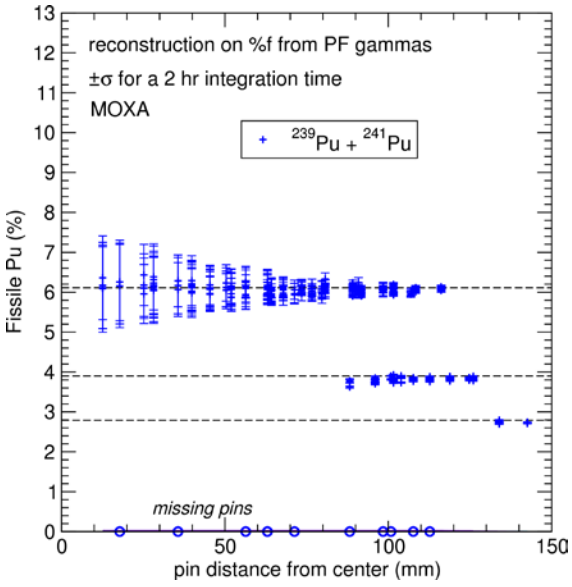

Figure 6: Example results for the determination of Fissile Pu (^{239}Pu + ^{241}Pu) fraction in MOX A, when incorporating assembly geometry and Pu isotopics data in the analysis process. This simulated assembly excluded 11 pins at different lattice positions from the middle to the edge of the assembly. Calculated values are based on 2-hour total assay time; one-sigma error bars on statistical uncertainty are shown. Dashed lines are the actual fissile fraction (^{239}Pu + ^{241}Pu) for the three Pu loading levels. (Note that Pu isotopics are identical for all loading levels; given the correct isotopic composition these numbers are equivalent to the wt% quoted in Fig. 1).

The preliminary results shown in Figure 6 indicate that: given a careful system design, a COTS portable neutron generator and reconstruction and analysis algorithms that fully acknowledge operator-declared information about the assembly, HGET has the potential to verify fissile-mass concentration on a pin-by-pin basis in total assay times of approximately 2 hours for a representative PWR MOX assembly. These initial performance estimates assumed that assembly type, missing-pin locations and Pu isotopics were accurately declared by the operator and incorporated in the analysis process. Under those assumptions, the relative standard deviation of the fissile-Pu quantification was less than a few percent for most pins, but approached 20% for the interior pins. The uncertainty in fissile concentration is small compared to the reconstructed contrast for the 11 missing pins.

9. Summary and Next Steps

While the initial HGET performance predictions presented in this paper are encouraging, further investigation is required to fully establish feasibility. From an operational standpoint, a neutron generator with 3 x 10^8 n/s is much higher flux than Am-Li sources currently used for active coincidence counting – typically 10^4 – 10^6 n/s [14]. This

raises concerns for exclusion area needed during a measurement. The measurement will induce some additional radioactivity in the assembly, although preliminary results indicate that the induced activity should be small relative to the original assembly activity. From a technical standpoint, the results here were generated using simulated data that does not include background terms, assuming full availability and accuracy of declared data for the assembly of interest, and assuming a near-perfect system response function in the tomographic reconstruction. Considerably more analysis is needed to more fully understand the potential of HGET and its viability for IAEA verification scenarios. The highest priority is the extension of the feasibility analysis to LEU, and to LEU with burnable poisons (Gd rods). The case of Gd loading in particular is challenging for coincidence counting assay, and the possibility of using the high-energy and high-intensity gamma rays from Gd to account for the burnable poisons offers potential advantages for HGET in overcoming the burnable poison effects. The performance predictions presented here were performed using only the prompt-gamma signature but delayed-gamma signatures become significant as the active-interrogation measurement progresses, and could be included in the reconstruction algorithms as a smoothly varying time dependent term. Continued study of HGET-specific reconstruction algorithms, particularly those that can identify the perturbation patterns created by missing pins and have robustness to imperfections in the system response function (e.g., undeclared or inaccurately declared missing pins), is needed. Perhaps most importantly, the HGET viability study needs to move into empirical space. The challenges of high-fidelity simulation for this relatively complex active interrogation approach (for which even basic cross-section data are not always available), and the inability of simulations to accurately capture the background terms that may arise in this active-interrogation scenario, strongly encourage proof-of-principle laboratory measurements using a representative tomographic device and objects (e.g., LEU fuel rodlets), to benchmark the predictive modeling tools and guide refinement of the nominal HGET instrument design.

10. References

[1] IAEA: Vienna, Austria; *IAEA Department of Safeguards Long-Term R&D Plan, 2012-2023*. 2013.

[2] Svard, S.J., et al., *Gamma-ray Emission Tomography: Modeling and Evaluation of Partial-Defect Testing Capabilities*, in *2014 IAEA Symposium on International Safeguards*. 2014.

[3] Smith, L.E., et al., *A Viability Study of Gamma Emission Tomography for Spent Fuel Verification: JNT 1955 Phase I Technical Report*. 2016, Pacific Northwest National Laboratory: Richland, WA. p. 197.

[4] Campbell, L.W., L.E. Smith, and A.C. Misner, *High-Energy Delayed Gamma Spectroscopy for Spent Nuclear Fuel ASsays.* IEEE Transactions on Nuclear Science, 2011. **58**(1).

[5] Mozin, V., et al., *Delayed gamma-ray spectroscopy for spent nuclear fuel assay.* Journal of Nuclear Materials Management, 2012. **40**(3): p. 78-87.

[6] *Safeguards Techniques and Equipment: 2011 Edition*, in *International Nuclear Verification Series*. 2011: Vienna, Austria. p. 162.

[7] Zhao, M., et al., *International Target Values 2010 for Measurement Uncertainties in Safeguarding Nuclear Materials.* ESARDA Bulletin, 2012. **48**: p. 3-24.

[8] Menlove, H.O., et al., *Neutron Collar Calibration and Evaluation for Assay of LWR Fuel Assemblies Containing Burnable Neutron Absorbers*, Los Alamos National Laboratory, LA-11965-MS, 1990.

[9] Canberra Industries, I. 2011 [cited 2016 December 1]; Available from: http://www.canberra.com/products/waste_safeguard_systems/pdf/JCC-71-72-73-SSC38898.pdf.

[10] Bairiot, H., et al., *Status and Advances in MOX Fuel Technology*, in *Technical Reports Series*. 2005, International Atomic Energy Agency: Vienna, Austria. p. 179.

[11] Wareing, T.A., J.M. McGhee, and J.E. Morel, *ATTILA: A Three-Dimensional, Unstructured Tetrahedral Mesh Discrete Ordinates Transport Code.* Transactions of the American Nuclear Society, 1996. **75**.

[12] Miller E A,Smith L E,Wittman R S,Campbell L W,Deshmukh N S,Zalavadia M A,Batie M A,Mozin V V . *Hybrid Gama Emission Tomography (HGET): FY16 Annual Report,* Pacific Northwest National Laboratory, PNNL-26213, 2017..

[13] *Emission Tomography: The Fundamentals of PET and SPECT*. Miles N. Wernick and John N. Aarsvold, ed. 1st ed. 2004: Elsevier Academic Press. 576.

[14] Reilly, Doug, et al., *Passive Nondestructive Assay of Nuclear Materials*, United States Nuclear Regulatory Commission, NUREG/CR-5550, LA-UR-90-732, 1991.

Outcomes of the JNT 1955 Phase I Viability Study of Gamma Emission Tomography for Spent Fuel Verification

S. Jacobsson Svärd[1], L.E. Smith[2], T.A. White[2,7], V. Mozin[3], P. Jansson[1], P. Andersson[1], A. Davour[1], S. Grape[1], H. Trellue[4], N. Deshmukh[2], E.A. Miller[2], R. S. Wittman[2], T. Honkamaa[5], S. Vaccaro[6], J. Ely[7]

1 Uppsala University, Uppsala, Sweden
2 Pacific Northwest National Laboratory, Richland, WA, USA
3 Lawrence Livermore National Laboratory, Livermore, CA, USA
4 Los Alamos National Laboratory, Los Alamos, NM, USA
5 STUK – Radiation and Nuclear Safety Authority, Helsinki, Finland
6 European Commission, Directorate General Energy, Directorate Euratom Safeguards, Luxembourg
7 International Atomic Energy Agency, Vienna, Austria

Abstract:

The potential for gamma emission tomography (GET) to detect partial defects within a spent nuclear fuel assembly has been assessed within the IAEA Support Program project JNT 1955, phase I, which was completed and reported to the IAEA in October 2016. Two safeguards verification objectives were identified in the project; (1) independent determination of the number of active pins that are present in a measured assembly, in the absence of a priori *information about the assembly; and (2) quantitative assessment of pin-by-pin properties, for example the activity of key isotopes or pin attributes such as cooling time and relative burnup, under the assumption that basic fuel parameters (e.g., assembly type and nominal fuel composition) are known. The efficacy of GET to meet these two verification objectives was evaluated across a range of fuel types, burnups and cooling times, while targeting a total interrogation time of less than 60 minutes.*

The evaluations were founded on a modelling and analysis framework applied to existing and emerging GET instrument designs. Monte Carlo models of different fuel types were used to produce simulated tomographer responses to large populations of "virtual" fuel assemblies. The simulated instrument response data were then processed using a variety of tomographic-reconstruction and image-processing methods, and scoring metrics were defined and used to evaluate the performance of the methods.

This paper describes the analysis framework and metrics used to predict tomographer performance. It also presents the design of a "universal" GET (UGET) instrument intended to support the full range of verification scenarios envisioned by the IAEA. Finally, it gives examples of the expected partial-defect detection capabilities for some fuels and diversion scenarios, and it provides a comparison of predicted performance for the notional UGET design and an optimized variant of an existing IAEA instrument.

Keywords: Spent nuclear fuel assemblies; Partial defect verification; Gamma-ray emission tomography

1. Introduction

The accurate verification of declarations about the fissile content of spent fuel is central to the International Atomic Energy Agency's (IAEA) safeguards of facilities handling and storing irradiated fuel. IAEA safeguards approaches for used fuels that are being transferred to difficult-to-access storage and that have a design allowing disassembly call for verification using a partial-defect or best-available method [1]. At present, IAEA's authorized instruments for attended partial-defect detection have limitations in terms of independence, defect sensitivity, and implementation flexibility. Furthermore, there is no authorized instrument for unattended partial-defect detection in spent fuel. Accordingly, the IAEA has expressed a need for "more sensitive and less intrusive alternatives to existing NDA instruments" for partial-defect detection [2].

Passive gamma-ray emission tomography (GET) is attractive for addressing partial-defect detection because it has the potential to non-destructively image the spatial distribution of the active fuel material in the assembly structure, and extract numerical data on individual fuel pins, without the need for any operator-declared information or disassembly of the fuel. Advantage is taken of the high level of radioactivity in used nuclear fuel in a two-step procedure:

(i) The gamma radiation field around a fuel assembly, at a selected axial level, is collected using one or several gamma-ray detector elements in a large number of positions relative to the fuel, and;

(ii) The internal source distribution in the fuel is reconstructed based on the recorded data, using tomographic algorithms.

In both steps, one may identify a multitude of alternative approaches, e.g. in terms of choice of detector set-ups and measurement schemes (step i) and choice of data analysis and reconstruction algorithms (step ii). In addition, for the case when the assay result is an image, there is a variety of image-analysis methods that may be applied to draw conclusions on the individual fuel pin level.

As described in this paper, reconstructed images and pin-wise data may be used directly to draw conclusions on possible pin diversion. Measured gamma-ray source

concentrations can also be strongly correlated to fuel parameters such as burnup (BU) and cooling time (CT), thereby achieving more specificity than other partial-defect detection methods. Further, tomographic assessment at multiple axial locations along the assembly length enables axially resolved pin-level assay (as opposed to volume-integrating assay). Finally, GET is viable in both wet and dry measurement environments, and in either unattended or attended modes, thus offering operational flexibility.

The IAEA attention to the GET technique began in the 1980's, leading to the development and testing of small-scale systems in multiple field campaigns on BWR and PWR fuel items [3]. Building on those efforts, the JNT A 1510 project began in 2003 and was completed in late 2015. Under JNT 1510, a full-scale, transportable tomography system based on IAEA's user requirements for underwater application was designed, fabricated, and field-tested [4]. This system is referred to as PGET (Passive Gamma Emission Tomography) and is used in attended mode.

In parallel to the IAEA-led efforts, a Swedish project for validating core simulators for pin-power distributions led to the construction of a heavy (30-metric tons) tomographic device, which was used for measurements on short-cooled (2-4 weeks) BWR fuel assemblies [5], [6]. As a consequence, the project also covered studies of the safeguards aspects of this technique [7]. During recent years, international nuclear research institutes have also gained interest in the application of tomographic techniques on complete fuel assemblies [8], [9]. Leveraging from the relatively large pool of knowledge and expertise that is now available on GET, the JNT 1955 Phase I project was launched by the IAEA in 2013 and was reported on in 2016 [10]. This paper accounts for its main outcomes.

2. Scope of the JNT 1955 Phase I project

The JNT 1955 Phase I project was carried out in 2013-2016 by the IAEA Member States Support Programs of the United States, Sweden, Finland and European Union, under the leadership of the IAEA. It was intended to complement previous IAEA projects on the GET technique, e.g. by considering unattended GET and an extended range of fuels and implementation scenarios.

Verification Objective	Description	Assumptions
1	Independent determination of the number of active pins that are present in a measured fuel assembly.	No a priori information about the assembly is available.
2	Quantitative assessment of pin-by-pin properties, for example the activity of key isotopes or pin attributes such as cooling time (CT) and relative burnup (BU).	Basic fuel parameters (e.g., assembly type, geometry and nominal fuel composition) are known.

Table 1: Verification Objectives covered in the JNT 1955 Phase I project.

At the project start-up, two Verification Objectives were identified, as defined in Table 1, where only Objective 1 may be considered addressed by the already existing PGET device. With these Verification Objectives in mind, efforts were made within the following areas:

- **GET performance analysis framework:** A modelling and analysis framework was developed for partial-defect detection capability evaluation, including a procedure for simulating tomographic data for selected experimental setups, fuel types, diversion and implementation scenarios;
- **GET instrument design:** The design of a "universal" GET instrument (UGETv1) was developed, intended to support the full range of verification scenarios envisioned by the IAEA;
- **Reconstruction and analysis methods:** A set of tomographic reconstruction and analysis methods were identified, described and demonstrated;
- **Proposed metrics for GET partial-defect sensitivity:** Metrics for quantifying the partial-defect detection capability of alternative GET approaches on selected diversion cases were suggested;
- **Quantitative performance predictions:** Quantitative performance predictions were made for the PGET and UGETv1 instrument designs, for a set of different fuel types, fuel parameters and diversion scenarios;
- **Inspection procedures:** An envisioned inspection procedure was presented.

Due to the extent of the work, each area is only covered superficially in the coming sections of this paper, while details may be found in [10].

3. GET performance analysis framework

One important outcome of the JNT 1955 project is the creation of a modelling and analysis framework for the evaluation of GET partial-defect-detection performance, which can be applied to various GET instrument designs, fuel assembly types and parameters, diversion scenarios and analysis methods. A flowchart describing this framework is illustrated in Figure 1. It provides end-to-end capability to assess tomographer performance for nuclear fuel assay, and could be considered a new, standing capability for the international safeguards community.

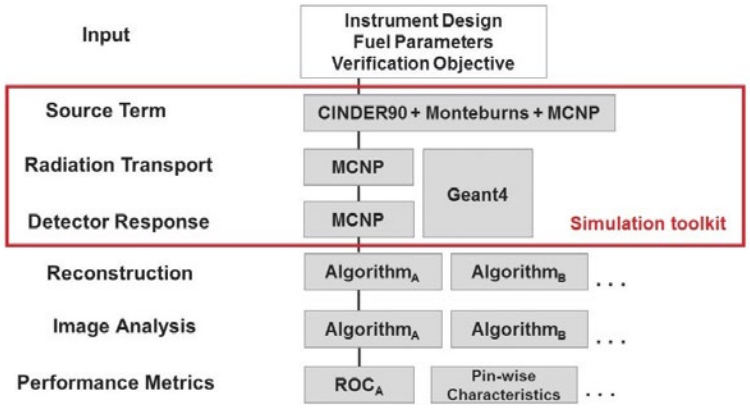

Figure 1: Flowchart describing the modelling and analysis framework developed for GET performance evaluation.

The inputs are the specifics of the fuel to be analyzed, the instrument design, including data-collection schemes such as the set of angular and lateral detector element positions used, and the conditions under which the analyses are made (e.g. the level of access to a priori information), which governs the tomographic reconstruction and analysis methods that are applicable. (Verification Objectives 1 and 2 presented in Table 1 are examples of such conditions.) The framework allows for the deployment of various reconstruction and analysis methods as well as various metrics of performance.

The heart of the framework is the simulation toolkit, marked in red in Figure 1. Here, a brief overview of the simulation procedure is presented, and the reader is referred to ref. [10] for more details;

1. First, pin-by-pin gamma-ray source terms for each fuel type and fuel parameter set under study are calculated using a combination of codes and methods, as described in refs. [11] and [12].
2. Second, the Monte Carlo N-Particle (MCNP) transport code [13] is used for transport of emitted gamma quanta from the fuel to the surface of the detector elements, taking into account the specifics of the fuel geometry studied (including possible pin diversions) and the device design. To allow for acceptable computation times for the low-efficiency transport geometries of this study, semi-deterministic transport is deployed; using MCNP's next-event estimator method, the probability of the gamma-ray contributing to a point at the front face of the detector is calculated analytically at each interaction or source point. Consequently, variations in response to gamma quanta hitting different parts of the detector surface are neglected, which is justified by the fact that the front surface of all detectors in this study was much larger than the exposed area, as defined by the collimator slit opening. These calculations are done pin-by-pin and energy-by-energy to get single-pin flux data for the complete set of detector element positions, which can be added together to form complete assembly data. In this summation, pin-wise weights are applied according to the source terms calculated in the first step. (In this way, the results from the time-consuming transport calculation can be re-used when changing pin-wise fuel parameters.) In this work, alternative simulations using the Geant4 code [14] have also been performed to benchmark the MCNP simulations, as described in section 7.2.
3. Third, separate Monte Carlo calculations of the detector response are performed, taking into account the complete gamma-ray flux into the detector elements, at all energies, while also considering detector specifics (e.g. energy resolution). Consequently, performance of different detector types in the same setup can be assessed using the same data from the first two steps.

This three-step simulation procedure allows for the creation of tomographic data for large virtual assembly populations, in terms of; (i) varying pin-by-pin BU, and; (ii) varying sets and levels of statistical noise. The former variation responds to the fact that authentic fuel assemblies have a pin-by-pin variation in BU. (In BWR fuels in particular, there may be relatively large variations in pin-wise BU due to spatial variations in void and thus in thermal neutron flux, which is met to some extent by introducing variations in initial enrichment. According to BWR operators, the maximum variation in pin-wise BU may be as large as ±20% under normal operation [15], [16].) The latter variation allows e.g. measurement time to be accounted for. Altogether, analyses of large assembly populations, with these variations included, enable the deployment of statistical performance metrics, as discussed in section 6.

4. GET instrument design

The data used for emission tomography consists of a set of gamma-ray intensities that should be recorded in well-defined angular and lateral positions with respect to the object. For the reconstructions to be efficient, a small region of the object should contribute to the recorded intensity in each position, as defined by the angle under which the radiation travels and the lateral distance of the region from the centre of rotation. In this application, heavy

collimators are used, which shield the detector elements while allowing radiation to enter through well-defined slit openings, thus allowing for the required spatial selection capability. The collimator-detector setup may be arranged in a rotate-only geometry or in a rotate-translate mechanical arrangement. The achievable spatial resolution will be governed by the system's spatial response, which is defined primarily by the slit openings, in combination with the lateral distance between each data point. (In a rotate-only geometry, the lateral distance is defined by the collimator pitch, while in a rotate-translate geometry, it is defined by the translation step used).

In the instrument design, the choice of detector as well as collimator material and dimensions depend on a number of factors such as;

– Fuel properties, e.g. BU, CT and size: Highly radioactive fuel (short CT, high BU, large mass) generally requires better shielded detector elements to avoid high levels of background radiation. Here, one may foresee a background of gamma quanta from other axial levels of the assembly than the one measured if shielding is inadequate, and gamma quanta entering the detector elements after being scattered in surrounding materials may also pose a problem;
– Requirements on isotopic selectivity: Detector elements with high energy resolution and spectroscopic data collection may be required to select specific gamma peaks, in particular for Verification Objective 2. Also, high full-energy peak efficiency will enable more efficient subtraction of background from scattered gamma rays, and thus enhanced data quality;
– Spatial resolution requirements: Longer and/or narrower collimator slits enable higher spatial resolution. (As pointed out above, spatial resolution is also governed by the measurement scheme used, in particular the lateral distance between data points.);
– Count-rate management: The collimator slit dimensions should preferably be large enough to allow for high counting rates in order to reduce measurement time, while staying within acceptable limits for the selected detector type in terms of count-rate saturation;
– Time requirements: Assay time can be shortened by using many, tightly-packed, detector elements as well as using detectors with high-count-rate capability.

Altogether, there is a strong inter-dependence between these design factors. As an example, detector elements offering high full-energy peak efficiency are generally relatively large, implying that a relatively small number of detectors will fit into the device, thus leading to longer assay times. Accordingly, instrument design will include a trade-off between e.g. time and precision.

The device design performed in this work was developed to meet both Verification Objectives 1 and 2, resulting in the notional Universal GET design (UGETv1). Thorough presentations of the UGETv1 design and the considerations made can be found in refs. [10] and [17], and only the outcome of the design work is presented here. The design was informed by two previous underwater designs, PGET [4], which was constructed in the JNT 1510 project to deliver on Verification Objective 1 for relatively long-cooled fuel, and PLUTO [6], which was constructed in Sweden to deliver pin-wise power in short-cooled fuel, a task similar to Verification Objective 2. The PGET and UGETv1 designs are illustrated in Figure 2, and their respective properties are listed in Table 2.

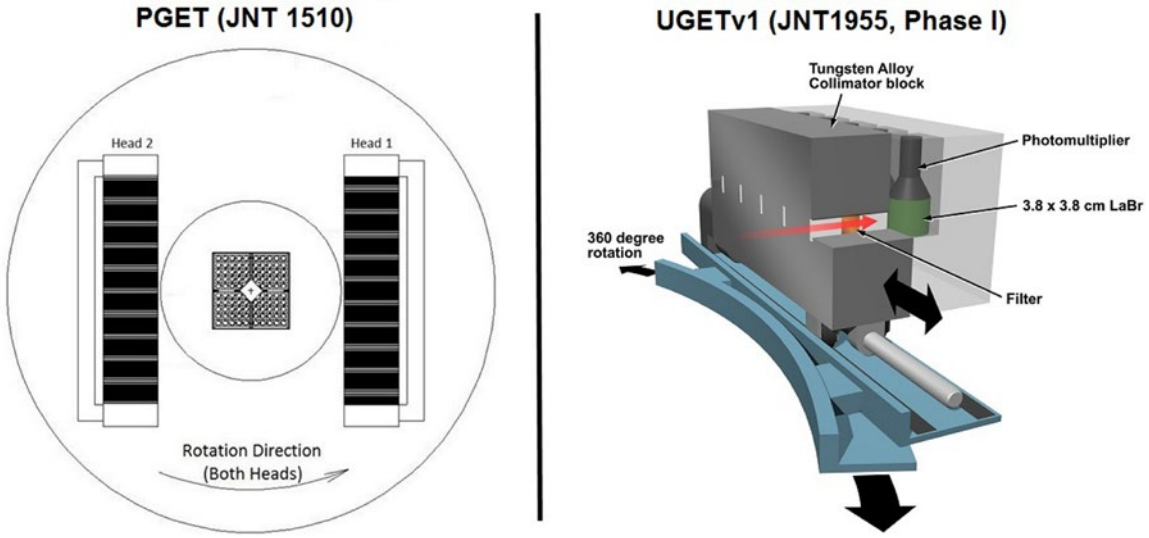

Figure 2: The two device designs analysed in section 7. **Left:** The existing PGET device, which was constructed in the JNT1510 project. It is based on two large arrays of small CdTe detectors, operated in threshold mode, in a rotate-only geometry. **Right:** A single detector head of the notional UGETv1 design, developed in this work. The full instrument would include four heads, each housing 8 relatively large $LaBr_3$ detectors operated in spectroscopic mode, in a translate-rotate geometry. The devices are not to scale.

Design parameter	PGET*	UGETv1
Maximum object diameter	30 cm	37.5 cm
Number of detector heads	2	4
Number of detectors per head	104	8
Detector type	CdTe	$LaBr_3$§
Detector dimensions	Cuboid: 10×5×2 mm^3	Cylindrical: 38x38 mm
Spectroscopic analysis	Broad Region-Of-Interest (ROI)	Peak analysis
Collimator slit length	100 mm	200 mm
Collimator slit width	1.5 mm	1.5 mm
Collimator slit height	Tapered 70→10 mm	10 mm
Detector (and slit) pitch	4 mm	46 mm
Number of lateral steps per angular projection for 2 mm sampling	- (rotation only)	23

* PGET parameters reflect design under JNT 1510. During 2016, PGET was refurbished, changing the design slightly.

§ LaBr3 scintillators are generally doped with small portions of Cerium to activate photoemission.

Table 2: Parameters of the existing JNT1510 PGET and the notional JNT1955 Phase I UGETv1 device designs.

As described in section 7, performance evaluations have been carried out for the PGET and UGETv1 designs. In short, the main differences between these designs and assumed modes of operation are; (i) the existing PGET device operates relatively small CdTe detectors in threshold mode with limited full-energy detection efficiency at high energies, while the notional UGETv1 design is intended to host larger $LaBr_3$ scintillator detectors, for which the evaluations assume spectroscopic full-energy gamma-ray peak analysis, and; (ii) PGET uses relatively light collimation, while additional shielding is included in UGETv1 to manage count rates for more short-cooled fuels (CT down to 1 year). As a result of these design selections, PGET allows for tightly-stacked detector arrays that offer rapid data collection in a rotate-only geometry, while the fewer number of $LaBr_3$ detectors in UGETv1, which offer more isotopic-specific data by means of size and mode of operation, require both rotation and translation of the detector arrays to record complete intensity projections, leading to longer assay times.

5. Reconstruction and analysis methods

Once the tomographic data have been recorded, tomographic reconstruction algorithms are applied to calculate the internal source distribution. There are a variety of algorithms available for emission tomography, which over the years have been developed and applied mainly for medical applications. However, a nuclear fuel assembly, with its highly inhomogeneous mix of strongly gamma-ray attenuating materials (such as uranium dioxide) and less attenuating materials (such as water or air), is a challenging object for tomographic measurement and reconstruction. If not taken into account in the reconstructions, gamma-ray attenuation will strongly influence the resulting representation of the source distribution. In this work, options from the two main classes of tomographic reconstruction algorithms; analytic and algebraic [18], have been explored for use on nuclear fuel assemblies. Analytic methods, such as filtered back-projection (FBP), typically use the Fourier transform, while the algebraic methods express the reconstruction in terms of an equation system, allowing for detailed modelling of e.g. attenuation when defining the equation system's weight matrix (the system matrix). The quantitative capabilities of some analysis methods when applied on emission data from nuclear fuel assemblies are presented in ref. [19].

The data used for tomographic reconstruction may constitute either of peak-specific data, giving information on the contents of the isotope emitting that particular peak, or of data that comprise a mix of information from several peaks and various levels of scattered gamma rays, depending on the instrumentation and the settings used for the data acquisition. In the end, the reconstructions will create information of the source distribution, but the specificity of this information will depend on the quality of the input data. In this section, the principles used for the tomographic reconstructions are described, while examples of output from devices with different hardware and settings are presented in section 7.

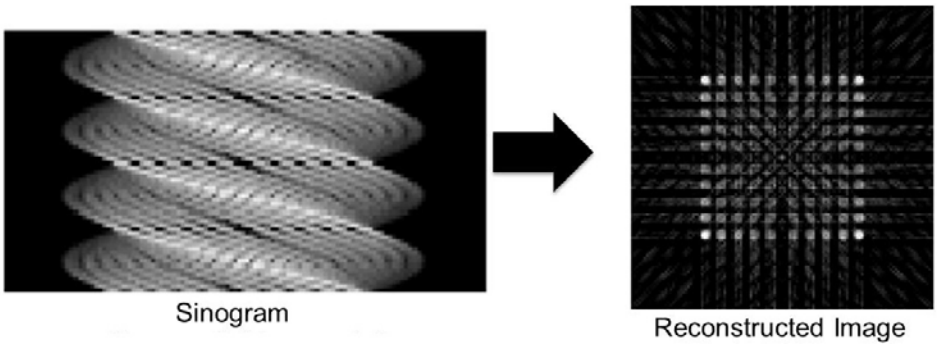

Figure 3: Tomographic data may be presented as a sinogram, with intensities as a function of lateral detector element position (horizontal axis) and angular position (vertical axis). Image reconstruction methods transform sinogram data into images of gamma-ray emission intensity, which are further analysed to deduce pin-wise data. (Example data obtained by simulating the detection of gamma rays in a 400-700 keV interval, being dominated by ^{137}Cs, modelling BWR fuel in the JNT1510 PGET instrument design.)

5.1 Image reconstruction and image analysis for Verification Objective 1

For Verification Objective 1, the number of fuel pins present should be determined without assuming any *a priori* information on the fuel. The route taken in this case is to reconstruct an image of the axial cross section of fuel, based on the collected sinogram of a fuel assembly (i.e. the collected intensities in a set of angular and lateral detector element positions relative to the fuel), see Figure 3. This image is then further analysed to deduce pin-wise data and allow for counting of the fuel pins.

Most image reconstructions in this work have been done using a standard FBP algorithm [18]. One may note that this type of algorithm does not include any attenuation corrections, and implicitly assumes an ideal spatial response function (i.e. the intensity in the detector is assumed to emanate from an infinitesimally thin line through the object). As an alternative, some reconstructions have also been performed using an algebraic method, modelling the spatial response of the collimator-detector system and assuming homogeneous attenuation in the image area when defining the system matrix [19]. With this method, a more realistic physics representation is achieved using no prior fuel information, thus fulfilling the assumptions for Objective 1. The spatial response function of the UGETv1 design used for 1274 keV gamma rays is presented in Figure 4.

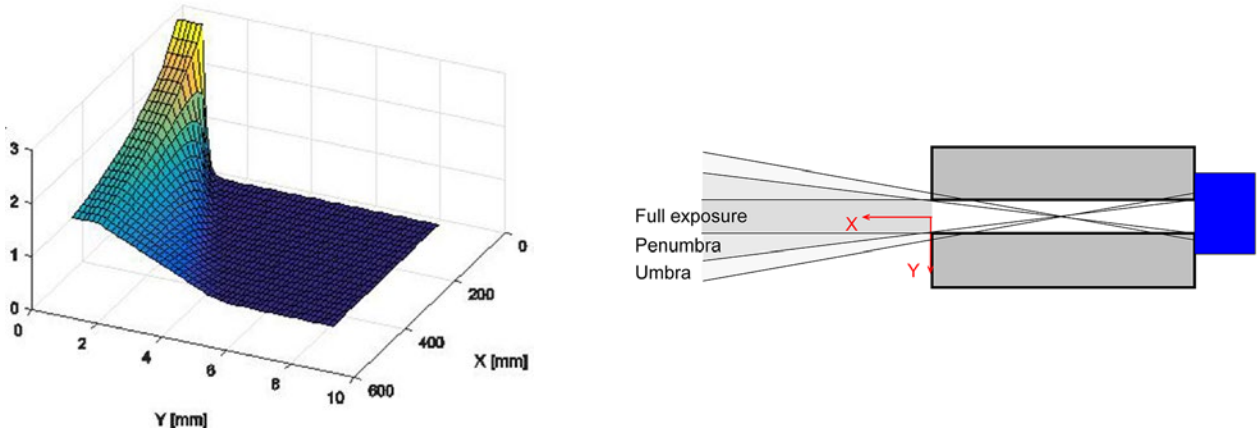

Figure 4: An example spatial response function for 1.274 MeV gamma rays (a.u. on the z axis) of the UGETv1 device design, used in algebraic reconstructions (left figure). The origin (X,Y=0) of the response function is centred at the front of the slit opening, and only positive Ys are presented. The function takes into account the physical properties of the measurement system (e.g., in terms of finite collimator slit width and gamma-ray transmission through the collimator material), which give rise to significant contributions from penumbra and umbra regions, illustrated schematically in the right figure. (For actual slit dimensions, see Table 2.)

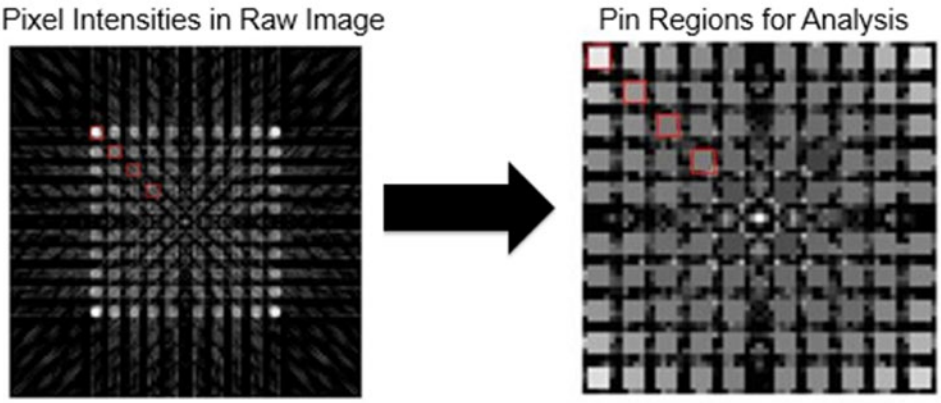

Figure 5: Example reconstructed image of simulated data for a VVER-440 assembly (left). The most fundamental image analysis is the aggregation of pixel intensity values in beforehand-defined pin-centred quadratic regions (right). A toolkit of more advanced image-analysis methods have also been developed to search the image for pins, being capable of adapting to possible irregularities in the geometry, as presented in ref. [20]. (Example images, obtained in reconstruction of simulated data from BWR fuel in the JNT1510 PGET instrument design. Here, the detection of gamma rays in a 400-700 keV ROI was modelled, being dominated by ^{137}Cs.)

Once the image is obtained, image analysis methods are required to extract pin-by-pin data, here called "pin scores". The most fundamental image analysis is to aggregate the reconstructed activities of multiple pixels in a "neighbourhood" centred on each pin location, as illustrated in Figure 5. However, irregularities that may arise from e.g. assembly torsion and pin dislocations may call for more advanced methods. A toolkit of such methods has been developed for analysis of fuel assembly images [20]. As part of the JNT1955 Phase I project, these methods were demonstrated on experimental tomographic images, proving functional on disturbed geometries [10].

Examples of analysis results for PGET and UGETv1 are given in section 7 for two combinations of methods; (i) FBP reconstruction and fundamental image analysis; and (ii) algebraic reconstruction and advanced image analysis. All analysis codes used can be made available to the IAEA.

5.2 Pin-activity reconstruction for Verification Objective 2

For Verification Objective 2, pin-wise fuel properties should be determined under the assumption that information on the fuel and its geometry is available. This opens a possibility to apply detailed modelling of the fuel configuration using algebraic methods, enabling a level of detail not accessible using analytic methods. In the work on Objective 2, three different alternatives have been used for defining a detailed system matrix in algebraic reconstructions, for which software can be made available to the IAEA; (Results obtained using t Wayfinding he two latter methods are presented in section 7.4.)

– **MCNP-generated matrix:** For simulation data obtained using MCNP (see section 3), the same transfer function as was used to create the data may be used to reconstruct the modelled source distribution. While being "unrealistically perfect" for the simulated data set, this approach enables analyses of the sensitivity to stochastic noise, added to the simulated data. For experimental data, one may also envisage the use of MCNP or similar Monte Carlo codes to model the system matrix, however, such a procedure would be excessively slow for "new" measured cases.
– **Ray-tracing:** The reconstruction toolkit TOMOPACK, with established use for reconstructions of tomographic data from the PLUTO [5] and Halden [9] devices, where %-level precision of pin-wise data has been demonstrated, is essentially based on ray-tracing and is thus suitable for analysis of spectroscopically-analysed full-energy-peak data. This modelling comprises the following features; (i) modelling of the instrument's spatial response function, see Figure 4; (ii) modelling the full-energy gamma-ray transport through the detailed 3D configuration of fuel pins, taking the axial symmetry into account, and; (iii) adaption of the pixel pattern to fit the object.
– **RADSAT-based matrix:** The Radiation Detection Scenario Analysis Toolbox (RADSAT) [21] combines 3-D deterministic transport through the measurement geometry with a stochastic model for detector response. Its use for tomography is somewhat exploratory, but it offers the capability to generate object-scatter contributions in the system matrix coefficients, for each pin, which may be essential for the analysis of data with low full-energy peak specificity, such as that of PGET.

6. Proposed metrics for GET partial-defect detection capability

For Verification Objective 1, so-called receiver operator characteristic (ROC) curves are suggested to provide metrics of the partial-defect detection capability, since they can be used to understand the trade-off between probability of detection (PD) and probability of false alarm (PFA). ROC analysis is used in many fields; a standard reference from

imaging sciences relevant to this work can be found in [22]. In the present case, the pin scores obtained from a measurement (calculated as described in Section 5.1) can be plotted as histograms, one histogram for the pins present and another for pins missing (or replaced). In the ROC analysis, a threshold value is selected, so that pin scores above the threshold are defined as pins present, while scores below the threshold are defined as non-fuel objects. If the two histograms do not overlap, perfect detection of missing pins without any false alarms can be realised. If the histograms overlap, then false alarms and/or non-detected missing pins will occur, depending on the threshold. By varying the threshold, the tradeoff between detection and false alarm can be quantified. An example of how the pin-score distributions for pins missing and pins present can be used to generate a ROC curve is given in Figure 6. When selecting an acceptable false alarm rate (setting the threshold), the ROC curve will give the corresponding probability of detection.

For Verification Objective 2, the metric used in this work (see e.g. section 7.4) is simply the agreement of reconstructed pin-wise isotopic activities with the simulated source distribution, expressed as a relative difference, or "fractional error". At the event of inspection, pin-wise data measured using a benchmarked methodology may be used to verify operator-declared data (in case such are available on the individual pin level) or to evaluate consistency among the population of pins in an assembly at a level within the demonstrated precision.

7. Quantitative performance predictions of PGET and UGETv1 device designs

Using the modelling and simulation framework described in section 3, the expected performance of two device designs has been analysed; the existing PGET device and the notional UGETv1 device (see section 4). The reconstruction tools described in section 5 have been deployed, as well as the performance metrics described in section 6.

7.1 Analysed cases

Since the number of imaginable GET implementation alternatives and diversion scenarios are exceedingly large, and a vast amount of time is required for simulating each foreseeable case, a comprehensive study of all possibilities would not be manageable. Consequently, this study was limited to a relatively small set of implementation and pin-diversion scenarios, fuel types and parameters, and gamma-ray energies used for assay, according to the following;

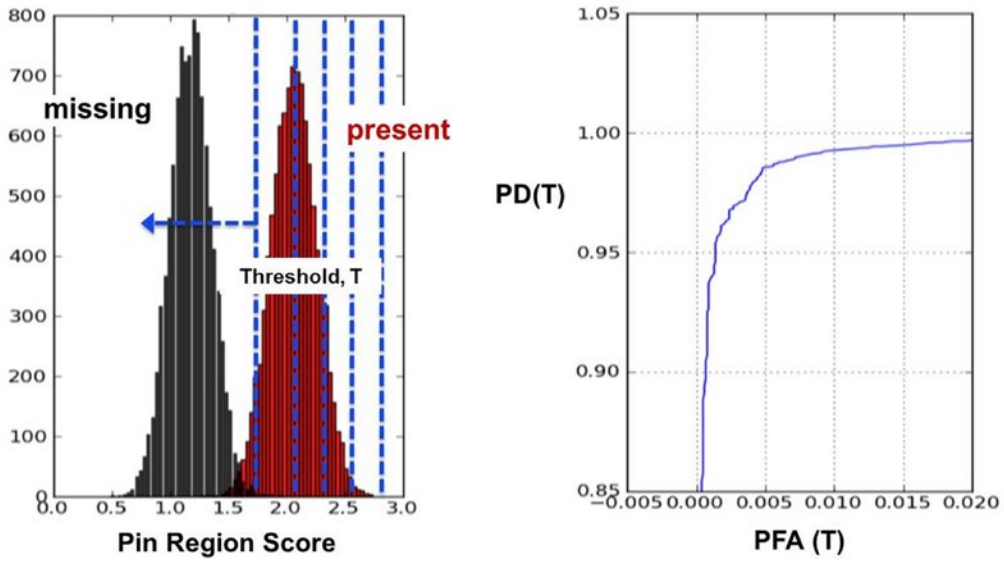

Figure 6: Pin-score distributions for pins missing and pins present (left) can be used to calculate the probably of detection (PD) and probability of false alarm (PFA) as a function of threshold, T, in terms of a ROC curve (right).

Implementation scenarios: The matrix of implementation scenarios (including fuel CTs), deployment constraints and target measurement times considered in this work is presented in Table 3. The notional UGETv1 device covers a CT range from 1 to 40 years, while PGET is not applicable for CTs as short as 1 year. Measurement times up to approximately 60 minutes were assumed acceptable. Only underwater assay was studied.

Pin-diversion scenarios: Three partial defect scenarios were considered; (i) Pin removal without any substituting materials, i.e. with water replacing the pins; (ii) Pin replacement with depleted-uranium pins (replicates low- or no-activity containing high-density substitute), and; (iii) Pin replacement with fuel pins of the same construction but lower BU (replicates material diversion between reactor cycles). However, as described in [10], scenario (ii) poses the least tomographically challenging case. Focusing on the

more challenging cases, only results from scenarios (i) and (iii) are presented here.

Fuel types, parameters and pin configurations: Three fuel types were studied, for which the simulated fuel pin configurations are illustrated in Figure 7; (i) SVEA-96S BWR fuel with 96 fuel pins, of which 5 were diverted; (ii) VVER-440 fuel with 1 water channel and 126 fuel pins, of which 6 were diverted, and; (iii) PWR 17x17 fuel with 25 water channels and 264 fuel pins, of which 11 were diverted. Due to gamma-ray attenuation, it is more challenging to tomographically measure fuel types with large and dense pin configurations, where information obtained from central fuel pins is scarce. Accordingly, BWR fuel poses the least challenging configuration and PWR poses the most challenging. Fuel BUs from 10 to 40 GWd/MTU were analysed in order to span typical values encountered in commercial power industry.

Gamma-ray energies: The gamma-ray source terms will depend on the fuel parameters; short-cooled assemblies will contain short-lived as well as long-lived fission products and higher total activity, while the gamma-ray spectrum emitted from long-cooled assemblies (CT>30 years) will be dominated by ^{137}Cs. All simulations covered a large number of gamma emitters and energies, but in the tomographic analyses only a few energy regions were selected (taking detector characteristics into consideration), corresponding to specific gamma-emitting fission products. The gamma-ray energies under study in this work are presented in Table 4. For each gamma-ray energy, relevant stochastic noise levels corresponding to assay time, BU and CT, were included in the statistical analyses of each simulated fuel type. The noise levels were given by Poisson statistics, based on simulated absolute intensities.

Implementation Scenario	Cooling time (years)	Deployment constraints
Routine verification of old fuel being transferred to a geologic repository	40	Attended or unattended
Routine verification of fuel being transferred to dry storage	5	Attended or unattended
Random verification of in-pool inventory	1	Attended

Table 3: Description of GET implementation scenarios considered in this work. The hardware configurations studied were the existing PGET device and the notional UGETv1 design (see section 4), for both Verification Objective 1 and Objective 2.

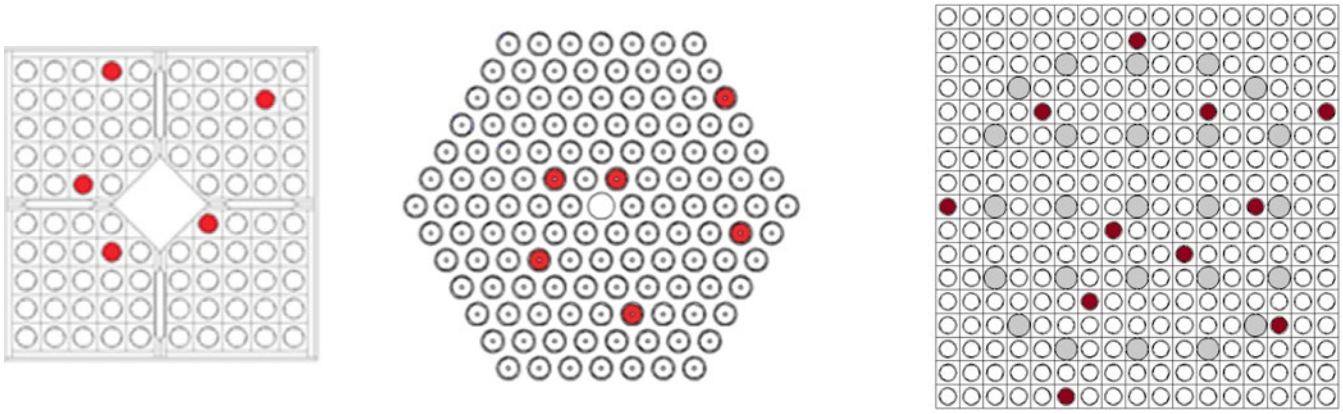

Figure 7: Map of the simulated diverted pin locations (in red) in the three assembly types under study: five for BWR (left), six for VVER-440 (middle) and 11 for PWR (right). In addition, VVER fuel by design includes one central water channel and PWR fuel includes 25 water channels (marked in grey). The fuel geometries are presented approximately, but not exactly, to scale.

Isotope	Energy [MeV]	Branching ratio [%]	Half-life	Relevant CT range
^{137}Cs	0.662	85.1	30.1 y	up to 100-150 y
^{134}Cs	0.605	97.6	2.1 y	up to 10 y
	0.796	85.5		
^{154}Eu	0.723	20.1	8.6 y	up to 25–30 y
	0.873	12.1		
	0.996	10.5		
	1.005	18.0		
	1.274	34.8		
^{144}Pr (^{144}Ce)	2.186	0.7	285 d	up to 5 y

Table 4: Characteristic fission products and associated gamma-ray emissions from spent fuel in the 0.4-2.5 MeV energy region. (Data from [23])

In general, the higher gamma-ray energies in Table 4 facilitate tomographic assay, since their higher penetrability enables more information to be obtained from the assemblies' innermost sections. However, also the emission intensity is important. For ^{154}Eu, the highest energy (1.274 MeV) is also the most intense and thus the most useful. One should note that for relatively long-cooled fuel (CT between 30 and about 100 years), only the long-lived, lower-energy gamma emitter ^{137}Cs is abundant enough to be measured.

7.2 Simulation and benchmarking

The simulation toolkit described in section 3 was used to create tomographic data for sets of virtual fuel assemblies for the cases accounted for above. For all simulations, all gamma quanta interacting in the detector elements were analysed with respect to their energy deposition, and the number of events in selected energy ROIs were analysed. The settings used for simulating the PGET device are presented in Table 5. For the notional UGETv1 device, spectroscopic full-energy peak analysis including subtraction of background under the peaks was assumed, and the detection of a set of individual emission lines in a small energy interval (few keV) about each peak was simulated.

ROI [keV]	Comment
400-700	Used for analysis of 662 keV gamma from ^{137}Cs
700-1100	Used for analysis of ^{154}Eu (primarily lines at 723, 873, 996, and 1005 keV)
1100+	Used for analysis of 1274 keV gamma from ^{154}Eu

Table 5: The Regions-Of-Interest (ROI) used when simulating PGET data. In the simulations, the energy deposition in the detector elements were analysed, while counting the number of events falling within the ROIs.

Following the procedure described in section 3, "single-pin base sinograms" were weighted and added together to comply with isotopic contents due to selected pin-wise BU and CT. Accordingly, high statistical quality of these "base data" was critically important for reducing systematic effects in the large sets of derived virtual assemblies that were used to assess performance evaluation. A particular concern was the sampling of pin contributions from the inner regions of the assembly, where gamma-ray self-shielding and line-of-sight obstructions are severe, leading to few sinogram counts. However, the calculation scheme did not allow for statistical analyses of individual single-pin sinograms. Instead, an estimate of precision emanating from the "base data" was achieved using two separate, independent simulations, according to a procedure described in [10]; In short, a "difficult case" (low gamma-ray energy from ^{137}Cs in a large PWR fuel configuration) was selected, for which tomographic data was obtained by aggregating "base data" respectively by performing an independent, high-level-statistics simulation of a complete fuel assembly with corresponding pin-wise ^{137}Cs contents. The two sets of data were used in identical reconstructions, and the differences in reconstructed pin-wise data were interpreted as imprecision emanating from the "base data". It was found that fuel pins near the assembly periphery were reconstructed at almost identical values for the two data sets, whereas differences increased towards the assembly centre, as expected. For all fuel pins the differences were within maximum ±3%, giving an indication of the precision of the base data and thus defining a limit of the achievable agreement of reconstructed pin-wise data to simulated source contents for this "difficult case". One may note that implications of counting statistics, due to e.g. variations in detector count rate or measurement time, may be evaluated at a higher level of precision by investigating the statistical spread obtained when adding such variations to the base data.

In order to ensure that the simulation-based conclusions drawn on PGET and UGETv1 performance for various fuel parameters and measurement times are correct, the Monte Carlo simulations were verified and validated in multiple ways;

- Gamma-ray source terms and detector response calculations (simulation steps 1 and 3 of Section 3) were evaluated using experimental data from measurements performed at the Clab interim storage facility for spent fuel in Sweden. This benchmark included relative peak intensities for a large number of gamma peaks as well as peak shape and level of Compton-scattered background;
- The Monte Carlo-based gamma-ray transport (simulation step 2 of Section 3) was evaluated using experimental tomographic data from the PLUTO device [5]. Both simulated gamma-ray projections as well as properties of reconstructed images were evaluated;
- The MCNP model of the PGET device was evaluated using experimental PGET data;
- A model of the PGET device was also developed in the alternative Monte Carlo simulation tool Geant4, and the Geant4 simulations were evaluated using experimental PGET data, and;
- The MCNP model of the notional UGETv1 device was evaluated in inter-code simulation comparisons to an independent Geant4 model.

All evaluations were considered satisfactory, thus providing confidence in the comparisons made between expected instrument performance for the existing PGET and the notional UGETv1 devices. Details on the evaluations can be found in ref. [10].

7.3 Results for Verification Objective 1: Independent pin counting

As accounted for in section 5.1, the approach for Verification Objective 1 was to use tomographic data in different types of image reconstructions, and perform image

analysis on the reconstructed images to independently count the number of fuel pins. Two alternative analysis routes were taken:

– **Analysis Route 1:** Basic analytic FBP image reconstruction, followed by basic image analysis (summing sets of pixel values said beforehand to represent each fuel pin). While not allowing for inclusion of spatial response or gamma-ray attenuation in the reconstruction, nor adaption to possible dislocation or torsion of the fuel in the image analysis, this route enabled automated analysis of large populations (up to 1,000) of simulated assemblies with varying BU distributions and stochastic noise. Consequently, this route enabled ROC curve analyses, as described below.
– **Analysis Route 2:** Algebraic image reconstruction and analysis, including modelling of the device's spatial response function and homogeneous gamma-ray attenuation in the image reconstruction as well as more advanced image analysis tools to identify and quantify pin-shaped objects in the reconstructed image. This route was not automated and thus smaller populations of assemblies could be analysed (up to 10), excluding ROC curve analyses of the results.

Apart from demonstrating the methods' capabilities to distinguish diverted fuel pins from pins present, one important aspect of these studies was to compare the performance of the PGET and UGETv1 devices.

Examples of quantified pin-wise ^{154}Eu activities when applying the two alternative analyses routes on simulated UGETv1 data for short-cooled PWR fuel assemblies with missing pins, offering a challenging diversion scenario for the most challenging fuel type of the three under study, are presented in Figure 8. As seen in the figure, the FBP reconstruction (which does not take gamma-ray attenuation into account) calculates lower pin activities in the assembly interior than in its periphery, whereas a more leveled response is given by the model-based algebraic reconstruction (which takes gamma-ray attenuation into account). In agreement with ref. [19], model-based reconstruction seems to allow for better separation between fuel pins and missing pins and/or water channels. However, one should also note that the simulation for the latter does not include any pin-BU variation.

ROC curve formalism (see section 6) was used to compare the expected performance of the existing PGET device with that of the notional UGETv1 device. For both devices, perfect energy and efficiency calibration of detector elements was assumed in the simulations. The evaluations were based on automated FBP reconstruction and summation of pixel values (Analysis Route 1) for sets of 1,000 virtual fuel assemblies with a BU variation for each pin selected from a uniform distribution within ±20% of the nominal value and stochastic noise corresponding to a 60-minute assay for UGETv1 and a 10-min assay for PGET. The results for the three fuel types under study with fuel parameter sets {BU=20 GWd/MTU, CT=5 years} and {BU=10 GWd/MTU, CT=40 years} are presented in Figure 9. For the sets with CT=5 years, the 1274-keV radiation from ^{154}Eu was analysed, while the 662-keV radiation from ^{137}Cs was used for the sets with CT=40 years.

The ROC curves in Figure 9 indicate that PGET offers more confident or similar capability of detecting missing pins as UGETv1. However, one should also note that no ROC analyses have been made for Analysis Route 2, which might offer different detection capability according to the results in Figure 8. The detection capability is further discussed in section 7.5.

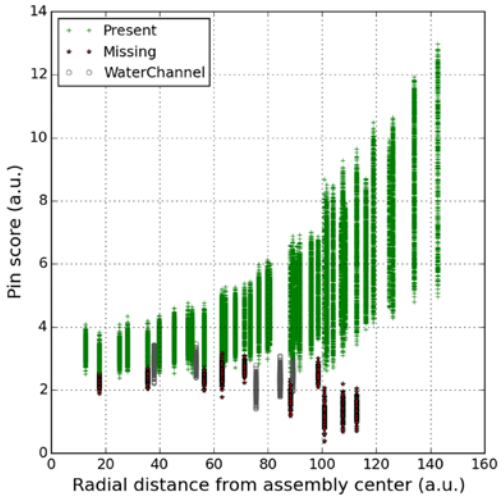

Radial distance from assembly centre (a.u.)

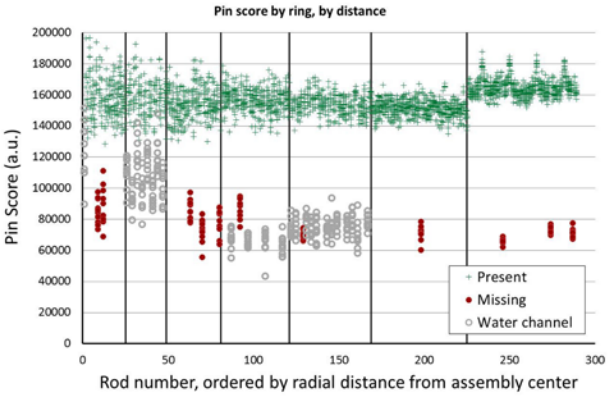

Pin number, ordered by ring, by radial distance from assembly centre (a.u.)

Figure 8: Pin-scores for pins present and pins missing, simulating the deployment of the UGETv1 device on sets of PWR assemblies (BU=40 GWd/MTU, CT=1 year) using the 1275 keV emission from ^{154}Eu. The upper figure results from simple FBP reconstruction and pixel summation on a set of 100 virtual assemblies with ±20% pin-wise BU variation. The lower figure results from model-based algebraic reconstruction and image analysis on a set of 10 virtual assemblies with no pin-wise BU variation. (Since the lower figure is the aggregate of 10 simulations, each of fuel with 253 pins present, 11 pins missing and 25 water channels, it contains markers for in total 2783 pins present, 110 pins missing and 275 water channels.) Both data sets include stochastic noise.

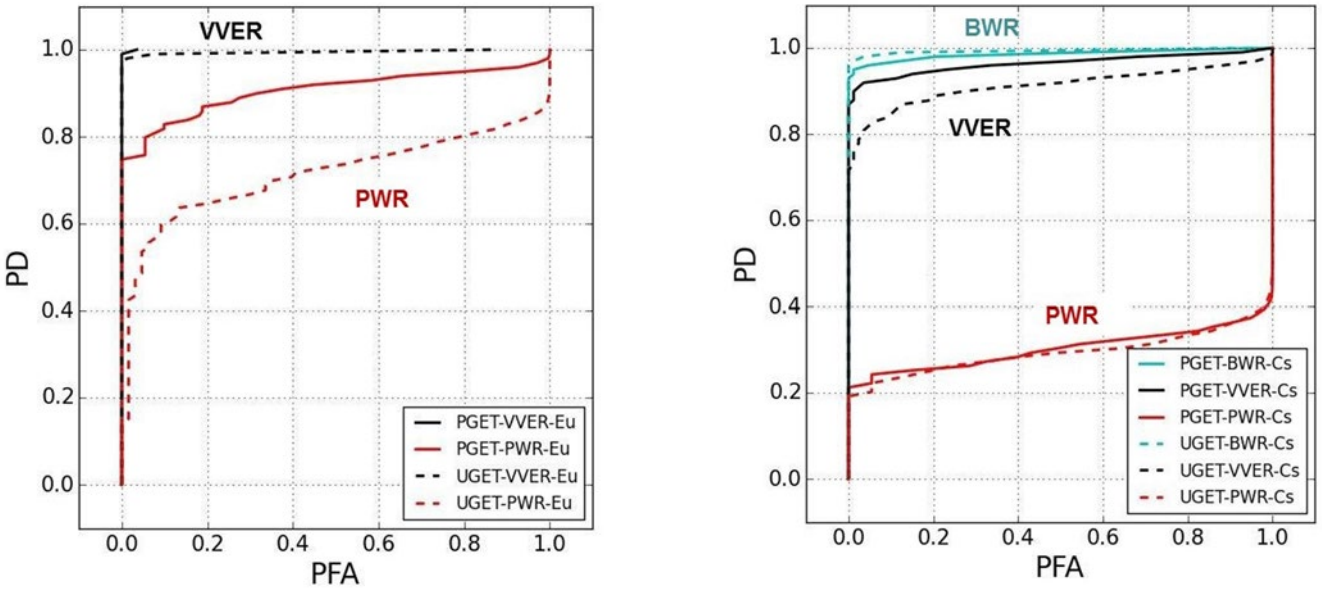

Figure 9: Predicted detection sensitivity of a single missing pin (i.e., bias defect) for perfectly-calibrated PGET and UGETv1 for BWR, VVER and PWR fuels, deploying simple FBP reconstruction and pixel summation. **Left:** Nominal BU of 20 GWd/MTU and 5 year CT with assay based on ^{154}Eu. (BWR performance is even higher than VVER and therefore not shown.) **Right:** Nominal BU of 10 GWd/MTU and 40-year CT with assay based on ^{137}Cs.

7.4 Results for Verification Objective 2: Pin-wise fuel properties

Verification Objective 2 assumes availability of the fuel-geometry information needed to enable the detailed algebraic reconstruction methods described in section 5.2. Using these methods, pin-wise isotopic contents are reconstructed (rather than images as in Verification Objective 1). The quality of the results, i.e. the precision of the calculated pin-wise isotopic contents, will depend on the fidelity of the algebraic system matrix. If spectroscopic full-energy peak analysis is applied, such as in the notional UGETv1 design (see section 2.2), full fidelity may be provided by full-energy transport calculations (ray tracing). If the collected data comprises significant object-scattered components, which may be the case for the PGET design, the calculations may require the inclusion of gamma-ray scattering as well. However, the more detail that is included in the calculations, the longer the execution time, which may make the most detailed calculations, such as MCNP, prohibitively long.

The results from three types of analyses are presented below;

1. Pin-wise isotopic-content reconstructions using the ray-tracing toolkit TOMOPACK, applied to simulated data for the notional UGETv1 device design for PWR fuel assemblies;
2. Pin-wise isotopic-content reconstructions using the RADSAT toolbox, which includes calculations of gamma-ray scattering components, applied on simulated data for the notional UGETv1 device design and the existing PGET device.
3. Estimation of pin-wise BU and CT, based on measured pin-wise isotopic contents.

For a complete description of all analyses performed, we refer to [10].

7.4.1 Ray-tracing-based reconstruction models

Simulations of UGETv1 assay of PWR fuel assemblies with 11 fuel pins missing (see Figure 7) have been analysed using the TOMOPACK ray-tracing-based reconstruction toolkit. In the simulations, the assemblies contained uniform pin-wise isotopic contents, and sets of 10 virtual assemblies were analysed for each case under study. Results for a short-cooled (1 year), high-BU PWR assembly (40 GWd/MTU) with 11 fuel pins missing are presented in Figure 10. Reconstructed relative pin-by-pin isotopic contents of ^{137}Cs, ^{134}Cs and ^{154}Eu are presented in terms of the fractional error from the simulated values, ordered ring-by-ring from the fuel assembly centre to the periphery. In the presented cases, the level of statistics in the analysed data sets corresponds to 40 minutes total assay time. Since a prerequisite for Verification Objective 2 was a priori known fuel geometry, activities are only reconstructed in fuel pins present and not in water channels or positions of missing pins.

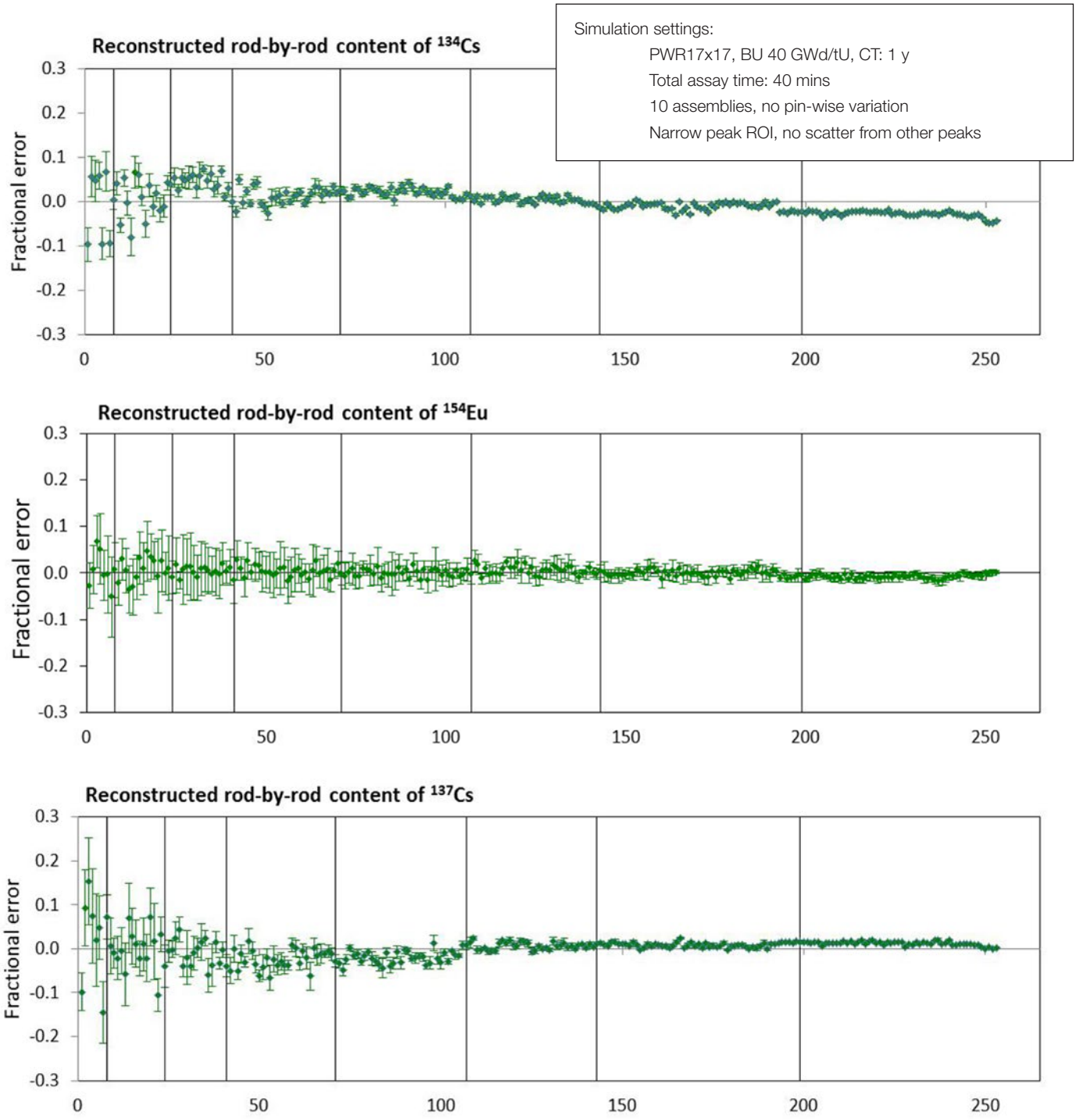

Figure 10: Results obtained in TOMOPACK reconstructions of simulated data for short-cooled, high-BU PWR 17x17 fuel assemblies in the suggested UGETv1 device design, presented as mean values of fractional error in reconstructed pin-by-pin isotopic contents obtained in analyses of 10 datasets, including error bars corresponding to ±1 σ confidence intervals. All pins were assigned equal isotopic contents in the simulations. The analyses were based on full-energy gamma peaks at 662 keV (^{137}Cs), 796 keV (^{134}Cs) and 1274 keV (^{154}Eu).

For all three isotopes in Figure 10, precision is high in peripheral fuel pins and up to about 10% (1 σ) in central fuel pins. Systematic deviations are generally smaller than a few %, except for the most central sections, where insufficient sampling of single-pin base sinograms may disturb the analysis (see section 3). The best and most stable results are obtained for ^{154}Eu, which emits the highest gamma-ray energy (1274 keV) and thus offers the highest escape fraction from the assembly centre.

The TOMOPACK ray-tracing toolkit was also used for reconstructing the pin-wise content of ^{137}Cs based on simulations of long-cooled (40 years) low-BU (10 GWd/MTU) PWR fuel. In this "difficult" case (low source concentration, low gamma-ray energy, large-sized fuel), longer measurement times would be required to obtain good statistics, and approximately 2 hours total assay time would give similar results as presented in Figure 10 (top).

7.4.2 Reconstruction models including scattered components

The RADSAT-based reconstruction approach offers a possible means to introduce scattering components when defining the system matrix, which may be valuable for the analyses of PGET data, in particular when broad energy windows are deployed so that object scatter constitutes a significant portion of the sinogram signal. Here, RADSAT has been used to analyse simulated data for both the UGETv1 and the PGET device. Data sets from 100 virtual VVER assemblies were studied, including ±20% variation in pin BU and six tampered fuel pins with 50% of the average BU value (replicating material diversion at about mid-life of the fuel). Figures 11 and 12 show the results for pin-by-pin quantification of the ^{137}Cs and ^{154}Eu concentrations in VVER fuel with two sets of fuel parameters; {BU=20 GWd/MTU, CT=5 years} and {BU=10 GWd/MTU, CT=40 years}. As described in section 7.2, relatively broad ROI were used when simulating PGET data, while UGETv1 data were simulated assuming spectroscopic full-energy peak analysis with background subtraction.

As seen in Figure 11 (top) and Figure 12 (top), RADSAT calculates activities in normal fuel pins within a few percent for all VVER fuels under study, when applied on simulated data for the UGETv1 device. Statistical uncertainty is smaller in the assembly periphery (as expected), but also in the inner sections precision is in the order of a few percent. Some systematic deviations may be identified, but these are also on the few-percent level. Performance is good also for tampered fuel pins, although their content of ^{154}Eu is generally slightly overpredicted and the statistical uncertainty is higher than for normal fuel pins. Accordingly, one would expect these tampered fuel pins to be confidently detected. In addition, a short-CT (1 year), high-BU (40 GWd/MTU) fuel was studied, giving similar results for ^{154}Eu assay using UGETv1 as presented in Figure 11 (top). (For this short-cooled fuel, only UGETv1 assessment was covered because PGET cannot manage the high count rates encountered for such fuel.)

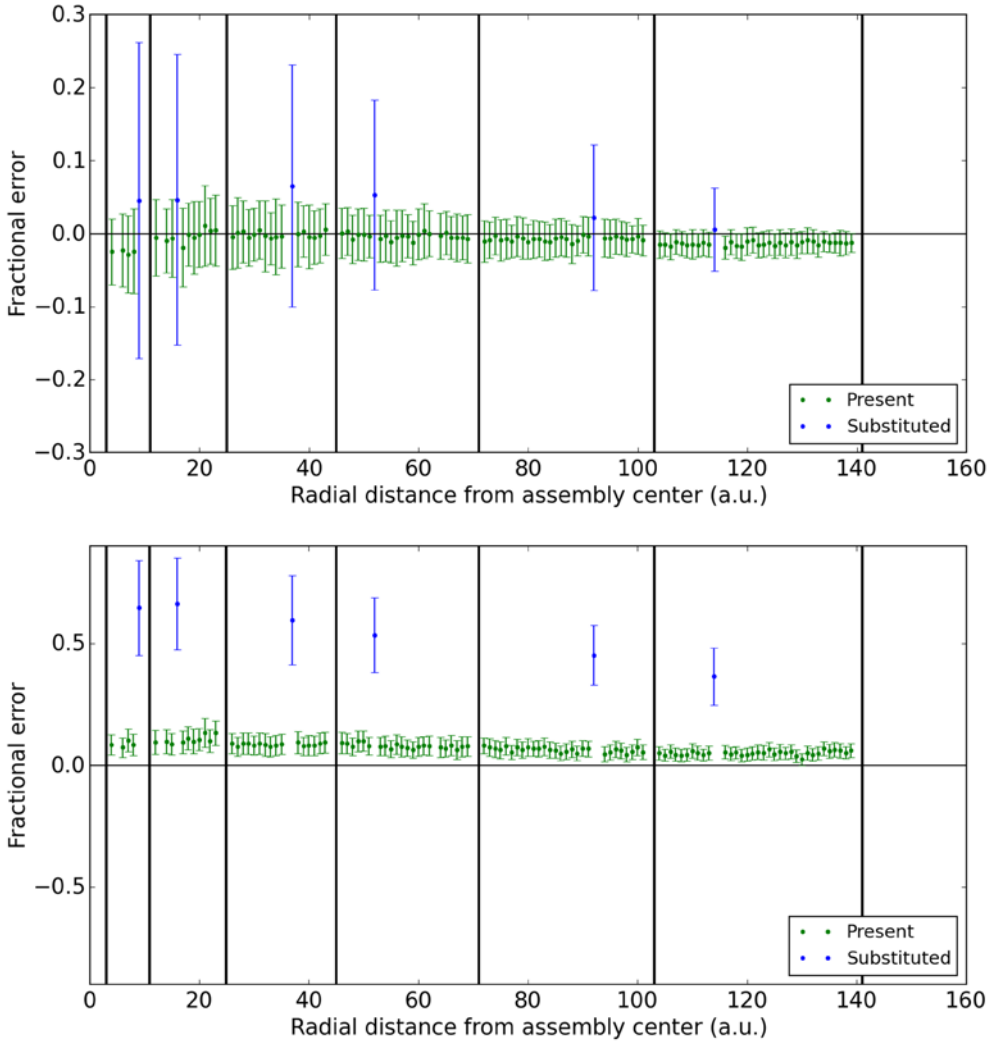

Figure 11: Fractional error, relative to true values, for pin-by-pin ^{154}Eu activity reconstruction with RADSAT-based system matrix using UGETv1 (top panel) and PGET (bottom panel). The 100-assembly population assumed VVER fuel with nominal BU of 20 GWd/MTU, 5-year CT, and ±20% pin-wise BU variation. Tampered pins (blue), have a nominal activity half that of the pins present (green). Error bars represent 1 σ uncertainties, obtained based on the simulated fuel population.

In the analyses of simulated data for the PGET device, there is a systematic overprediction of the activities in normal fuel pins, which increases towards the assembly centre. The tampered fuel pins are strongly overpredicted, especially for the ^{154}Eu assessment in Figure 11 (bottom), which would complicate their detection. Alternative ways to improve this situation could be to (i) analysis-wise further enhance the modelling capabilities for scattering, or (ii) measurement-wise define energy windows such that scattering components in the data are minimized. While the latter alternative may be applicable to ^{137}Cs data, the low full-energy detection efficiency at 1274 keV of the PGET detector elements may preclude such an approach for ^{154}Eu data.

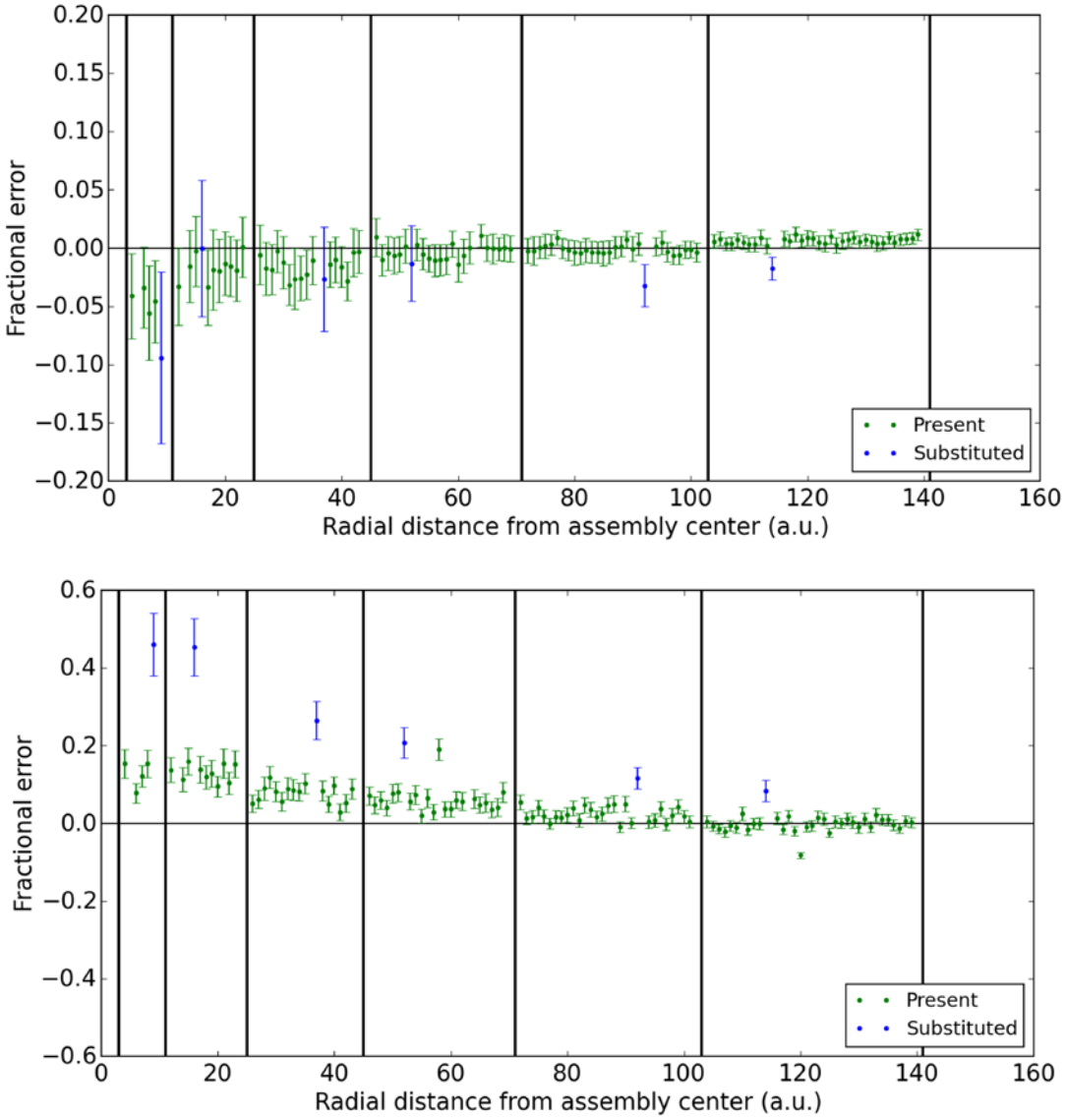

Figure 12: Fractional error, relative to true values, for pin-by-pin ^{137}Cs activity reconstruction with RADSAT-based system matrix using UGETv1 (top panel) and PGET (bottom panel). The 100-assembly population assumed VVER fuel with nominal BU of 10 GWd/MTU, 40-year CT and ±20% pin-wise BU variation. Tampered pins (blue), have a nominal activity half that of the pins present (green). Error bars represent 1 σ uncertainties, obtained based on the simulated fuel population.

7.4.3. Pin-wise BU and CT determination

Gamma-ray spectroscopy is an established technique to characterize nuclear fuel, and several studies have been made to establish correlations between full-energy peak intensities of gamma rays from ^{137}Cs, ^{134}Cs and ^{154}Eu, recorded in gamma-scanning measurements of nuclear fuel assemblies, to fuel parameters such as BU and CT [24]. In a similar manner, tomographically measured pin-wise activities of these isotopes may be used to determine BU and CT on the single-pin level. These pin-wise fuel parameters may, in turn, be used to control the consistency of the population of fuel pins in an assembly or even to verify operator-declared data, if available on the single-pin level. However, such data are not typically provided to the IAEA today in spent fuel declarations.

As described in [10], the investigations performed in this work lead to the following conclusions;

– For short-cooled fuels, analysis of the quotients of the tomographically measured pin-wise contents of ^{134}Cs and ^{154}Eu would offer the smallest statistical uncertainty in the determination of pin-wise BU and CT, using the methods in [24], when these isotopes are available (i.e. at CT<10 years).
– At intermediate CT (10 to 30 years), the quotient of ^{154}Eu and ^{137}Cs can be used, with slightly larger statistical uncertainties.
– At long CT (>30 years), only ^{137}Cs will be available. However, ^{137}Cs can still give a direct measure of the fuel BU, provided that all fuel pins have the same CT. Consequently, the precisions demonstrated in e.g. Figure 10 (top) or Figure 12 (top) give a direct measure of the achievable precisions in pin-wise BU determination.

Considering a 40-minute assay using the notional UGETv1 device, the simulations and ray-tracing-based analyses in this work (see section 7.4.1) show that even for the innermost sections of PWR fuel assemblies with CT=1 year and BU=40 GWd/MTU, the pin-wise BU and CT may be determined with statistical uncertainties below 6% and 0.4 years, respectively, based on the quotients of the pins' ^{134}Cs and ^{154}Eu contents. However, one should note that this represents the highest achievable precision, which requires that systematic uncertainties are eliminated. For more information, we refer to [10].

7.5 Discussion on predicted UGETv1 and PGET performance

As seen in Figure 9, the evaluations on Verification Objective 1 indicate that PGET performance would exceed that of UGETv1 for most analysed cases. The reason is mainly the larger number of detector elements in PGET, which leads to more efficient data collection and thus to better counting statistics during a fixed measurement time. Assuming an operationally tolerable false alarm rate of approximately 0.05 (1 false alarm per 20 assemblies), these findings indicate that Analysis Route 1 (FBP reconstruction and summation of pixel values) would achieve a probability of detecting a single missing pin, at any location in the assembly, that is greater than 0.80 for VVER and BWR fuels, with both devices, regardless of BU and CT. However, the evaluation also indicates that the single-missing-pin performance for both devices would be low for PWR fuel (due to its large physical dimension and relatively tight fuel-pin spacing). Referring to Figure 8, one should note that alternative analyses, such as Analysis Route 2 (algebraic reconstruction and advanced image analysis) may perform better, albeit efforts must be made to automate it for use in unattended mode.

As seen in Figure 11 and 12, the evaluations on Verification Objective 2 indicate superior performance of the UGETv1 device as compared to PGET, contrary to Objective 1. The reason is the capability of UGETv1 to select full-energy gamma, which enables the analysis of isotope-specific data. However, one may expect that smaller energy windows (for example 630-680 keV instead of 400-700 keV for ^{137}Cs, which was simulated here), may help to reduce the systematic bias in the application of PGET to Objective 2. More investigations of object-scatter effects, as a function of energy-window width in PGET, are needed. For UGETv1, a potential to deduce pin-wise BU and CT in short-cooled PWR fuel with statistical uncertainties below 6% for BU and below 0.4 years for CT, has been indicated even for central pins.

Finally, one should note that PGET is not operational at CTs down to 1 year due to count-rate saturation of the detector elements in the high gamma flux from short-cooled fuel, while UGETv1 was designed to be operational also at short CTs. For Verification Objective 1, results obtained when applying Analysis Route 1 on UGETv1 data at CT=1 year shows that a probability >95% for detecting a single missing fuel pin would be achievable for all three fuel types under study, assuming a tolerable false alarm rate of 0.10. For more detailed information of these analyses, we refer to [10].

8. Envisaged inspection procedure

The envisioned inspection procedure, identified and refined as part of the JNT 1955 Phase I project can be outlined according to the following:

A. Baseline inspection procedure, performed on-site, either automatically in case of unattended use or by an inspector in the case of attended use:

1. Tomographic measurement
2. Online image reconstruction
3. Online image analysis
4. On-site initial integrity statement

B. If undeclared removal/replacement is suspected:

5. Detailed pin-activity reconstruction based on current fuel type and position in device. (No additional measurement required.)

The last step (B.5) reflects the functionality of Verification Objective 2, at least if operator-declared information is used for the detailed modelling. However, it may also be envisaged that geometric information is extracted directly from reconstructed images in step A.2, without any need for operator-declared data. Such a possible procedure ("Verification Objective 1.5") is also discussed below.

9. Conclusions, discussion and outlook

According to this and previous studies, GET has the potential to provide bias-defect sensitivity in most fuel verification scenarios, a significant improvement over IAEA's current partial-defect capabilities using a Fork-based system or Digital Cerenkov Viewing Device. The IAEA also possesses a GET measuring device for attended use (PGET). This device was refurbished during 2016, introducing e.g. new detector elements and data-acquisition electronics in order to provide adequate efficiency and energy calibration; capabilities which did not meet expectations before refurbishment. The current study covers analyses of expected PGET performance, based on simulations for a variety of fuel types and fuel parameter sets, assuming high-fidelity calibration but based on the detailed design before refurbishment. Because only minor changes were made to the detector elements, the results are expected to be representative for the refurbished PGET. However, there may still be room for improvements in terms of e.g. optimisation of energy windows used for selecting the detected gamma rays to be analysed, which can be a subject for future studies.

In this study, a "Universal" GET design has been developed ("UGETv1"), which is capable of supporting the full range of fuel characteristics considered in this study, but that versatility comes at a price in terms of both assay time and instrument lifecycle cost. (For cost estimates, see [10].)

A set of tomographic reconstruction algorithms has been identified, described and used, which may find use in the application of GET for safeguards. For Verification Objective 1 (counting of fuel pins without any prior information on the fuel), image reconstruction algorithms have been presented, which are complemented by image-analysis methods to count the number of fuel pins present in the measured assembly. For Verification Objective 2 (determination of pin-wise fuel properties, making use of prior information on e.g. fuel geometry), algebraic methods have been suggested that include detailed modelling of the gamma-ray transport through the fuel configuration.

Among the outcomes of this work is the creation of a simulation and modelling framework, which provides end-to-end capability to assess tomographer performance for nuclear fuel assay, and could be considered a new, standing capability for the international safeguards community, available on request. It is modularised to allow for studies of expected performance of various GET measurement device designs for a variety of fuel types, fuel properties and data analysis methods.

For Verification Objective 1, it was found that the PGET and UGETv1 devices exhibit, in general, comparable performance despite their very different designs, but PGET achieves that sensitivity in shorter assay times. The higher collection efficiency of PGET elevates its performance over UGET for cases where the signal coming from interior pins is particularly weak (e.g., PWR assemblies), while UGET achieves high performance for the shortest-cooled fuels that cannot be measured by PGET. These comparative findings are based on an analytic FBP reconstruction; however, results may vary with other reconstruction methods. One may e.g. note that algebraic reconstruction including modelling of the system's intrinsic response function and uniform attenuation gave the most promising results in terms of separation between fuel pins and background, see e.g. Figure 8. Prior work has also indicated that image analysis and algebraic reconstruction methods offer the potential robustness to issues such as misalignment of assemblies, bowing of individual fuel pins, non-functioning detector elements, irregular measurement positions etc.

For Verification Objective 2, predicted performance for PGET was lower than for UGETv1, primarily because significant object-scatter contributions in PGET's wide energy windows perturb a relatively small full-energy peak signal. Smaller energy windows might offer improvements in Objective 2 performance for PGET, but more studies are needed to quantify this potential. It may also be envisaged that geometric information may be extracted from reconstructed Objective 1-type images, to be used in Objective 2-type analyses without any need for operator-declared data. The project team and stakeholders have discussed the potential for such a procedure ("Verification Objective 1.5"), but analysis of such an approach was beyond the scope of this study.

Finally, one may note that the performance metric used for Verification Objective 1 relates to bias defects, i.e. diversion of single fuel pins. If the performance metric were defined for higher defect levels (e.g. 5% or 10% of the pins instead of the <0.5% bias defect at the event of 1 missing pin out of 264 pins in a PWR assembly) the ROC curves are expected to look considerably better also for PWR fuels. This is an area for future work.

10. Acknowledgements

U.S. participation in the JNT 1955 Phase I project has been funded by the U.S. Support Program to the International Atomic Energy Agency (IAEA) and the National Nuclear Security Administration's Office of Nonproliferation and Arms Control. Uppsala University's contributions were funded by the Swedish Radiation Safety Authority (SSM) via the Swedish Support Program to the IAEA under contracts SSM2013-85-9, SSM2014-94, SSM2015-99, SSM2016-130, and activity number 3060152-08. The computations performed by Uppsala University were partially performed on resources provided by Swedish National Infrastructure for Computing (SNIC) through Uppsala Multidisciplinary Center for Advanced Computational Science (UPPMAX) under projects p2013091, snic2013-1-296, snic2014-1-203, and snic2014-1-392. Finnish participation was supported by the Finnish Support Program to the IAEA, financed by the Finnish Foreign Ministry. The contribution by the European Commission was financed through the regular European Commission budget.

The project team appreciates the guidance of IAEA's James Ely, Misha Mayorov, and Alain Lebrun.

11. References

[1] International Atomic Energy Agency; *Special Criteria for Difficult-to-Access Fuel Items*; SG-GC-Annex-04; IAEA; 2009.

[2] International Atomic Energy Agency; *IAEA Department of Safeguards Long-Term R&D Plan, 2012-2023*; STR-375; IAEA; 2013.

[3] Lévai F, Desi S, Czifrus S, Feher S, Tarvainen M, Honkamaa T, Saarinen J, Larsson M, Rialhe A and Arlt R; *Feasibility of gamma emission tomography for partial defect verification of spent LWR fuel assemblies*; STUK-YTO-TR-189; Finnish Radiation and Nuclear Safety Authority, STUK; 2002.

[4] Honkamaa T, Levai F, Turunen A, Berndt R, Vaccaro S, and Schwalbach P; *A Prototype for passive gamma emission tomography*; IAEA Safeguards Symposium; 2014.

[5] Jacobsson Svärd S, Håkansson A, Bäcklin A, Osifo O, Willman C and Jansson P; *Non-destructive Experimental Determination of the Pin-power Distribution in Nuclear Fuel Assemblies*; Nuclear Technology, 151(1):70-76; 2005.

[6] Jansson P, Jacobsson Svärd S, Håkansson A and Bäcklin A; *A Device for Non-destructive Experimental Determination of the Power Distribution in Nuclear Fuel Assemblies*; Nuclear Science and Engineering 152(1):76 86; 2006.

[7] Jacobsson Svärd S, Håkansson A, Bäcklin A, Jansson P, Osifo O and Willman C; *Tomography for partial-defect verification - experiences from measurements using different devices*; ESARDA Bulletin, 33:15-25; 2006.

[8] Baird B; *Quantitative analysis of the fission product distribution in a damaged fuel assembly using gamma-spectrometry and computed tomography for the Phebus FPT3 test*; Nuclear Engineering and Design, 262:469-483; 2013.

[9] Holcombe S, Jacobsson Svärd S and Hallstadius L; *A novel gamma emission tomography instrument for enhanced fuel characterization capabilities within the OECD Halden Reactor Project*; Annals of Nuclear Energy, (85):837–845; 2015.

[10] Smith LE, Jacobsson Svärd S, Mozin V, Jansson P, Miller E, Honkamaa T, Deshmukh N, White T, Wittman R, Trellue H, Grape S, Davour A, Andersson P, Holcombe S and Vaccaro S; *A Viability Study of Gamma Emission Tomography for Spent Fuel Verification: JNT 1955 Phase I Technical Report*; PNNL-25995, Pacific Northwest National Laboratory, USA; 2016.

[11] Trellue HR, Fensin ML, Richard JR, Galloway J and Conlin JL; *Description of the Spent Nuclear Fuel Used in the Next Generation Safeguards Initiative to Determine Plutonium Mass in Spent Fuel*; LA-UR 11-00300, Los Alamos National Laboratory, USA; 2011.

[12] Mozin V and Tobin S; *DGSDEF: Discrete Gamma-ray Source DEFinition code*; LA-CC-10-083. Los Alamos National Laboratory, USA; 2010.

[13] Pelowitz DB; *MCNPXTM User's Manual. Version 2.6.0*; NM LA-CP-07-1473 Los Alamos National Laboratory, USA; 2008.

[14] Agostinelli A et.al.; *Geant4 a simulation toolkit*; Nuclear Instruments and Methods in Physics Research Section A, 506:250–303; 2003.

[15] C. Netterbrandt, Oskarshamns Kraftgrupp AB (OKG), Personal communication, March 2014.

[16] J. Eriksson, Forsmarks Kraftgrupp AB (FKA), Personal communication, March 2014.

[17] White TA, Jacobsson Svärd S, Smith LE, Mozin VV, Jansson P, Davour A, Grape S, Trellue N, Deshmukh NS, Wittman RS, Honkamaa T, Vaccaro S and Ely JH; *Passive Tomography for Spent Fuel Verification: Analysis Framework and Instrument Design Study*; ESARDA Symposium, Manchester, UK; 2015.

[18] Kak AC and Slaney M; *Principles of Computerized Tomographic Imaging*; IEEE Press, ISBN 0-85274-349-1, Piscataway, NJ, USA; 1988.

[19] Jacobsson Svärd S, Holcombe S and Grape S; *Applicability of a set of tomographic reconstruction algorithms for quantitative SPECT on irradiated nuclear fuel assemblies*; Nuclear Instruments and Methods in Physics Research Section A, 783:128–141; 2015.

[20] Davour A, Jacobsson Svärd S, Andersson P, Grape S, Holcombe S, Jansson P and Troeng M; *Applying image analysis techniques to tomographic images of irradiated nuclear fuel assemblies*; Annals of Nuclear Energy, 96:223-229; 2016.

[21] Shaver MW, Smith LE, Pagh RT, Miller EA, and Wittman RS; *The Coupling of a Deterministic Transport Field Solution to a Monte Carlo Boundary Condition for the Simulation of Large Gamma-Ray Spectrometers*; Nuclear Technology 168(1):95-100; 2009.

[22] Metz CE; *Basic Principles of ROC Analysis*; Seminars in Nuclear Medicine; 8(4):283-298; 1978.

[23] IAEA Nuclear Data Section, Isotope Browser. Updated 2017.

[24] Jansson P. *Studies of Nuclear Fuel by Means of Nuclear Spectroscopic Methods*; PhD thesis, Uppsala University, Sweden. Retrievable at http://urn.kb.se/resolve?urn=urn:nbn:se:uu:diva-2057; 2002.

Signatures from the spent fuel: simulations and interpretation of the data with neural network analysis

A. Borella[1], R. Rossa[1], C. Turcanu[1]

1 SCK•CEN, Nuclear Science and Technology unit,
Boeretang 200, B-2400 Mol, Belgium
Email: aborella@sckcen.be

Abstract:

In the last years, the safeguards verification of spent fuel assemblies by NDA has received increased interest also due to upcoming programmes for the geological disposal. During safeguards inspections one aims at verifying the completeness and correctness of operator declared data. One should then be able to draw conclusions on the fuel integrity and diversion of pins, as well as checking the consistency of operator declarations on initial enrichment, fuel type, burnup and cooling time. The verification of spent fuel is also important for safety aspects related to the storage of spent fuel.

The experimental observables associated to NDA of spent fuel assemblies are often a complex function of the characteristics of the fuel, its irradiation history and other variables related to the used measurement setup and devices; nowadays one often assumes that some of the variables are known to interpret the data and draw conclusions. To facilitate the interpretation of the data and draw more robust safeguards conclusions, an R&D effort is on-going at SCK•CEN and its results are given in this paper.

This work reports first about the efforts done at SCK•CEN on simulating detector response functions for different types of NDA instruments such as the Fork detector, the ForkBall detector and SINRD detectors. These responses are obtained from Monte Carlo model of the fuel and measurement setup. The spent fuel composition and radiation characteristics are taken from a spent fuel reference library developed in recent years.

A database of detector responses corresponding to 8400 cases with different fuel characteristics and irradiation parameters was then obtained. We explore the use of these simulated observables as input for data analysis algorithms aimed at uniquely characterizing the spent fuel and drawing safeguards conclusions. More specifically, we focus on the application of artificial neural networks due to their ability to generalize non-linear relationships. As a first step, cooling times smaller than 100 years were selected from the database, and several network configurations and training schemes were investigated.

Keywords: Spent fuel verification; Simulated observables; Data mining; Artificial neural network

1. Introduction

Spent fuel assemblies (SFA) are subject to verification of safeguards authorities due to their residual fissile material content. A direct measurement of the residual fissile mass is not possible with available technologies [1,2,3] and can only be estimated. The workhorses used during the verification of SFA are instruments such as the DCVD and the Fork detectors; these instruments allow to draw conclusions on the absence of gross defect in the fuel assemblies and verify the consistency of the operator declaration about fuel characteristics (e.g. fuel type, initial enrichment) and irradiation history (e.g. burnup and cooling time).

Considering the large amount of spent fuel in interim storage and the incipient opening of spent fuel repositories [4], there is an interest in developing NDA methodologies that could allow a more quantitative assessment of the spent fuel assembly before its disposal. This interest is also shared by the regulatory authorities and fuel management bodies to comply with requirements related to the safe fuel disposal; the implementation-oriented R&D activities on deep geological disposal of spent fuel and long-lived radioactive waste has been emphasised in [5,6].

The traditional nuclear signatures of spent fuel in a Non-Destructive Assay, i.e. passive neutron, gamma emission and Cherenkov glow, are mainly due to minor actinides (e.g. Cm isotopes) and fission products (e.g. Cs isotopes). Their associated observables (i.e. measured counts or light) do not provide a direct measure of the residual fissile mass and are a complex function of several variables, such as irradiation history parameters. At the moment, none of the available methods allow a unambiguous determination of all the variables. Therefore, one typically supposes that one or more of such variables are actually known, so that the number of unknowns is reduced. An example of such case is the determination of the residual fissile content which can be estimated after the burnup of the fuel has been determined from the observables for example with a calibration procedure [7].

New NDA methods are being studied and developed in the last decade[3,8]. In an ideal scenario each method could generate one or more observables where each would allow the unique determination of the quantities of interest. However, this does not seem to be the case [9].

This situation therefore calls for a methodology to disentangle the quantities of interest from the observables.

In this framework, we carried out R&D work first to simulate observables associated to NDA equipment such as the ForkBall detector and SINRD. This work is described in Section 2, where the methodology developed at SCK•CEN to simulate observables is explained. Then, in Section 3 we focus on the interpretation of the data and the extraction of the quantities of interest from the simulated observables; we describe an approach based in neutral network analysis. The obtained results are presented and discussed; outlook and recommendation for future work are given.

2. Detector response function simulations

2.1 Methodology

Due to the limited accessibility of spent fuel [10], the development and optimization of measurements methods are carried out by means of numerical calculations, often based on Monte Carlo methods [11]. Studies with Monte Carlo methods are based on models including the geometry and composition of the measurements equipment, the measurement environment and the characteristics of the radiation source.

The determination of the spent fuel composition and the characteristics of the emitted radiation can be achieved by means of evolution and depletion codes such as Origen-ARP [12,13,14] and ALEPH2 [15]. In the last years, SCK•CEN developed a spent fuel library (SFL) and investigated the impact of different factors on spent fuel composition and emitted radiation. The characteristics of spent fuel depend on quantities such as fuel type, irradiation history and initial composition of the fuel. We focussed on 17x17 PWR fuel elements and studied the change of the neutron emission by varying parameters such as initial uranium enrichment (IE), average power level (AP), duration of the irradiation cycle (DIC) and cooling time between two complete irradiation cycles (CTIC), burnup (BU and cooling time (CT) after discharge [16,17]. The current version of the SFL contains information for Low Enriched Uranium (LEU) fuel with an initial enrichment between 2% and 5% and cases with Mixed Oxide (MOX) fuel with up to 10% of Pu. The data library does not contain information about fuel with burnable poison yet.

The spent fuel library consists of entries, each corresponding to a specific irradiation case. In one entry the total neutron emission, total gamma emission, and the corresponding energy spectra are given. In addition, the abundances of 50 selected nuclides are present [10]. The data are generated in a format which is compatible with the one of an MCNP [18] input file.

The overview of the methodology developed for this study is presented in Figure 1. The used methodology relies on the development of an MCNP input file template of the measurement setup, including the fuel. The composition of the fuel and the description of the source term is then taken from the library for the desired cases, substituted in the template and the simulation is run. More information on the specific tallies is given in the next section where the considered detection system and associated observables are described. The output file of the simulation is combined with the radionuclide abundancies and source term intensity obtained from the SFL to generate the database with signatures of the different fuel assemblies.

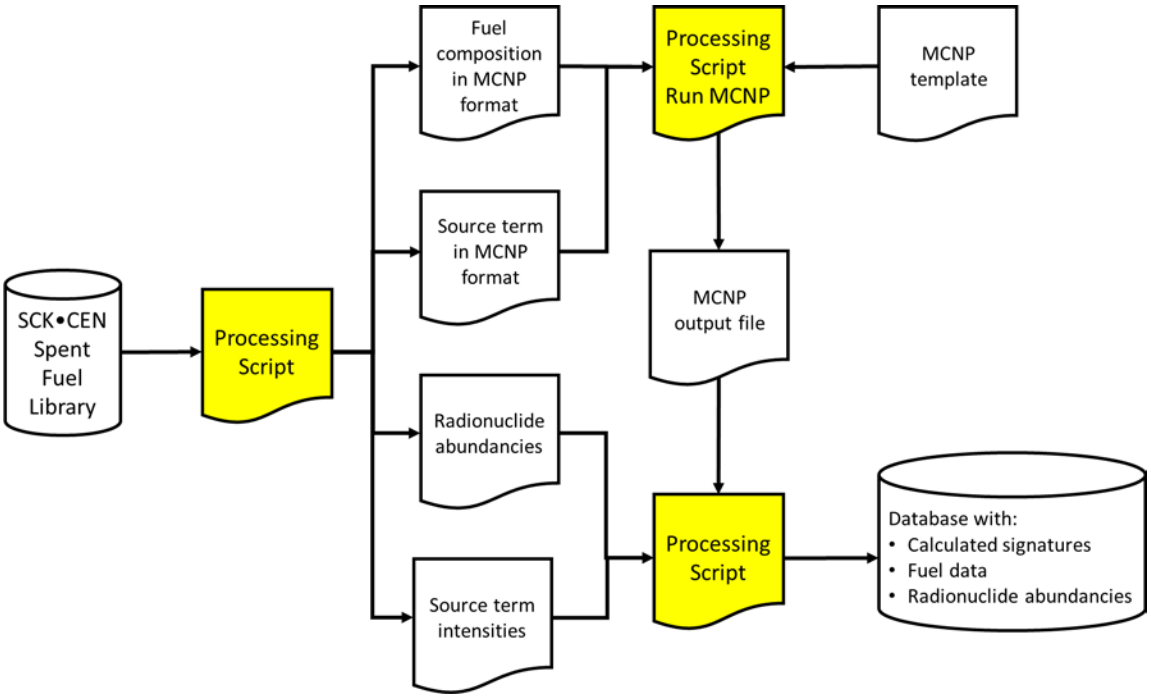

Figure 1: Overview of the methodology to generate simulated observables.

2.2 Considered detection systems

Two different types of equipment were considered. The first one is the so-called ForkBall detector [19]. This detector is designed for underwater measurements of SFA and includes features found in the Fork detector such as total neutron counts with fission chambers, total current obtained with ionization chambers and gamma-ray spectra obtained with a Cadmium Zinc Telluride (CZT) detector. The fission and ionization chamber are installed into cavities inside a polyethylene cylindrical arms wrapped with Cd. A variant without Cd was also considered.

The second detection systems implements the Self-Interrogation neutron resonance densitometry (SINRD) technique by carrying out measurements in dry conditions; this system features miniaturized fission chambers in the instrumentation channel of the SFA. The fission chambers are either bare or wrapped by neutron absorbing foils of Cd or Gd; additional details on the technique can be found in [8].

2.2.1 ForkBall detector

Separate simulations were carried out for neutrons and photons. In the neutron simulations for each entry of the SFL we determined the detection efficiency and the net multiplication factor both for the configuration with and without Cd around the polyethylene arms of the detector. The detection efficiency was estimated by multiplying to F4 tally by the (n,f) cross section of ^{235}U and amount of fissile material in the fission chambers (FM treatment). The F4 tally is used to determine the neutron fluence per starting particle and the FM treatment allows to multiply this fluence by quantities such as cross sections and attenuation coefficients that depend on the cross section. With this treatment it is possible to determine the number of fissions associated to a given flux and a given amount of ^{235}U and it is therefore possible to estimate the detector response.

While the neutrons simulations are straightforward and do not require a variance reduction technique, the gamma simulations associated to the CZT detectors require an ad-hoc procedure. Due to the presence of a shield and collimator used in the ForkBall, standard MCNP simulations are highly inefficient. A special procedure, described in [20], was therefore developed. The procedure splits the photon transport into two simulations. In a first simulation for a photon of given energy, the probability to reach CZT crystal is determined. A second set of simulations is done to determine the intrinsic detector efficiency that is the probability that an incoming photon deposits all its energy in the CZT crystal. These two quantities are then multiplied to obtain the overall full-energy detection efficiency, that is the probability that a photon of a given energy emitted by the fuel results in a full-energy peak in the crystal.

In first approximation, the overall full-energy detection efficiency does not depend on the fuel composition which still largely made up of Uranium and Oxygen. The obtained results are given in Fig. 2.

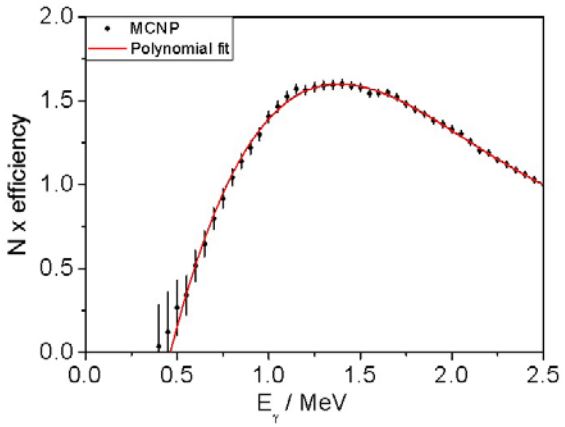

Figure 2: Normalised full-energy detection efficiency for the CZT detector in the Forkball detector.

The net peak count rate c due to a gamma ray of energy E_γ emitted by the radionuclide i is then given by

$$c\left(i,E_\gamma\right)=\varepsilon\left(E_\gamma\right)\times M_i\times A_i\times P\left(i,E_\gamma\right) \quad (1)$$

Where

- $\varepsilon(E_\gamma)$ is the overall full-energy detection efficiency
- M_i is the mass of the radionuclide in the SFA
- A_i is its specific activity
- $P(i,E_\gamma)$ is the number of emitted gamma rays of energy E_γ per decay

2.2.2 Self-Interrogation neutron resonance densitometry

For the SINRD technique the response of different types of fission chambers in the instrumentation channel of the SFA was simulated by multiplying the F4 tally by the (n,f) cross section of the active material and amount of fissile material in the fission chambers (FM treatment). The presence of shielding material was also accounted for by the FM treatment. Table 1 gives the details of the modelled detectors; more details on the choice of detectors and filters thickness are given in [8].

Active material	Filter	Energy cutoff
^{238}U	---	---
^{235}U	---	---
^{235}U	1 mm Cd	~ 1 eV
^{239}Pu	0.1 mm Gd	~ 0.1 eV
^{239}Pu	1 mm Cd	~ 1 eV

Table 1: Active materials and filters for SINRD.

As indicated in [8], the chosen signatures are sensitive both to 239Pu and 235U in the fuel.

The so-called SINRD signature and FAST to Thermal ratio (FAST/TH) are given in table 2. These quantities are

adimensional and are determined according to the procedure outlined in [8].

2.3 Data processing and results

The MCNP calculations provide observables (tallies) that are usually expressed per simulated source particles. To express the observables in absolute terms one has to take into account the source strength associated to the considered spent fuel element. This information is retrieved from the SFL and the value of the observable is determined for the considered case. Overall a database of observables and spent fuel characteristics is generated. Within the database other calculated information on the spent fuel is also included such as the content of fissile material and the multiplication factor. An excerpt of the database content is shown in Table 2.

			Neutron	Counts			CZT			
BU	IE	CT	with Cd	without Cd	SINRD	FAST/TH	$^{134}Cs_1$	^{137}Cs	$^{134}Cs_2$	^{154}Eu
GWd/t_{HM}	%	y	cps	cps			cps	cps	cps	cps
5	2	5	1.0	1.2	0.026	0.009	22.2	425.2	38.4	3.2
10	2	5	6.3	6.9	0.031	0.010	88.3	847.3	153.2	12.9
15	2	5	31.3	34.4	0.037	0.009	187.3	1263.6	324.9	28.9
20	2	5	109.8	123.6	0.038	0.009	324.4	1677.7	562.7	51.2
25	2	5	284.2	317.0	0.041	0.009	485.4	2088.6	841.8	76.2
30	2	5	600.9	652.3	0.044	0.010	647.8	2490.3	1123.5	102.4
35	2	5	1088.2	1159.4	0.046	0.010	841.1	2893.2	1458.7	130.5
40	2	5	1711.4	1877.6	0.046	0.010	1041.0	3292.0	1805.4	157.4
45	2	5	2568.7	2793.7	0.047	0.010	1213.6	3679.9	2104.7	182.9
50	2	5	3559.5	3912.6	0.049	0.010	1420.1	4071.4	2462.8	208.8
55	2	5	4813.7	5240.8	0.049	0.010	1621.7	4459.6	2812.4	232.2

Table 2: Excerpt of the database. The signatures $^{134}Cs_1$ and $^{134}Cs_2$ denote the net peak areas at 605 keV and 796 keV respectively.

3. Neural network analysis

3.1 The use of Artificial Neural Networks as function approximators

Artificial neural networks (ANN) denote a class of computational models that emulate the functioning of the biological brain, by using a number of interconnected neural units (shortly, neurons or nodes). They have been widely used in machine learning and data mining, in particular owing to their capacity to work as universal function approximators, provided certain conditions are met by the network architecture [21].

An ANN can be described as a network in which each node *i* processes the *n* input units it is connected to through an transfer (or activation) function f_i :

$$y_i = f_i\left(\sum_{j=1}^{n}\left(w_{ij}\cdot x_j - \theta_i\right)\right) \quad (2)$$

where y_i is the output of neuron *i*, x_i is the *j*-th input to node *i*, w_{ij} is the weight of the connection between input *j* and node *i,* and θ_i is the threshold (or bias) of the node. While each neuron *i* can have its own transfer function in our implementation the same transfer function was used for all the neurons in a given layer.

Neural networks have a layer for input neurons, a layer for output neurons, and one or more inner layers of neurons, also called hidden layers. Leshno et al. [21] proved that a standard multilayer feedforward (i.e. without feedback loops) ANN with a locally bounded piecewise continuous and non-polynomial transfer function can approximate any continuous function with any degree of accuracy. Feedforward networks used for function approximation problems have one or more hidden layers of nodes with non-linear transfer functions (e.g. sigmoid) followed by an output layer of nodes with linear transfer functions. This multilayer architecture allows the network to learn nonlinear relationships between input and output vectors.

Standard numerical optimisation algorithms can be used to optimise the network's performance function, often taken as the mean square error between the network's output and the network's target (real or simulated values of the function to be approximated). Various, gradient based or Jacobian based, learning algorithms [22] can be applied to adjust the weights and the biases of an ANN in a direction that optimises the performance function of the network. The most simple is the gradient descent algorithm, where the current vector $z^{(k)}$ of weights and biases is updated at each iteration *k+1* based on the current gradient g_k and the learning rate α_k, until the network converges:

$$z^{(k+1)} = z^{(k)} - \alpha_k \cdot g_k \quad (3)$$

One of the fastest training algorithms for neural networks is the Levenberg-Marquardt optimization method [23], which was used for our application.

3.2 Spent fuel characterisation based on Artificial Neural Networks

In this work, we employ ANN's to explore the use of detector response values to characterize spent fuel in terms of initial uranium enrichment, burnup and cooling time. Simulated data are used with different ANN architectures and learning algorithms. The MATLAB R2016b Neural Network Toolbox [24] was used for all data processing and analysis.

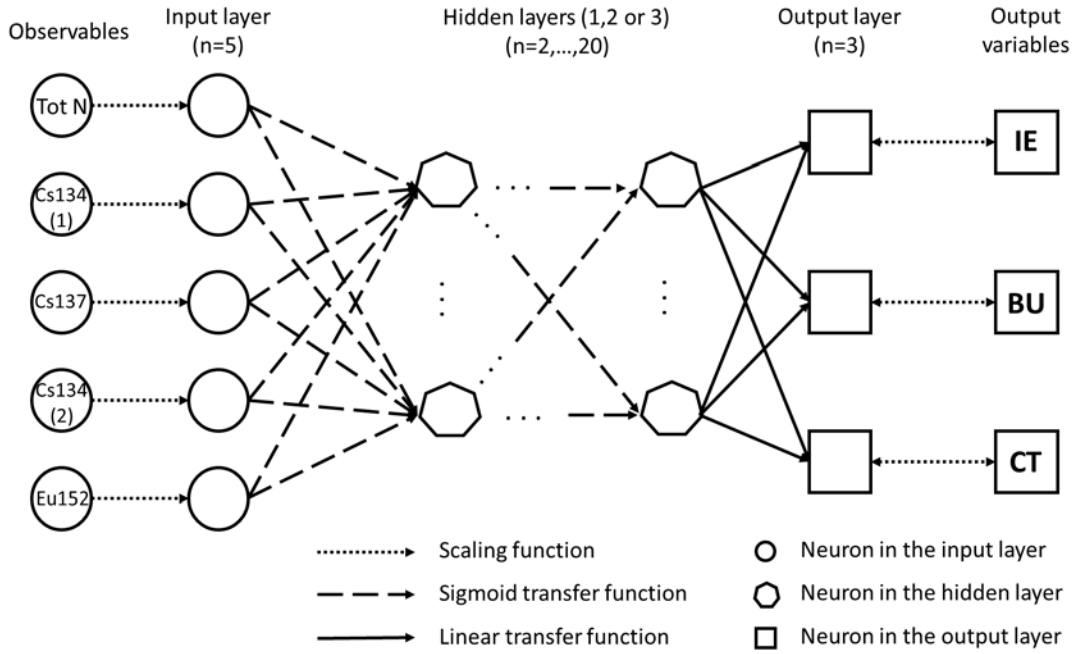

Figure 3: Artificial neural networks architecture implemented in this work.

The implemented ANN architecture is illustrated in Fig. 3. As observables, we considered total neutron counts for a Cd wrapped fission chamber and gamma rays spectroscopy data from ^{137}Cs, ^{134}Cs and ^{154}Eu. These data represent the variables in the input layer of the ANN. The BU, IE and CT represent the variables in the output layer of the ANN. While the BU and IE data were linearly spaced over their range, the CT data spanned several decades and had a logarithmical spacing. The natural logarithm was then taken to ensure that the resulting variable is uniformly distributed over its range. Both the values in the input layer (observable) and the one in the output layer (quantity to be predicted) were scaled between –1 and +1 before being fed to the network optimization algorithm.

The algorithm was applied on a subset of the database described in section 2.3. We considered data with fourteen burnup (BU) values (from 5 to 70 GWd/t_U in steps of 5 GWd/t_U), initial enrichment (IE) of between 2.0% and 5.0% in steps of 0.5%, eleven values of cooling time (CT) from 1 day to 100 years. A total of 1078 cases were considered.

For the neurons in the hidden layers we used hyperbolic tangent sigmoid transfer functions whereas for the transfer functions for the output neurons were linear. The quantity mean square error (*mse*) was used as target for minimisation. In the used *mse* each squared error contributes with the same importance as follows:

$$mse = \frac{1}{3N}\sum_{j=1}^{3}\sum_{k=1}^{N}\left(A_{k,j,calc} - A_{k,j}\right)^2 \qquad (4)$$

Where $A_{k,j,calc}$ is the value of the parameter as determined by the ANN in the output layer (Fig. 3), $A_{k,j}$ is the nominal value of the parameter. The index *j* runs over the IE, BU and CT output while *k* runs over the part of the database used for training. The calculation of the *mse* is done before the final scaling.

In the future we will define the performance in such a way that the percentage deviation enters in the definition of the quantity to be minimized rather than the absolute deviation. Note that the absolute variation in the logarithm of CT results already in a relative deviation on the CT.

The database of simulated observables and spent fuel characteristics is divided in two sets, corresponding to training and validation. The data in the validation set are used to stop training if the network performance on these data fails to improve or remains the same for a predefined number of iterations. The Levenberg-Marquardt algorithm

was used for training the network. The neural networks tested used up to three hidden layers.

3.3 Results

First we studied the impact of the number of neurons on the performance, assuming that all data set was used to train the network. The performance was then calculated on the whole database of N=1078 cases. We considered from 2 to 20 neurons per hidden layer, while the number of hidden layers went from one to three. The obtained results indicate that the performance increases in general with the number of neurons per layer and with the number of hidden layers. However, the improvement is marginal above 15 neurons, as shown in Fig. 4.

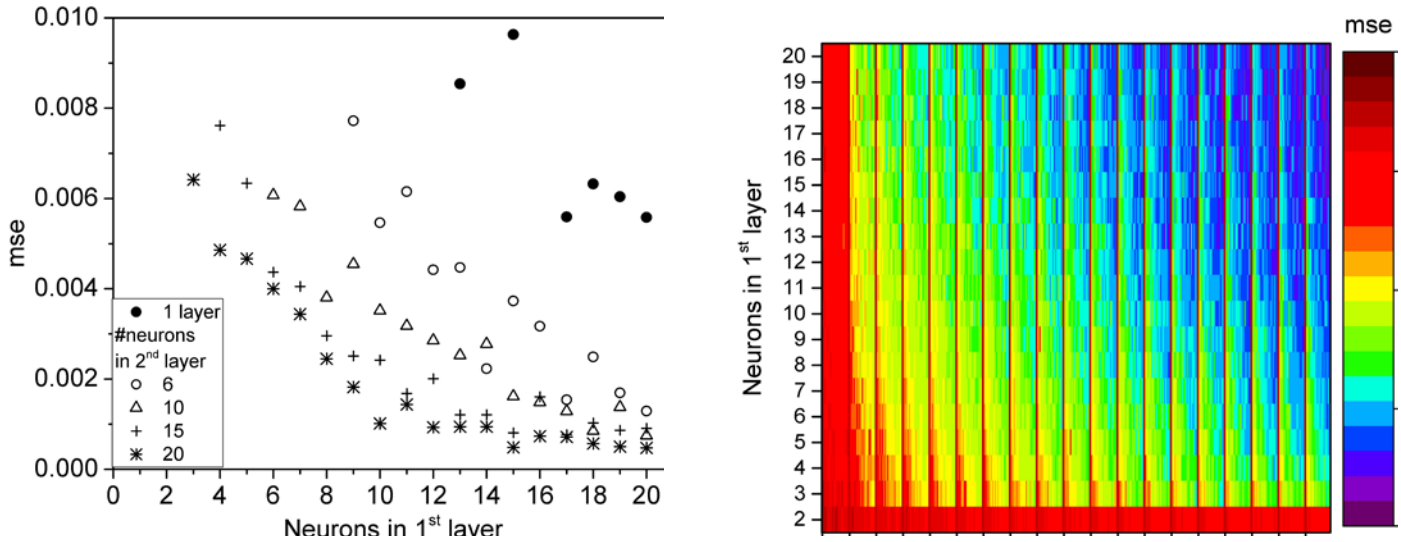

Figure 4: *mse* for ANN with one, two and three hidden layers as a function of the number of neurons. The *mse* in the right figure is limited to a maximum value of 0.01.

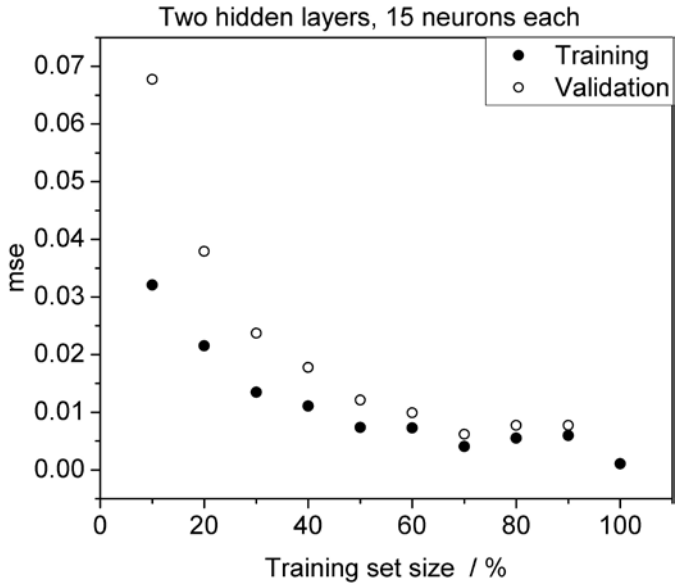

Figure 5: *mse* for ANN with two hidden layers as a function of the training set size. For both hidden layers the number of neurons was set to 15.

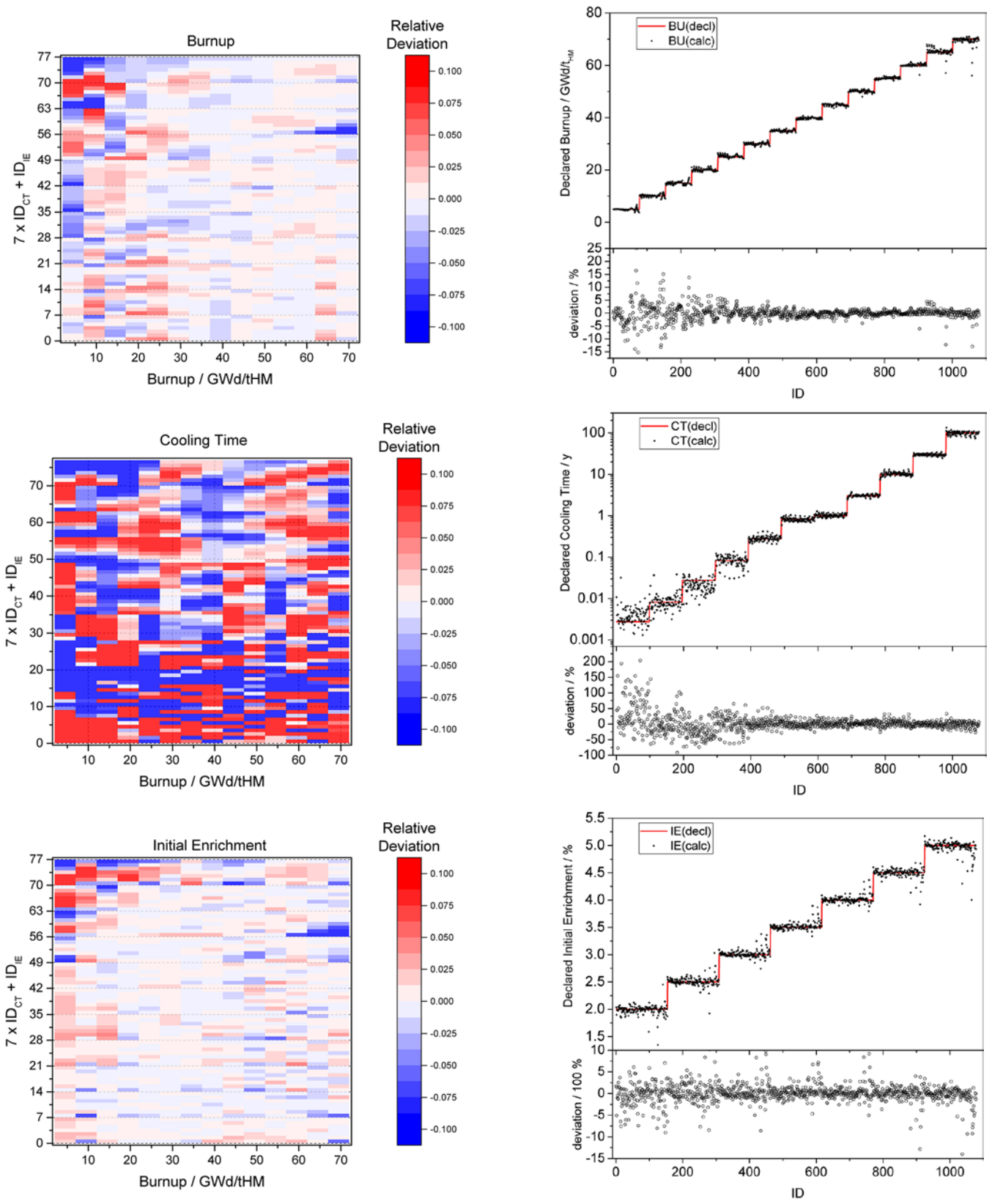

Figure 6: Deviations in the predicted values of BU, IE and CT for the considered cases. The results refer to an ANN with 3 hidden layers and 20 neurons per layer. The training set size was 50%. See the text for explanation.

In addition, we carried out calculations by changing the fraction of data used for training from 10% to 100% in step of 10%. The number of neurons was 5, 10, 15 and 20 and we considered up to three hidden layers; both the performance on the training and the validation set were computed. The assignment of individual data to the training or validation set was done randomly by MATLAB.

In general, we found that the value of the performance changes if the calculation is repeated; this is due to the fact that in the current implementation the initial values of the weights and biases of the ANN are randomly assigned [25] and this is affecting the results. For each network configuration the calculations were repeated 20 times and the average performance was calculated with its standard deviation. For the case in which 100% of the data are used for training, we observed a standard deviation in the *mse* between 12 % and 25%. By reducing the share of the training set, the standard deviations are higher; this is due to the fact that choice of the data used for training is random and changes every time; consequently, the value of the performance is affected. In addition, it was found that also the share of the training and validation data sets is not a fixed number but fluctuates around its nominal values. The resulting spread on the performance should be kept in mind when comparing different performance values.

The performance on the training set was in general better than the performance on the validation set. The difference between them was increasing by reducing the size of the training set, as shown in Fig. 5., and by increasing the number of neurons in the last hidden layer.

As expected the performance improves with the size of the training set and there is a clear difference between the performance obtained with 90% and 100% training; however, the improvement is marginal in the range 50% to 90%.

While it is of interest to identify which parameters affect the performance, it is also important to understand how performance values translate into deviation between calculated values and “real” values of BU, IE and CT. In Fig. 6, the % deviation on the value of BU, CT and IE are shown for the ANN with 3 hidden layers and 20 neurons per hidden layer with 50% training. In the plots on the left, the deviations are shown as a function of BU (X-axis) and IE and CT (Y-axis). The Y-axis is an identification number ID that is given by the formula $7 \times ID_{CT} + ID_{IE}$, where ID_{CT} and ID_{IE} range from 1 to 11 and 1 to 7 respectively and uniquely identify the case of CT and IE to which they refer. For the plots on the right the deviations are given as a function of an arbitrary case identified number (ID) that is used for a more straightforward representation; for each variable (BU, CT, IE) the ID is chosen such that the corresponding declared variable is monotonically increasing.

The results indicate that if 20 neurons and 50% of the data are used for training the ANN is capable of reproducing the value of BU within 3% for 85% of the cases, the value of IE within 2% for 80% of the cases and the value of CT within 10% for 58% of the cases.

In a more ideal case, where 100% of the data are used for training, the ANN is capable of reproducing the value of BU within 3% for 96% of the cases, the value of IE within 2% for 98% of the cases and the value of CT within 10% for 87% of the cases.

The reason why we obtain larger deviation on the CT when compared to BU and IE is not clear. The larger deviations at low value of CT can be related to the choice of observables which are less sensitive to CT smaller than 1 y.

4. Conclusions and outlook

In this work we first reported about a methodology developed to simulate detector response functions for different types of NDA instruments. A database of detector responses for 8400 cases with different fuel characteristics and irradiation parameters was then obtained. The use of the simulated observables as input for data analysis algorithms aims at uniquely characterizing the spent fuel and drawing safeguards conclusions. We explored the application of artificial neural networks due to their ability to generalize non-linear relationships on a subset of data corresponding to cooling times smaller than 100 years.

We studied the network performances in terms of mean square error as a function of the number of hidden layers, number of neurons in each hidden layer and share of the training data set. We could conclude that, within the range considered, the performances increase with the number of neurons, number of hidden layers and share of the training data set. The results show that, when all the data set is used for training, the ANN is able to reproduce the BU and IE within a few percent for most of the analysed cases, whereas the resulting CT has a larger deviation especially for values lower than 1y. The performance is significantly worse when a fraction lower than 50 % of the data set is used for training the ANN.

Future research will focus on improving the performance of the network with respect to the CT and further testing of the optimal network configuration. In particular, the performance of the network when selecting CT larger than 1 y or 10 y will be investigated. The possibility to selectively use data for training rather than randomly choose the data will also be considered. We will investigate the impact of the initial weight values. We will also try to identify which additional observables (for instance the SINRD signature) would result in an improvement of the performance. The impact of the range values of burn-up, initial enrichment and cooling time on the

performance will also be studied. The use of different performance functions will also be considered.

5. Legal matters

5.1 Privacy regulations and protection of personal data

"I agree that ESARDA may print my name/contact data/photograph/article in the ESARDA Bulletin/Symposium proceedings or any other ESARDA publications and when necessary for any other purposes connected with ESARDA activities."

5.2 Copyright

The authors agree that submission of an article automatically authorises ESARDA to publish the work/article in whole or in part in all ESARDA publications – the bulletin, meeting proceedings, and on the website.

The authors declare that their work/article is original and not a violation or infringement of any existing copyright.

6. References

[1] D. Reilly, N. Ensslin, H. Smith Jr. and S. Kreiner, *Passive Nondestructive Assay of Nuclear Materials*, NUREG/CR-5550, LA-UR-90-732, 1991

[2] *Coordinated Technical Research Meeting on Spent Fuel Verification Methods*, IAEA March 3-6 2003

[3] S. Tobin, H. Menlove, M. Swinhoe, M. Schear, *Next Generation Safeguards Initiative research to determine the Pu mass in spent fuel assemblies: Purpose, approach, constraints, implementation, and calibration*, Nuclear Instruments & Methods In Physics Research Section A, 2011, doi 10.1016/j.nima.2010.09.064

[4] Park W. S., et al., 2014. *"Safeguards by design at the encapsulation plant in Finland"*. Proceedings of the 2014 IAEA safeguards symposium.

[5] European Council Decision 2006/976/Euratom of 19 December 2006

[6] IGD-TP Implementing Geological Disposal of Radioactive Waste Technology Platform Strategic Research Agenda, www.igdtp.eu/index.php/documents/doc_download/14-strategic-research-agenda, 2011, ISBN 978-91-979786-0-6,

[7] Borella A., et al., *Spent Fuel Measurements with the Fork Detector at the Nuclear Power Plant of Doel*, 33rd ESARDA Annual Meeting, Budapest, Hungary, May 16-20 2011

[8] R. Rossa, *Advanced non-destructive methods for criticality safety and safeguards of used nuclear fuel,* PhD thesis at Université libre de Bruxelles, September 2016.

[9] S. Tobin et al., *Research into Measured and Simulated Nondestructive Assay Data to Address the Spent Fuel Assay Needs of Nuclear Repositories*, In: Proc. 57rd INMM Annual Meeting, Atlanta, Georgia, United States, 2016

[10] A. Borella, et al., *Extension of the SCK•CEN spent fuel inventory library*, 37th ESARDA Annual Meeting, 2015

[11] M.H. Kalos and P.A. Whitlock, Monte Carlo Methods. Volume I: Basics, John Wiley & Sons, NY 1986.

[12] S.M. Bowman , O.W. Hermann, L.C. Leal, C.W. Parks, ORIGEN-ARP, A Fast and Easy-to-Use Source Term Generation Tool, ORNL/CP-104231, Oak Ridge 1999

[13] I. Germina, et al. *Overview of ORIGEN-ARP and its Application to VVER and RBMK*. Oak Ridge National Laboratory, Oak Ridge, TN, 2007

[14] I. Gauld, S. Bowman, J. Horwedel, *Origen-ARP: automatic rapid processing for spent fuel depletion, decay, and source term analysis,* ORNL/TM-2005/39. January 2009

[15] A. Stankovskiy, G. van den Eynde *ALEPH 2.2 A Monte Carlo Burn-up Code,* SCK•CEN-R-5267, September 2012

[16] R. Rossa., et al., *Development of a reference spent fuel library of 17x17 PWR fuel assemblies*, ESARDA BULLETIN, No. 50, December 2013

[17] A. Borella, M. Gad, R. Rossa, K. van der Meer, *Sensitivity Studies on the Neutron Emission of Spent Nuclear Fuel by Means of the Origen-ARP Code*, In: Proceeding of the 55th INMM Annual Meeting, Atlanta, Georgia, United States, July 2014.

[18] MCNP6 Users Manual - Code Version 6.1.1 beta, LA-CP-14-00745, June 2014.

[19] A. Borella, et al., *Advances in the Development of a Spent Fuel Measurement Device in Belgian Nuclear Power Plants*.- In: Symposium on International Safeguards, Linking Strategy, Implementation and People, Book of Abstracts, Presentations and Papers, 2014, IAEA, Vienna, Austria, p. 272

[20] A. Borella, et al., *A Method To Determine Detector Response Functions In A Heavily Shielded Environment And Application To Spent Fuel Measurements With Cadmium Zinc Telluride Detectors*, In: MC2015 - Joint International Conference on Mathematics and Computation (M&C),Supercomputing in Nuclear Applications (SNA) and the Monte Carlo (MC) Method, Nashville, United States, 2015

[21] Leshno, M., Lin, V. Y., Pinkus, A., & Schocken, S., *Multilayer feedforward networks with a nonpolynomial activation function can approximate any function*, Neural networks, 6(6):861-867, 1993.

[22] Hagan M.T., Demuth H.B., Beale M.H., *Neural Network Design*, Boston, MA: PWS Publishing, 1996.

[23] Hagan, M.T., and M. Menhaj, *Training feed-forward networks with the Marquardt algorithm*, IEEE Transactions on Neural Networks, Vol. 5, No. 6, 1999, pp. 989–993, 1994.

[24] https://www.mathworks.com/products/neural-network.html

[25] MATLAB documentation, *init* function

Sealing Systems in German Spent Fuel Storage Facilities

K. Aymanns[1], A. Rezniczek[2], A. Jussofie[3], I. Niemeyer[1]

[1] Forschungszentrum Jülich GmbH
IEK-6: Nuclear Waste Management and Reactor Safety, 52425 Jülich, Germany
[2] UBA Unternehmensberatung GmbH
52134 Herzogenrath, Germany
[3] BGZ Gesellschaft für Zwischenlagerung mbH
until 31.07.2017 GNS Gesellschaft für Nuklear Service mbH

Abstract:

This paper describes the current issues related to sealing devices in the German on-site spent fuel dry storage facilities (SFSFs) related to the Germany's energy transition. Accordingly, there is a need of future investigations for improving techniques in order to achieve better radiation protection and occupational safety during safeguards verification of spent fuel casks stored in SFSFs.

In the context of phasing out nuclear energy production, the eight still operating reactors will be successively disconnected from the power grid by the end of 2022 at the latest. The nuclear material of all power reactors has to be removed prior to decommissioning of the reactor building. The defueling of reactors increases the handling operations at these sites especially by the temporary higher number of cask loadings. Accordingly, the number of transfers of these loaded casks (dual purpose: transport and storage casks) from the reactor to the SFSF will further increase as well. By end of 2027, it is foreseen that all spent fuel assemblies will have been loaded into casks. After their transfer to SFSFs, the SFSFs will have a static inventory of more than 1,000 casks, because no receipts or shipments are expected following the final reactor shut down. The spent fuel packed in casks will be stored in interim dry storages for several decades until a repository for heat generating high level waste is available. The casks may be difficult to be accessed; especially the seals attached at the protection plate on top of the approx. 6 meter high casks. A seal verification that involves the replacement of the seal will require more time and will lead to a higher radiation dose for both inspector and storage staff than easier in-situ verification or seal verification by Remote Data Transmission (RDT). Given this situation optimization of safeguards concepts and sealing systems devices applied is needed. Solutions are required to ease the verification of the casks and to minimize the exposure of the inspectors and storage staff.

Keywords: spent fuel management, spent fuel storage facilities, sealing systems

1. Introduction

Following the nuclear accident at Fukushima in March 2011, the German Government decided to immediately shut down eight of the 17 operating nuclear power plants (NPPs) and to completely phase out the use of nuclear energy for electricity production. The decisions have a significant impact on spent fuel management in Germany. After shut-down of another reactor in 2015, the eight remaining NPPs will be successively taken from the power grid by the end of 2022 at the latest. On 23 July 2013, The German Federal government entered an Act into force on the site selection process for a deep geological repository for high level radioactive waste, including spent fuel assemblies and vitrified waste [1]. This act does not specify a specific host rock type but it determines a selection of a final repository site until 2031. The repository site selection procedure should be transparent and science-based. Potentially suitable areas should be narrowed down, step by step, on the basis of scientific criteria for the best possible safety for a period of one million years. Furthermore, the selection procedure includes public participation. A commission was set up to prepare the site selection procedure and in July 2016, the commission submitted a final report including their recommendations for the German Federal Parliament (*Bundestag*). [2] The recommendations of the commissions were included in the Act on the further development of the site selection act, which entered into force on 16 May 2017 [3].

The site selection will be followed by the licensing procedure for the construction, operation and decommissioning of the repository. The decision of phasing out the production of nuclear energy provides some safeguards challenges in Germany. The defueling of reactors has a major impact on the time schedules and frequency of spent fuel handling operations in reactors, storage facilities and their associated safeguards activities. Due to the defueling of the reactors the amount of cask transfers dramatically increases. Therefore the need for long-term reliable unattended Safeguards (SG) measures must be put in place to preserve the Continuity of Knowledge (CoK).

This paper describes the current issues related to sealing devices in the German on-site dry spent fuel storage facilities. The Research Centre Jülich set up a project on this

issue. The next step in this project is to investigate options for improving techniques in order to minimize the radiation exposure of the inspectors and storage staff as well as occupational safety for verification of spent fuel casks stored in SFSFs.

2. Spent Fuel Storage Facilities in Germany

Due to the defueling of reactors, the number of transfers of loaded casks (dual purpose: transport and storage casks) from the reactor to the SFSF are increasing. Accordingly the spent fuel cask inspections for safeguards are also rising.

By the end of 2027, all spent fuel assemblies are foreseen to be loaded into dual purpose casks. Once the transfer of all loaded casks to the SFSFs is complete, the SFSFs will have a static inventory of more than 1,000 casks because no receipts or shipments are expected following the final reactor shut down. Germany's former plan to store spent fuel in central dry storage facilities at Ahaus and Gorleben had to be abandoned due to the prohibition of spent fuel transports on public traffic routes. In this context, 12 new decentralized on-site interim dry storage facilities were constructed and licensed for the storage of spent fuel assemblies. The assemblies are loaded in dual purpose casks for transport and storage – CASTOR® V-casks.

Figure 1: Design of CASTOR Type V19 and V/52 (Copyright: GNS)

The licensed storage period of all German SFSFs is limited to 40 years beginning with the emplacement of the first spent fuel containing cask in the storage building. The licensed mass of heavy metal (HM) in the on-site dry SFSF varies between 450 Mg and 2,250 Mg and amounts to 3960 Mg (Ahaus) and 3800 Mg (Gorleben). The storage capacities of the on-site dry SFSFs range between 80 and 192 CASTOR® V-casks [7].

The construction of the 12 on-site dry SFSFs is based on three different concepts (acronyms will be detailed later): the STEAG, the WTI and the tunnel concept. They were constructed as storage halls from steel concrete (at the Neckarwestheim site in the form of storage tunnels). The STEAG concept has been applied at six North German sites at Brokdorf, Krümmel, Brunsbüttel, Grohnde, Lingen and Unterweser. The WTI concept has been applied at the five sites at Biblis, Philippsburg, Grafenrheinfeld, Isar and Gundremmingen located in the southern part of Germany. The tunnel concept at Neckarwestheim was developed as a special solution due to site-specific conditions [4].

In addition to the two central SFSFs and the twelve on-site dry storage facilities, two local interim dry storage facilities at Greifswald (ZLN) and Jülich are operated in Germany [4].

STEAG Design:

The design characteristics of the STEAG concept (designed by the company STEAG encotec GmbH) include a one-nave building with thick concrete structures (Figure 1). The wall thickness is about 1.2 m and the roof thickness is about 1.3 m. The distance between each cask is approximately 55 cm [4].

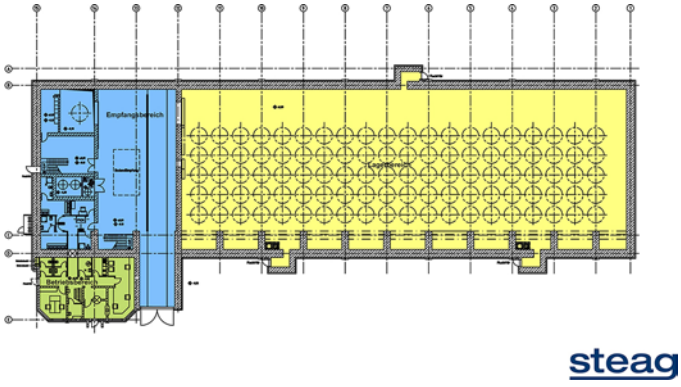

Figure 2: SFSF built as STEAG Concept [4]

WTI Design:

The WTI concept (designed by the company of consulting engineers Wissenschaftlich-Technische Ingenieurberatung GmbH) is a two-nave building with two separate storage halls; the wall thickness is around 0.85 m, respectively, and the roof thickness about 55 cm (Figure 2). The distance between each cask is approximately 50 cm [4].

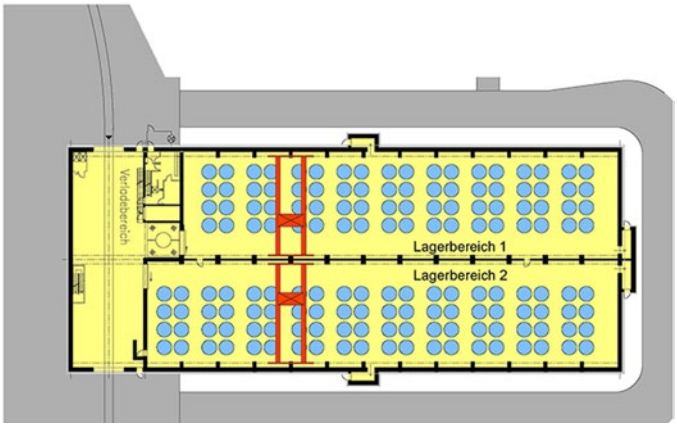

Figure 3: SFSF built as WTI Concept [4]

Tunnel Design:

The tunnel storage was designed to the specific on site geological conditions. The facility consists of an entrance building, which is arranged aboveground, two tunnel tubes running parallel in east-western direction, which are connected at their ends by a tunnel, and an exhaust air system and an escape construction (Figure 3). The distance between each cask is approximately 44 cm [4].

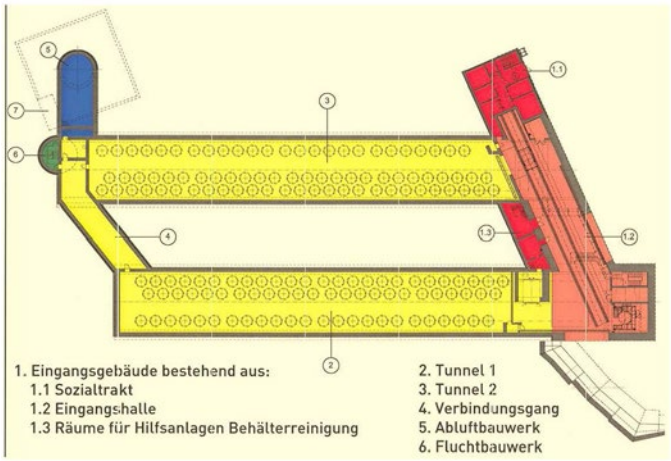

Figure 4: SFSF built as tunnel concept [4]

The dense packing of casks can be seen on the three layouts of the SFSFs. Due to this arrangement; casks cannot be moved between other casks. Movements of CASTOR® casks over other casks of this type with a height of approx. 6 m is technically not possible due to the maximum lifting height of the crane, which is 9 m from the ground. If a cask has to be transferred into the maintenance room (located inside the entrance area), all casks in the rows in front of this cask have to be transferred individually to a buffer area first in order to allow the movement of the selected cask.

3. Safeguards Implementation in German Spent Fuel Storage Facilities

The IAEA has drawn the 'broader conclusion' for Germany in March 2009 for the first time. The implementation of integrated safeguards started with in 2010. This was also the starting point for implementing integrated safeguards in the German SFSFs. Since the IAEA concluded on the absence of undeclared nuclear material and activities in Germany, the safeguards objectives changed. The requirements to timeliness for spent fuel verification and detection probability were lowered; the quarterly routine inspections were replaced by randomly performed inspections with a short notice of 24 h and a probability of occurrence of 20 percent in a given facility. The inspection-interval for physical inventory verification (PIV) continues to take place annually.

3.1 C/S of long term static dry storage casks

Regarding the long-term storage of spent fuel in SFSFs, any safeguards inspection plan for the dry interim storage should be ruled by two main aspects. First, CoK of the nuclear material flow by Containment & Surveillance (C/S) measures from the reactor to the storage facility and during the storage period should be maintained. Second, verifying the nuclear inventory of the casks by counting and identification should involve an evaluation of the C/S system and, as a back-up, non-destructive-analysis (NDA) measures on the CASTOR®-casks as appropriate in the hypothetical worst case, where all safeguards measures, seals and surveillance fail [5, 8]. In order to avoid this worst case, different sealing systems are applied for cask sealing in combination with camera surveillance.

For states under integrated safeguards, such as Germany, the IAEA requires maintaining CoK during transport of CASTOR® V-casks to their storage position and during their long term storage. Due to the inaccessibility of the nuclear material during interim dry storage, casks loaded with spent fuel should be under dual containment and surveillance (C/S). In order to meet this requirement, two independent sealing systems using different physical principles are applied by IAEA and EURATOM during long-term storage, mostly supplemented by surveillance. Three different types of sealing systems (see Table 1) are currently used at German SFSFs.

Code	Equipment name	Description/ Application
CAPS	Cap seal (metallic)	Passive seal, cable not monitored. After removal the verification of seals is only possible at IAEA or EURATOM Headquarters.
COBRA	Fibre optic general purpose seal	Passive seal, Multi Fibre optic seal; reflective particles incorporated in the seal body provide unique identifier; in situ verifiable
EOSS	Electronic Optical Sealing System	Active seal. Reusable seal consisting of a fibre optic loop and electronical seal. Light pulses monitor the loop, and every opening and closing of the seal is stored in the seal. A dedicated reader is used to verify the seal.

Table 1: Sealing Systems used in German SFSF [6]

3.2 C/S without inspector following loading of Castor casks

The loading and transfer of CASTOR® V-casks is not always as straight forward as desirable due to the drying process necessary before closing the cask and the seal can be applied. The residual moisture in the cask has to meet special criteria and the time needed to reach these

criteria is difficult to predict. Practical experience shows a range from 10 to 200 hours. To avoid inspectors having to remain on-site or on-call while the cask is drying, the IAEA and EURATOM proposed an approach to delegate the task of applying the seals to the operator when the inspectors are not present. After the spent fuel has been loaded into the cask the operator seals the cask by using the COBRA seal, the electronic seal EOSS and the EOSS seal interface. The equipment needed for the sealing procedure is shown in figure 6.

Figure 5: Equipment needed by the operator for applying the COBRA and the EOSS seal [9]

Figure 6 shows the bolts, where the sealing wires are threaded. Two bolts each are used for the COBRA and the EOSS fiber-optic cables.

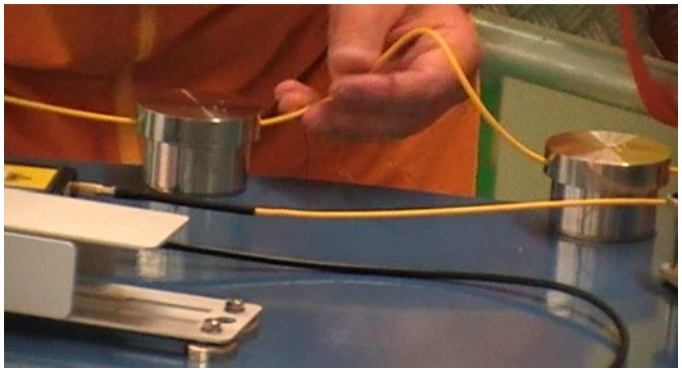

Figure 6: Threading the EOSS fiber-optic cable. Two additional bolts are used for COBRA sealing [9]

This procedure is recorded by installed safeguards video surveillance. The EOSS seal interface guides the operator through the sealing procedure and confirms its successful termination as a storable message. [7]. Casks that were sealed by the operator in the reactor and transported to the storage facility are there verified after finishing the loading campaign by the two inspectorates of EURATOM and IAEA; at the same time the EOSS seals are replaced by metal seals and/or COBRA seals. Some SFSFs use COBRA seals as group seals. In one SFSF individual CASTOR®-casks are sealed by COBRA seals and additionally groups of those casks are connected by a single EOSS seal as a group seal.

4. Discussion and Outlook

The verification of sealing systems currently used at German SFSFs is a very arduous and time consuming task due to the spatially limited storage configuration.

The obligation to replace a metal seal and a COBRA seal in regular intervals is difficult to fulfill in view of the small distance between casks, which excludes the possibility to transfer a cask between other casks into the maintenance room and requires the application of special climbing aids instead of elevating work platforms enabling a seal exchange at a height of approx. 6 m. Seal verification or seal renewing that involve the replacement of the seal on the top of the casks lead to a higher radiation dose for both inspector and storage staff than the easier in-situ verification or seal verification by RDT. Work safety rules do not allow unsecured movements between casks and thus enforce time consuming positioning of persons for each cask separately. Near the casks the radiation level is higher than elsewhere. The principle guideline for radiation protection „As Low As Reasonably Achievable“ (ALARA principle) calls for a reduction in the duration of stay in this environment as far as possible. Efforts should be made to minimize the dose rate for inspectorate and staff in this area for example by using RDT systems. According to the document of IAEA and EURATOM “Partnership Approach under Integrated Safeguards for Spent Fuel Storage Facilities” remote monitoring in SFSFs should be used to the extent possible in order to increase the effectiveness and efficiency of Safeguards implementation.

Given this situation, there is an urgent need to optimize the safeguards concept and to tailor the sealing devices to the specific conditions of an interim SFSF in a static operation. Solutions are required to ease the verification of the casks and to minimize the exposure of the inspectors and storage staff. This is the main goal of our current investigations. It requires reviewing suitable current and future sealing systems as well as complementary available technologies, such as laser based systems or neutron monitors, and evaluate pros and cons of their application to safeguarding spent fuel storage casks in the German SFSFs. This will be carried out in the next steps of this project.

5. Acknowledgements

This work was supported by the Federal Ministry for Economic Affairs and Energy, Germany, through the German Safeguards Support Programme to the IAEA and the Programme “Neu- und Weiterentwicklung von Safeguardstechniken und -methoden” (FKZ 02W6263).

6. References

[1] Gesetz zur Suche und Auswahl eines Standortes für ein Endlager für Wärme entwickelnde radioaktive Abfälle und zur Änderung anderer Gesetze (Standortauswahlgesetz – StandAG) vom 23. Juli 2013 (BGBl. I 2013, Nr. 41, page 2553)

[2] Kommission Lagerung hoch radioaktiver Abfallstoffe - Abschlussbericht: Ein faires und transparentes Verfahren für die Auswahl eines nationalen Endlagerstandortes, 5. Juli 2016

[3] Gesetz zur Fortentwicklung des Gesetztes zur Suche und Auswahl eines Standortes für ein Endlager für Wärme entwickelnde radioaktive Abfälle und anderer Gesetze vom 05.05.2017 (BGBl. I 2017, Nr. 26, issued on 15th May 2017, page 1074)

[4] „Dezentrale Zwischenlager, Bausteine zur Entsorgung radioaktiver Abfälle“, Bundesamt für Strahlenschutz, Salzgitter, Germany, 2005

[5] Jill Cooley „Integrated Safeguards – Current Status of Development and Plans for Implementation”, Department of Safeguards, International Atomic Energy Agency, Vienna, Austria, IAEA-SM- 367/3/01

[6] „Safeguards Techniques and Equipment: 2011 Edition”; International Nuclear Verification Series No. 1 (Rev.2), International Atomic Energy Agency, Vienna, Austria, 2011

[7] A. Jussofie, R. Graf, W. Filbert, “German Approach to Spent Fuel Management”, IAEA-CN-184/30; Symposium on International Safeguards: Preparing for Future Verification Challenges, Vienna, Austria, 2010

[8] A. Jussofie, K. van Bevern, M. Hahn, W. Trautwein, “Germany’s Accelerated Exit from Nuclear Energy: Challenges and Perspectives with regard to Safeguards” IAEA-CN-220/Symposium on International Safeguards: Linking Strategy, Implementation and People, Vienna, Austria, 2014

[9] Kernkraftwerk Unterweser, Preussen Elektra GmbH

Self-calibration Method for Dead Time Losses in Neutron Counting Systems

K.D. Ianakiev[1], M.L. Iliev[1], M.T. Swinhoe[1], A.M. LaFleur, C. Lee[1, 2]

[1] Los Alamos National Laboratory, Los Alamos, NM 87545
[2] KAERI, Republic of Korea

Abstract:

Most of the safeguards assay for quantitative characterization of SNM (mass, multiplication, random neutron contribution) are based on neutron measurements and rely exclusively on the counting information from very efficient, but slow He-3 proportional tubes. The response of neutron detection systems is inevitably affected by Dead Time (DT) losses that are generally caused by very complex and convoluted processes, which are difficult to take into account for corrections (for example, the DT losses for bipolar shapers differ from those of unipolar shapers). Therefore an empirical approach for calculating the DT losses assuming exponential (paralyzing) DT using measurements with two Cf-252 sources with known activities was established as current practice for many safeguards neutron counting systems. The availability of a very wide range of such Cf-252 calibration sources becomes the limiting factor for extending the deadtime correction calibration over a sufficient dynamic range to reach the conditions of real measured material.

In this paper we present a novel self-calibrating method for the determination and correction of deadtime losses that uses directly the neutron signal from real measured material. The count rate from the material is measured with two configurations of the preamplifiers: a standard configuration of the preamplifiers and tubes, corresponding to a nominal (100%) load per preamplifier and a second "deadtime measurement" configuration, where every two neighbouring clusters of He-3 tubes are connected together to a single preamplifier, corresponding to 200% load per preamplifier. A proof of principle DT calibration measurement over a wide dynamic range exceeding 10^6 reactions/sec using a 14 MeV neutron generator, demonstrated experimentally the viability of this method. The method produces the DT correction factor at every measured counting rate. The results show the very important observation that the correction factor does not fit with either fully paralyzing or fully non-paralyzing dead time models. Using either model could lead to substantial deadtime correction errors.

Explanation of DT behaviour and implementation aspects of this method in typical safeguards neutron systems (already in use or to be built) such as differential dieaway, coincidence and multiplicity counting will be discussed.

Keywords: neutron counting losses; dead time models; dead time correction; self-calibration; KM200

1. Introduction

The analytical measurements using pulse mode radiation detection systems rely on proportionality between incident and recorded radiation events. That proportionality is limited by the inevitable counting losses due to: a) random time distribution and intensity of the incident radiation events and b) the minimum response time of the detection system to process and record two separate detection events, called Dead Time (DT). The DT in a typical gamma spectroscopy measurement system has two components: a) one from the duration of shaped pulses resulting from convolution between the detector current pulse *I(t)* and time response (weighting function W(t)) of the selected pulse processing electronics and b) electronics time to detect the pulses above the event threshold, measure (typically the ADC measurement time) and record the amplitude of the pulse. Because the emphasis of gamma spectroscopy instrumentation is on preserving the energy information, unipolar shaping with time constant much longer than detector current pulse is used for better noise and ballistic deficit suppression. In order to correct these losses two DT loss models are conventionally applied: a) paralyzing DT model $N_{meas}=N_{in}*\exp(-N_{in}*t_d)$, where t_d is a deadtime constant used to correct the losses due to pile-up of superimposed unipolar pulses that prevents a new event being detected and recorded before the pile-up pulse goes below the event discriminator threshold and b) non-paralyzing DT model $N_{meas} =N_{in}/(1+N_{in}*t_d)$ used to correct the time for a pulse amplitude measurement process that is triggered by the event discriminator signal. These two models have similar behaviour at incident rate where DT losses are relatively low ($N_{in}* t_d << 1$) but very different behaviour at elevated rates and high DT losses [1, 2]. The uniform pulse shape due to time constants longer than the detector pulse and low busy time amplitude dependence due to very low event detection threshold (set just above the noise) provide a good match with constant extension of the DT of the paralyzing model. Therefore the paralyzing DT model combined with very effective pile-up

rejection became an industry standard for correction of DT losses in gamma spectroscopy.

On the contrary, the emphasis in neutron counting systems is to preserve the counting information from the 3He detector despite the long (microseconds) and very fluctuating shape of the current pulse (see Fig 1a). Therefore with almost no exceptions the signal processing of existing electronics (Amptek-11, PDT, KM200) is based on bipolar shaping with time constant much shorter than the duration of the detector current pulse in order to reduce the dead time [3] as it is shown on Fig 1b.

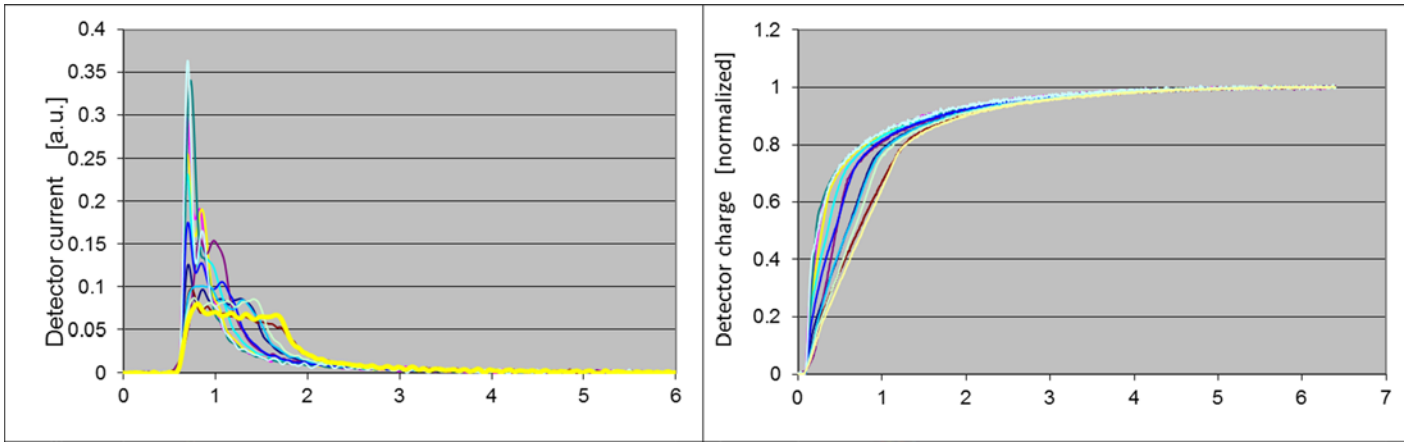

Fig. 1a: Normalized charge pulses (left) and corresponding current pulses. The fluctuation of charge collection time (left) result in very wide amplitude and duration of the current pulses (right)

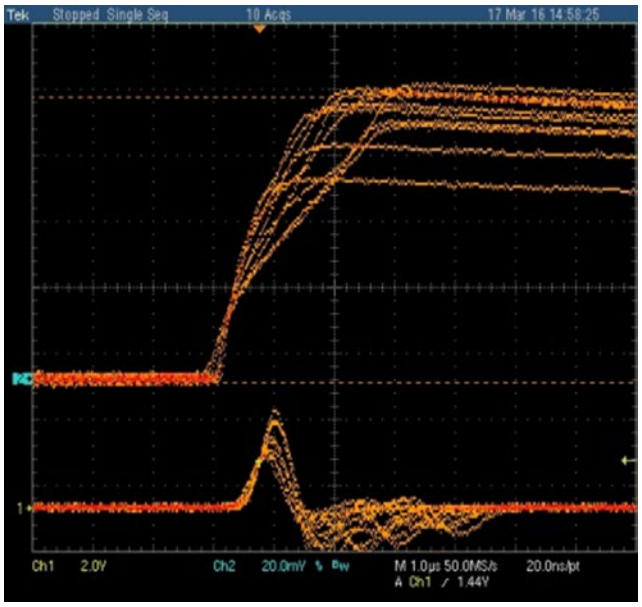

Fig.1b Charge pulses (top) of N2 gas fill He3 tube and corresponding bipolar output pulses from KM200-SLOW shaper [4]

The fluctuation of differentiated current pulses causes artificial parasitic triggering (the so called double pulsing effect). This effect is the main factor governing the selection of time constant as a trade-off between dead time and minimal amount of artificial pulses. We would like to stress that the average value of a bipolar pulse is zero (the areas of positive and negative lobes are equal). This leads to substantial differences in high count rate behaviour between unipolar and bipolar shapers:

- The pulse pile-up spectrum in a unipolar shaper is superimposed on the right (higher energy) versus the original spectrum while the pile up in the spectrum from a bipolar shaper is superimposed in both directions versus the original non-pileup spectrum.
- The pile-up of unipolar pulses causes updating dead time and is described very well with the exponential dependence of the paralyzing DT model (zero output at Nin* t_d >> 1). **Because the bipolar pulse has zero average value, the average value of superimposed bipolar pulses will be zero regardless of the input counting rate.** The intuitive implication is that the paralyzing DT model would not describe well the DT behavior of a bipolar shaper at elevated DT.

2. Description of the neutron detection system of the PUNITA facility and experimental setup

As described in the previous section, the DT losses in neutron counting systems are very complex and convoluted processes, which are difficult to take into account for corrections. Therefore an empirical approach for calculating the DT losses assuming exponential (paralyzing) DT using measurements with two **^{252}Cf** sources with known activities was established as current practice for many safeguards neutron counting systems [5].

The following equations are used to calculate the dead time corrected singles (S_C) and doubles (D_C) rates:

$$S_C = S_M e^{\frac{\delta S_M}{4}} \quad (1)$$

$$D_C = D_M e^{\delta S_M} \quad (2)$$

where S_C and D_C are the true singles and doubles rates, S_M and D_M are the measured singles and doubles rates, respectively, and δ is the total deadtime coefficient given by:

$$\delta = \left(A + B \cdot S_M \cdot 10^{-6}\right)\mu s \quad (3)$$

where A and B are constants. The dead-time parameter B is approximated as $B = A^2/4$. These standard deadtime correction parameters (A and B) are applied to the singles and doubles rate for both coincidence and multiplicity analysis. The triples deadtime correction uses the multiplicity deadtime parameter. The multiplicity deadtime parameter was approximated as A/4.

It is important to note that there are several measurement methods that can be used to determine A and B for a particular detector system.

1. ***Doubles to Singles Ratio*** – measure the singles and doubles rates from at least 4 ^{252}Cf sources that span a large range in activity, plot ln(D/S) versus Singles rate, use a quadratic curve to fit the data and determine A.
2. ***Source Intensity Ratio*** – measure a strong and a weak ^{252}Cf source with very well-known neutron yields, set the ratio of the deadtime corrected doubles rates equal to the known ratio of ^{252}Cf yields, and iteratively solve the equation for A.
3. ***Paired Source*** – measure 2 high yield ^{252}Cf sources separately and then together, set the deadtime corrected doubles rate from measuring sources together equal to the sum of the deadtime corrected rates from measuring the sources separately, and iteratively solve the equation for A.

The system deadtime is affected by properties of the detector (e.g. polyethylene design, detector fill gas) and by the signal processing electronics (e.g. number of preamps, shaping time). The deadtime loss of neutron pulses increases at higher count rate, and it can be corrected empirically [6,7,8]. These techniques can provide excellent results for measurement samples with count rates in the range of the calibration sources used. But applications such as spent fuel, plutonium waste and MOX storage canisters, uranium and trans-uranium ingots, etc. often require operation at count rates many times the count rate of the empirical calibration. The reliance of the present deadtime calibration method on a single measurement point therefore introduces potential limitations, such as:

- It is difficult to find and measure ^{252}Cf sources in the entire dynamic range of the detection system.
- The count rates and neutron correlation characteristics of a ^{252}Cf calibration source are different from those of a measured SNM.
- And last but not least, the dead time behavior of bipolar shapers used in the ^{3}He electronics can differ from the calculated values based on the simple assumption of paralyzing DT model with a fixed deadtime constant even at low or moderate count rates.

3. Self-calibration method for counting loss correction

In order to address the challenges listed above, LANL has developed a new self-calibrating method for the determination and correction of dead time losses that uses the neutron signal from real measured material directly [9]. It is based on measuring the same incident reaction rate in the detector (count rate) from the material, N_{in}, with two configurations of preamplifiers: a standard configuration of preamplifiers and tubes, corresponding to a nominal (100%) count rate load per preamplifier and a second "dead time measurement" configuration, where every two neighbour clusters of detectors are connected together to a single preamplifier, corresponding to 200% load per preamplifier. An illustration of the described measurement is shown on Figure 2.

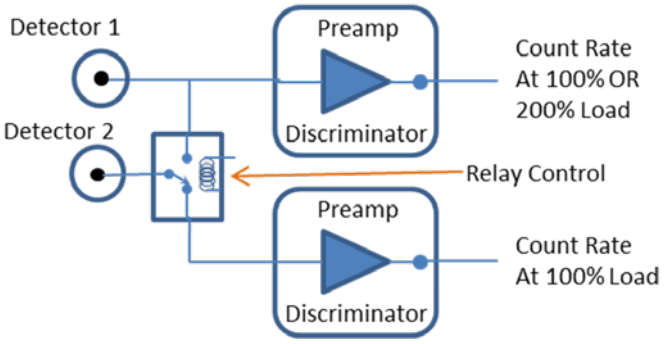

Figure 2: Illustration of detector switching method for dead time self-calibration. When the relay switch at the preamps' input is in its initial position, both channels see the normal count rate load ($N_{100\%}$). When the relay is switched, the bottom preamp sees no detector signal and the top sees the double count rate load ($N_{200\%}$). The TTL output of both preamplifiers are summed in OR circuitry.

The expression for the dead time constant (t_d) and the corrected input count rate per channel (N_{IN}) can be found using the following analysis:

First assuming the dead time in the system is paralyzing:

$$N_{100\%}\left(sum\ of\ two\ channels\right) = 2\times N_{IN}\, e^{-N_{IN} t_d} \Rightarrow \quad \frac{N_{100\%}}{2N_{IN}} = e^{-N_{IN} t_d} \qquad /4/$$

$$N_{200\%} = 2N_{IN}\, e^{-2N_{IN} t_d} \Rightarrow \quad \frac{N_{200\%}}{2N_{IN}} = (e^{-N_{IN} t_d})^2 \qquad /5/$$

Where, $N_{100\%}$ is the measured count rate when one detector is connected to one amplifier, and $N_{200\%}$ is the measured count rate when two detectors are connected to one amplifier.

Observing that $e^{-N_{IN} t_d}$ is present in both expressions, we can eliminate the t_d unknown and simplify:

$$\frac{N_{200\%}}{2N_{IN}} = \left(\frac{N_{100\%}}{2N_{IN}}\right)^2$$

Solving for N_{IN}, we get an expression for the incoming count rate that involves only measured quantities:

$$N_{IN} = \frac{{N_{100\%}}^2}{2N_{200\%}} \qquad /6/$$

We can also solve for the value of the paralyzing dead time.

$$t_d = \frac{-2N_{200\%}}{{N_{100\%}}^2} ln\left(\frac{N_{200\%}}{N_{100\%}}\right) \qquad /7/$$

Secondly we can apply the same method with the assumption of non-paralyzing dead time. In this case the measured count rates are:

$N_{100\%} = N_{IN}\,(1 - N_{100\%}\, t_d)$ and $N_{200\%} = 2N_{IN}\,(1 - N_{200\%}\, t_d)$. /8/

Then, $\frac{N_{100\%}}{N_{200\%}} = \frac{1 - N_{100\%}\, t_d}{2(1 - N_{200\%}\, t_d)}$.

In the above equation t_d is the only unknown, so solving for t_d gives

$$t_d = \frac{2}{N_{200\%}} - \frac{1}{N_{100\%}}. \qquad /9/$$

Substituting t_d in the equation /5/ and solving N_{IN} for gives

$$N_{IN} = \frac{N_{100\%} N_{200\%}}{2(N_{200\%} - N_{100\%})}.$$

4. FNEM detector and DT calibration using classical dual source method

The classical paired source DT correction method was used to calibrate a new detector developed at KAERI called the Fast Neutron Energy Multiplication (FNEM) detector. This detector utilizes both FNEM and passive neutron albedo reactivity (PNAR) methods. FNEM consists of two rings of three ^{3}He tubes where 1 ring is located close to the sample cavity and the other ring is located far from the sample cavity (see Figure 3). The FNEM method is sensitive to the induced fission rate by fast neutrons and PNAR is sensitive to the induced fission rate by thermal neutrons. The total induced fission rate is proportional to the amount of fissile material in the sample being measured.

The efficiency for each ring of the FNEM detector was measured to be ~6.7% for the inner ring and ~0.75% for the outer ring. Since the FNEM method is based on multiplication (induced fission) in the measured sample, this detector was designed to measure high count rate samples (>1 x 10^6 n/s) and thus understanding the DT correction is essential to its calibration and characterization [10].

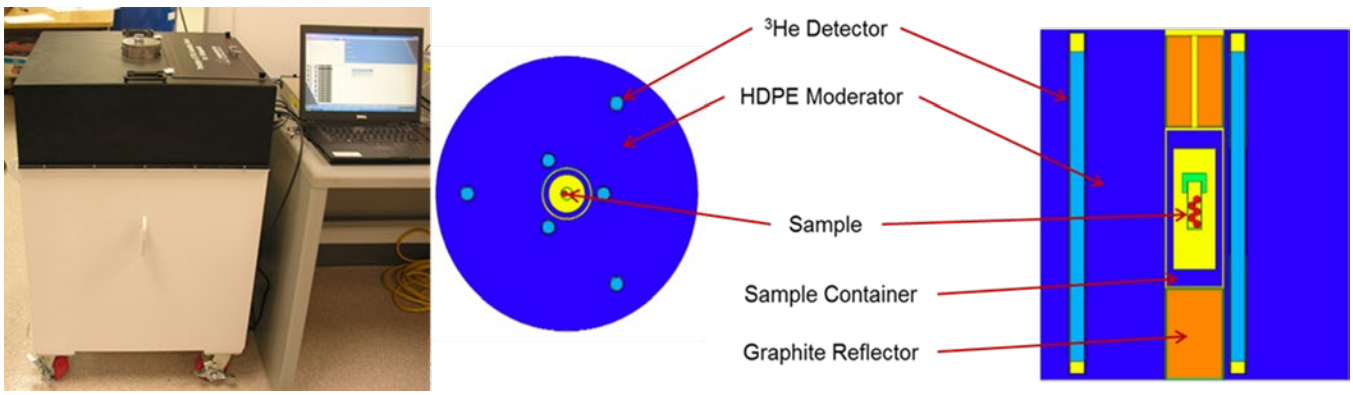

Figure 3: Picture and schematic of FNEM detector.

Using the paired source method described earlier in this paper, the DT coefficients (A and B) for FNEM were measured using two ^{252}Cf sources with intensities of 1.57×10^{6} n/s and 1.55×10^{6} n/s at LANL. The iteratively calculated coefficients for dead time were 2.147×10^{-6} for A and 1.152×10^{-12} for B, which were then applied in the INCC software. The fractional count loss of the inner ring was determined to be about 6.3% and 12.1% for the 0.12 and 0.25 MHz count rates, respectively [10]. It should be noted that the incident neutron rate used for deadtime measurement corresponds to about 3% of the maximum expected emission from a high count rate multiplying sample.

5. DT calibration using neutron generator and LANL self-calibration method

Because the exponential paralyzing DT model may not fit well the real behaviour of the bipolar shaper of PDT-110A , the extension of the calibration from two ^{252}Cf sources by a factor of 30 may lead to substantial count rate (respectively SNM mass) correction error. Therefore, we have used a neutron generator placed in the centre of the FNEM cavity as a neutron source with variable intensity of neutron flux. It should be noted that unlike the radioactive sources , we don't know the exact value of the NG neutron flux.

The neutron flux was controlled by changing the neutron generator's acceleration voltage and beam current, which provides a dynamic range greater than a factor of 10. Two types of measurements were performed: one with PDT-110A and another with KM200 electronics with a switching relay that allows us to measure $N_{100\%}$ and $N_{200\%}$. The KM200 electronics were mounted on an aluminium junction box that contains the HV and a switching relay circuitry. The preamps were gain matched and the plateau characteristics were tested in both switching configurations to make sure that the additional input-capacitance does not change the counting characteristics of KM200. This is possible because a) the gain of KM200 charge sensitive amplifiers does not change by small variations of input capacitance and b) the threshold is set at 40V above the plateau knee and thus can tolerate few tens of percent change of amplifier gain. We switched only the top two detectors (#1 and #3) in the first ring of the FNEM shown on Fig.4. During the first measurement, each detector was connected to its own preamplifier. We recorded the individual count rates to make sure that each detector sees roughly the same count rate. We used the average of the count rates of detector 1 and detector 3 to represent $N_{100\%}$. The second measurement was performed with detector #3 disconnected from preamplifier 3 and connected to preamplifier 1 which provided the count rate in DT measurement condition $N_{200\%}$.

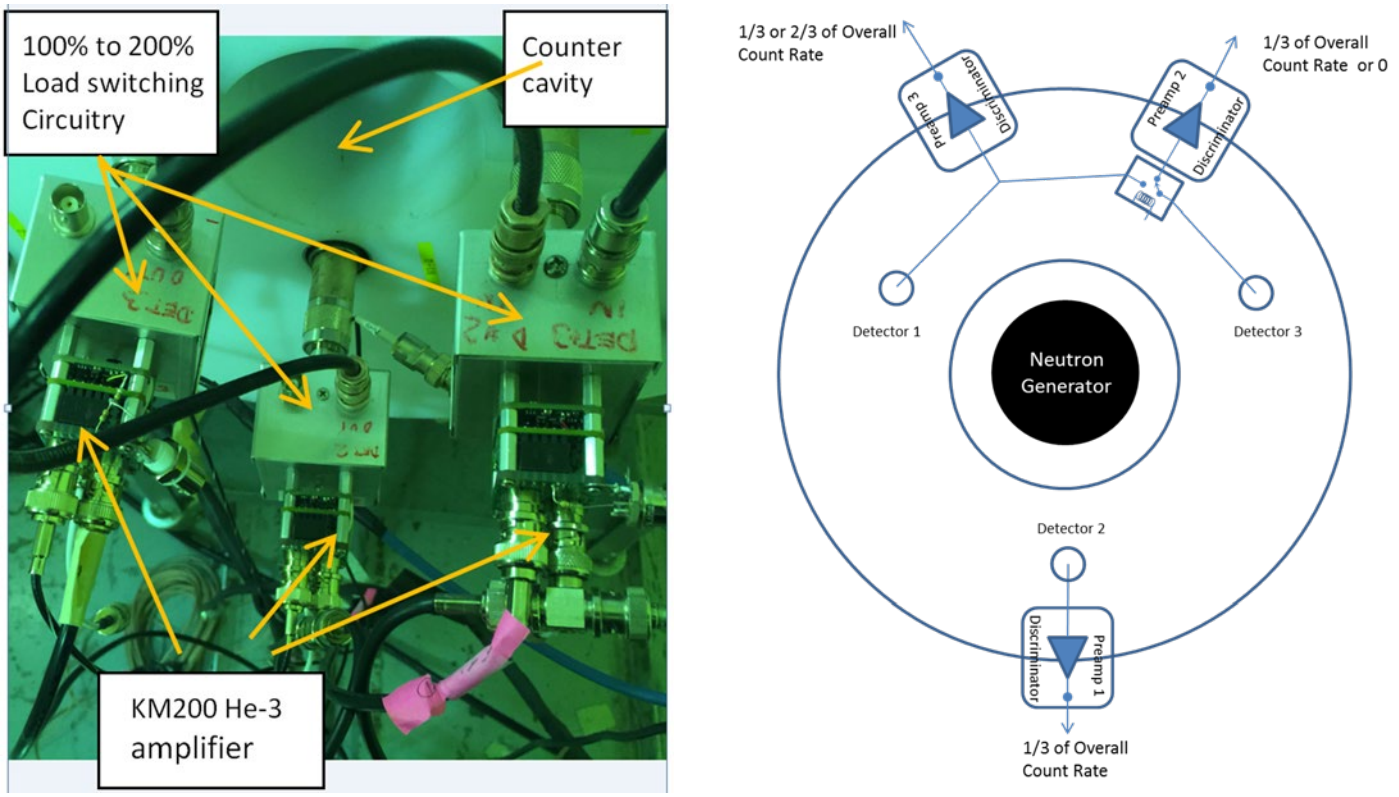

Fig. 4: Left: Top view of FNEM with preamplifiers and switching boxes installed on inner ring of tubes. Right: simplified switching diagram.

The count rates $N_{100\%}$ and $N_{200\%}$, corresponding to one and two tubes per amplifier, were measured for each intensity setting of the neutron generator. The load per amplifier and count rate data for each were recorded using a JSR-15 shift register. Using the analytical expressions derived in section two based on paralyzing dead time, we have calculated the incident neutron rate N_{IN} per amplifier. The measured count rates for PDT-110 (one tube per amplifier) and KM200 (one and two tubes per amplifier) are plotted in Fig 5.

The corrected output count rate Nout=Nin is used to calculate the dead time losses and corresponding dead time td based on the paralyzing DT model. In order to compare these results we also calculated and compared the KM200 and PDT-110A dead time using classical empirical and self-calibration methods for correction of counting losses. The plot on Fig.6 compares the calculated DT behaviour for:

- PDT-110A dead time from the paired source calibration in [10] calculated as 1.62 μs for 40 000 cps, and 1.54 μs for 83000 cps input count rate per tube;
- PDT-110A dead time using NG versus input count rate from self-calibration method ;
- KM200 dead time using NG and self-calibration method.

The results plotted in Figure 5 show significant dead time reduction (about 30%) between the calibrated and extended range of count rates as well as good consistency in PDT dead time behaviour using paired ^{252}Cf source and NG. The deduced dead time constant (t_d) shows a reduction in value for higher count rates. This is a clear indication that the real dead time losses do not follow the exponential dependency of the paralyzing DT model. The correction of counting losses using equations /6,7/ for non-paralyzing DT model provided even higher dead time constant dependence with positive slope. Therefore we used the correction data based on paralyzing DT that has lower dead time deviation at the maximal count rate range and thus fits better for that particular case.

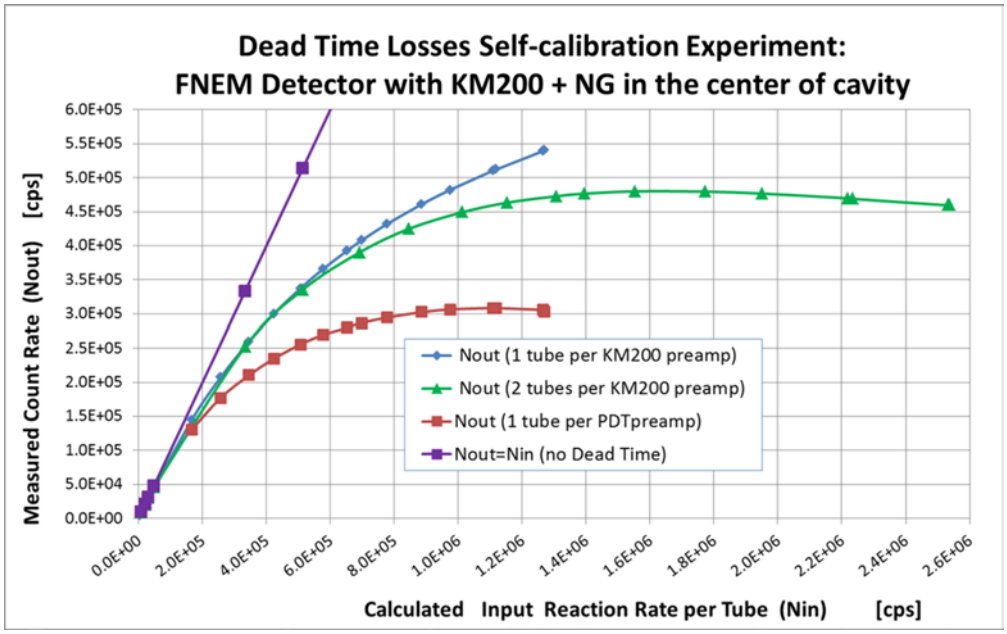

Figure 5: Measured count rates per amplifier versus (determined) input count rates for the KM200 at $N_{100\%}$ (blue) condition, KM200 at $N_{200\%}$ condition (green) and PDT110A amplifier (red) connected to one detector. The purple line represents the count rate (Nout=Nin).

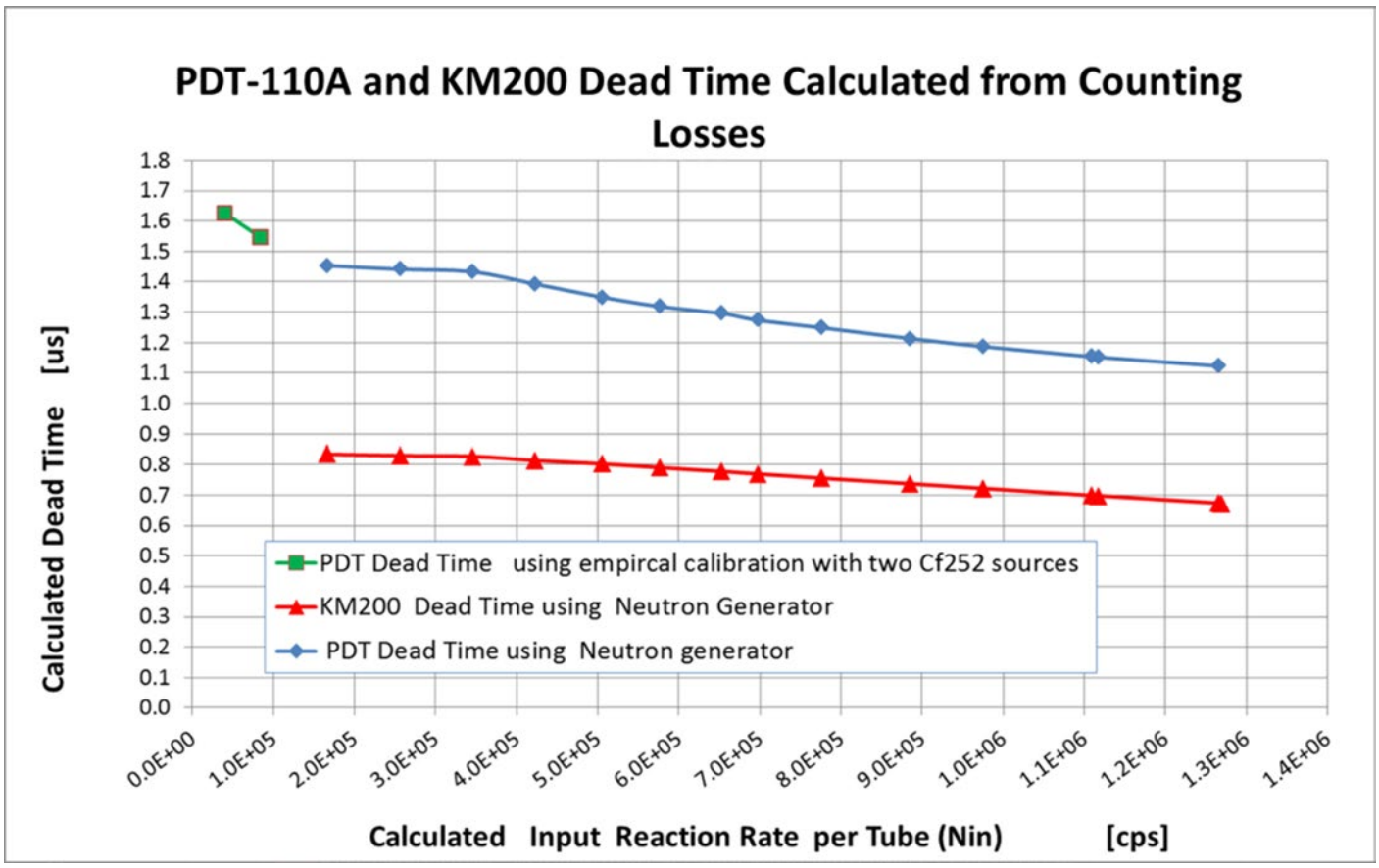

Figure 6: DT versus input count rate. Green: PDT-110A DT using a pair of ^{252}Cf sources [10]. Blue: PDT-110A DT using a NG and empirical method for correction of counting losses. Red: KM200 dead time using NG and self-calibration method for correction.

It should be noted that neither the non-paralyzing nor the paralyzing models are accurate over a wide dynamic range of incoming neutron count rate. Therefore, it is necessary to perform dead time calibration near the intensities of the target measured source. This is where the proposed calibration method is most valuable. It does not rely on the extrapolation of a priori calibration at lower intensity.

In order to explore and explain the count loss trend at higher count rates we ran the neutron generator in pulsed mode where the constant output emission rate is increased in reverse proportion to the generator duty cycle. The snapshots of the unipolar (current pulse) and bipolar (shaper output) signals from KM200 amplifiers, recorded at 10% duty cycle and maximum intensity of the neutron generator are shown on Fig. 7. The estimated incident rates for that setting is about 13×10^6 cps (10 times higher than maximum count rate from continuous output testing shown on fig.5.

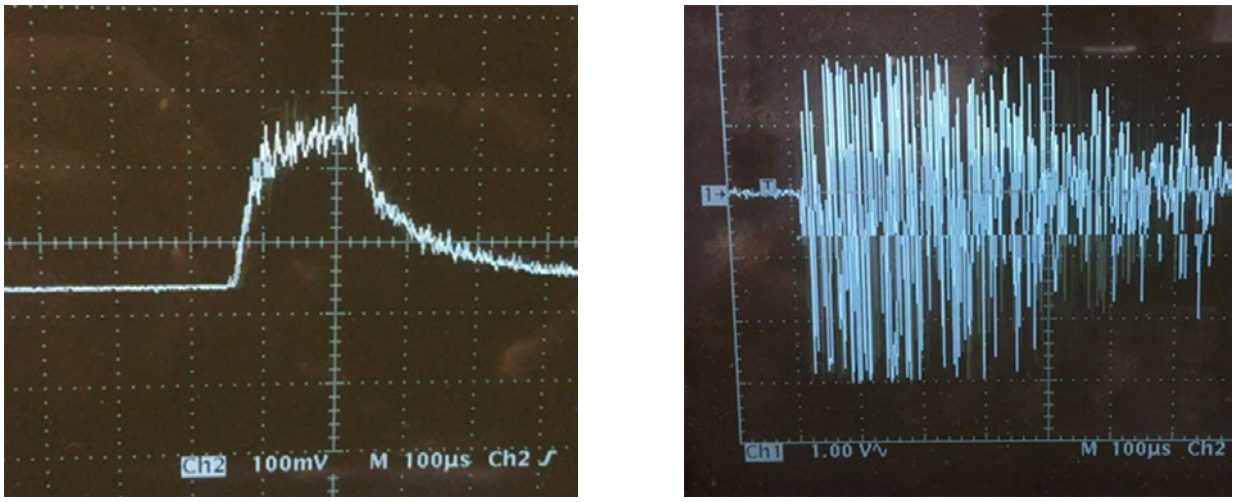

Fig. 7 Left: unipolar (current pulses) Right: The bipolar pulse output

The pile up of detector current pulses appears as a single fluctuating pulse that does not reach the base line during the entire duration of the neutron generator pulse, consistent with the updating paralyzing dead time model. In contrast, the bipolar pulses pile-up in both directions and thus cross the baseline despite the severe pile-up (20+ pulses during the duration of shaper pulse) and thus continue to count. Because of the random phase of the pile-up the superimposed signal looks much wider than singe bipolar pulses shown on Fig.1b.

6. Implementation aspects of this method in typical safeguards neutron systems

6.1 Active interrogation

Fission neutron detectors used in the pulsed active interrogation systems such as DDA assay for measuring of SNM have to operate at very wide dynamic range of incident count rates and thus are subject of severe counting losses. Implementation of faster tubes and electronics can improve the counting capabilities and allow analysis closer to the burst, but will not eliminate all of the counting losses. The implementation of this self-calibration method could further expand this capability by using simple switching circuitry without extensive retrofitting of existing electronics. The DT losses can be characterized by one time calibration that can give values that can be used for routine measurements. Because the DDA assay relies on singles rate measurements, DT losses are smaller and the accuracy of the calibration is not as critical as for assays based on neutron coincidence counting. Initial testing of this method in JRC PUNITA active interrogation system at JRC-Ispra will be reported in [11].

6.2 Neutron coincidence counting

Unlike singles rate measurements, neutron coincidence counting is very sensitive to the counting losses as the DT losses error of singles propagates with power 2, 3 etc., to the double, triples moments. The currently used DT loss calibration works well for low DT losses where the paralyzing DT model does not deviate much from the experimentally observed behaviour of the DT losses. But an applications such as coincidence assay for measuring high mass plutonium canisters, spent fuel, etc, that are expected to operate at higher DT losses the current practice for calibration with low activity ^{252}Cf sources may lead to substantial errors.

Here the measured count rates (S,D,T etc.) for the two hardware configurations (standard – i.e. 100% load and dead time – i.e. 200% load) can be used to extract and correct for dead time losses. Two possible methodologies are envisioned: a) extrapolate dead time free count rates from the slope of the measured count rates for 100% and 200% load; b) iterative procedure to extract and correct for dead time losses. The former approach relies on linearity of the count rate variation with preamplifier load, which will be explored and confirmed experimentally. For more complex situations, where nonlinearities in count rate variation with preamplifier load are observed, the iterative approach will be used. The iterative approach is foreseen to use the ratios (e.g. $\frac{S_{100\%}}{S_{200\%}}; \frac{D_{100\%}}{D_{200\%}} \frac{T_{100\%}}{T_{200\%}} \frac{Q_{100\%}}{Q_{200\%}}$) for singles, doubles, triples and quads, that, if properly dead time corrected, should not depend on the load per preamplifier. We will use this fact to develop the iterative calibration procedure, where the initial estimate of dead time correction will be used to extract initial dead time corrected count rate ratios for both preamplifier loads. The dead time correction estimate will then be further iterated until close agreement between the dead time corrected ratios for 100% load and 200% load measurements is achieved.

We would like to stress that the proposed method and hardware implementation is applicable for all currently used preamplifiers (such as Amptek A-111) electronics for both shift register and list mode data acquisition.

7. Conclusion

We have presented a new hardware based method for the determination of counter dead time. This method can use the counting rates from actual unknown samples in order to determine the dead time correction constants and thus avoid the problem of extrapolating dead time coefficients determined at low counting rates to high counting rates. The hardware is relatively easy to retrofit to many existing neutron detectors. We have demonstrated the method for singles counting and shown that the dead time behaviour of typical neutron detector systems does not follow either paralyzing or non-paralyzing model precisely, but the paralyzing model is closer. The method can also be used for doubles and triples and higher moments of multiplicity counters.

8. Acknowledgments

Office of International Nuclear Safeguards in the U.S. Department of Energy/National Nuclear Security for their support for presenting this work at ESARDA conference.

9. References

[1] G. F. Knoll. “Radiation Detection and Instrumentation” – 3rd ed., New York, NY: Wiely & Sons, 2010

[2] R. Jenkins, R. W. Gould, D. Gedcke. “Quantitative X-rays Spectroscopy”, New York, NY: Marcel Dekker, Inc., 1995

[3] K. Ianakiev, M. Iliev, M. Swinhoe and N. Johnson “High Count Rate Thermal Neutron Detectors “High

Count Rate Thermal Neutron Detectors “IAEA Safeguards Symposium, Vienna, 2014

[4] Iliev, Metodi; Ianakiev, Kiril Dimitrov, Swinhoe, Martyn Thomas “KM200 Front-End Electronics for Thermal Neutron Detectors”, INMM 57th Annual Meeting, 2016-07-24/2016-07-28 (Atlanta, Georgia, United States)

[5] N. Ensslin, W. C. Harker, M. S. Krick, D. G. Langner, M. M. Pickrell, J. E. Stewart, “Application Guide to Neutron Multiplicity Counting,” LANL, Los Alamos, NM, LA-13422-M, November 1998.

[6] H.O. Menlove, M.T. Swinhoe, J.B. Marlow, et al., “Mini-Epithermal Neutron Multiplicity Counter (Mini-ENMC) Manual,” Los Alamos National Laboratory Report, LA-14350-M (2007).

[7] L. Holzleitner, M.T. Swinhoe, “Dead-time correction for any multiplicity using list mode neutron multiplicity counters: A new approach – Low and medium countrates,” Radiation Measurements 46 (2011) 340-356.

[8] A. M. LaFleur, et al. “Characterization and performance evaluation of a new passive neutron albedo reactivity counter for safeguards measurements”, Radiation Measurements 61 (2014) 83-93.

[9] K. Ianakiev, M. Iliev, M. Swinhoe, HIGH COUNT RATE THERMAL NEUTRON DETECTORS AND ELECTRONICS; Provisional Patent Application Serial No. 62/411,898;

[10] Hee Seo, et al. “Development of prototype induced-fission-based Pu accountancy instrument for safeguards applications”, Applied Radiation and Isotopes Volume 115, September 2016, Pages 67–73

[11] K. D. Ianakiev[1], M. L. Iliev[1], M. T. Swinhoe[1], B. Pedersen[2], G. Varasano[2], J. Crochemore[2], T. Bugucarska[2], L. Holzlightner[2], P. De Baere[3], S. Vaccaro[3], M. Couland[4], « Field trial of KM200 Electronics in the JRC PUNITA Facility” , 39th ESARDA Conference, 15th-18th May 2017, Dusseldorf, Germany

Containment and Surveillance Systems – reflections on future technologies

G. Boström, V. Sequeira, E. Wolfart
European Commission, Joint Research Centre
Directorate for Nuclear Safety and Security, Ispra, Italy

Abstract:

Euratom Safeguards is busy implementing the Next Generation Surveillance System (NGSS) in the field currently, close to 700 units are to be installed in the next years.

This paper deals with the time after NGSS. It is time to design the technology that follows, to discuss the requirements for containment and surveillance systems in a broader sense, to study the very volatile general technical environment and select options for further development.

With the growth of the security markets, with the advent of autonomously driving cars, with increasing threats in cybersecurity, with the appearance of more intelligent, smart sensors using various physical technologies beyond optical vision, opportunities can be envisaged and analysed for applicability. This may allow more efficient and effective safeguards implementation, and ideally, could contribute to an opening of the market and help reducing cost.

At the same time, a growing number of facilities particularly at the back end of the fuel cycle turn static and new facility types appear. These pose their own challenges and may call for revised inspection approaches utilizing non image based sensors.

Keywords: publication; guidance; editing; standardisation

1. Introduction

Inspectorates are constantly being challenged with decreasing funding, amount of personnel, inspection days and mission budget. The efficiency and effectiveness of safeguards activities are debated. At the same time, new equipment must be developed to exchange old one's which has come close to the end of life cycle.

In order to fulfil the desired wish that inspectors are both more effective and efficient, we would need to see an increase in the number of sensors connected together with a clever automated decision-analysis and event-extraction. A current emerging system existing with a constantly increasing functionalities is "integrated Review and Analysis Program" (iRAP) which is a joint development project by IAEA and DG-ENER [1]. Adding the automated data transfer using techniques such as RADAR and Rainstorm is currently building a very cost-optimized solution.

Could we not in the (near) future have even more unattended equipment in place, which observes the processes transmitting relevant data to a local storage. Automated processes would identify events and assist the Nuclear Inspectors to confirm declared operations and to analyse potential situations where further analysis is needed. The unattended systems could be based on a combination of dedicated components and OEM modules.

The above scenario would require a larger amount of unattended sensors that has the capacity to transmit remotely its content to a central store. In Nuclear Safeguards of today we have an increasing amount of unattended systems, primarily Surveillance cameras and a few other connected devices for enrichment and reprocessing facilities [2].

This system, correctly configured and where relevant data is provided, is able to extract a list of relevant events and provide, if necessary and available a limited sized video-sequence over the time of the events. The strength of such a system setup is the efficiency with which the inspector would work, i.e. the time spent is focused on the events and not on all the time in between events.

With a constantly increasing threat from cyber-attacks, the new safeguards tools must be able to seamlessly follow the latest advancement in cybersecurity to ensure the authenticity of all safeguards relevant data and be able to handle future cyber-attacks.

2. New Safeguards tools

The valid lifetime for a safeguards equipment is very long. It is long not just because it is the perfect tool. The development-time and validation process is both long and expensive. Sometimes, the development of new equipment from idea to final fully functional system takes 5-10 years, sometimes even longer.

If the inspectors working with safeguards equipment would chose, quite some equipment would have been updated, changed or trashed. This cannot be done for the simple reasons that other comparable or better equipment neither exists nor can be developed in a reasonable amount of time.

Whenever new safeguards equipment is designed, the common sense would be to think about the long-term future trends. Not just the near future but also potentially considering relations to sensor-technologies from other industrial branches. By thinking out of the box, one could potentially gain strengthened detection capacities or effectiveness.

Where allowed by the operator and agreed with local state, the devices would without interaction from Inspectors or Technicians send its data to headquarters or local site-offices. The data can be processed automatically and large benefits can be identified both for Inspectors but also for Operators and State Inspectorates. With this in mind, the future safeguards tools must enable secure remote data transmission and centralized control.

3. Next generations Nuclear Safeguards camera (NGSS)

The NGSS is currently deployed in large scale substituting old DCM-14 cameras and other commercially available systems such as FAST/NICE. The camera, despite initial engineering difficulties, is a success. Currently, the output video stream files from the camera can be handled by both the Safeguards review station GARS, by iRAP but also by new emerging video-review tools such as Video-Zoom [3] or in its most basic form, any MPEG enabled video-application. The NGSS has important features such as multiple asymmetric crypto-keys for authentication, enabling dual-use and third party installation and maintenance.

The primary components, i.e. the imaging sensor and the processing DSP, acquire the images and implements scene-change detection. This detection capacity means that the camera can by itself react to scene changes and when these occur, tag the event and change the image storage frequency. The camera can also be triggered by external sources via a few electrical interfaces.

The subsequent video review tool, then can list all the events that have been detected both by the scene-change detection but also from other events that has been connected via electrical or network-based connections.

Still, the camera, having all the advanced capacities in some cases returns large amounts and long sequences of video data. Generally, it is a very time-consuming task for the inspectors to perform an efficient and effective analysis of long video-streams.

When considering a future generation of Surveillance Cameras, what kind of additional tools and sensors can be added? Remember that to go from an idea to final deployable product is very long, maybe now it is time to start thinking of a successor. Currently, the commercial market is designing new generations of advanced sensors that did not exist some years ago. To be more visionary, some sensors, which may be essential for safeguards in 10 years from now, has potentially not even been launched commercially?

We should probably consider the fact that commercially available or open modules may fit into new systems and form its central parts. Of course, the global aim of a robust system with long term guaranteed operational lifespan must be kept in mind. Still, new emerging tools, sensors and OEM platforms could be part of a new generation of safeguards tools.

Apart from the basic CMOS/CCD light sensitive sensor, what additional components could be of interest to design the future system? A list drawn today cannot be fully comprehensive, since future intelligent sensors are not known. Trying to answer the question, we can start with a few components that appear in existing Nuclear Safeguards equipment, which could also be of interest in a compound sensor-system.

3.1 LIDAR sensors

A Lidar is by the name; Light Detection and Ranging, is a sensor which uses electromagnetic waves in the near- or visible spectra to measure distances. These sensors have the capacity to measure the near surrounding in 3 dimensions. Already now, they have entered into the consumer market and the first smart-phones equipped with solid-state sensors with active light enabled 3D capacity are commercially available [4].

How would this help future surveillance systems? In the area of design information verification/Building Technical characterization (DIV/BTC) or containment verification, this technique is already a key-player. Several nuclear safeguards systems use these sensors to draw conclusions; Static 3D scanners used in 3DLVS/3DLR for accurate change detection [5] and a mobile scanning equipment for large scale mapping and indoor-localization[6].

But what can they do for a Surveillance system? As previously mentioned, video-review is a crucial but fairly time-consuming activity. Intrinsically, a large amount of image sequences may be visualized to identify declared activities. Furthermore, an inspector must maintain focus to potentially also find what not searched for, i.e. potential non-declared activates.

A Lidar amended Safeguards Surveillance Camera could be designed in such a way that a triggered event occurs whenever something in the scene physically happens. One could neglect changes in the image-scene such as shadows, light changes etc. and concentrate on actual movements.

Figure 1 shows an image and a schematic drawing of a spent fuel pond. The surveillance camera is placed to

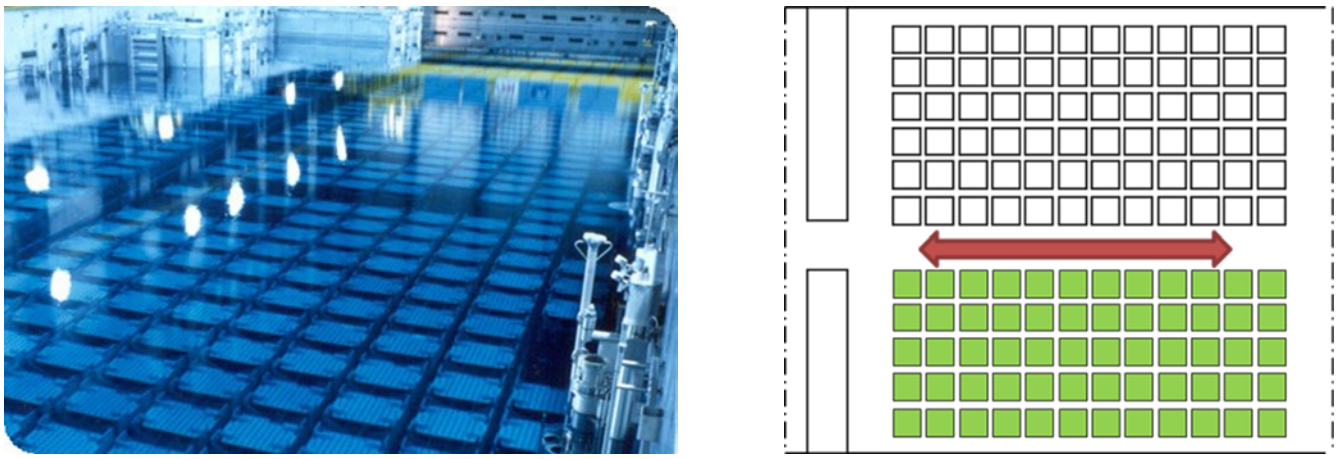

Figure 1: Left: Image of Interim storage pond in La Hague, France (image from Areva Webpage), Right: concept pond with green baskets under surveillance and red arrow indicating daily movement of equipment with traversal crane.

overlook the stored bins and no changes are to take place. The natural movement of traversal crane with a bin-carrier both introduce natural scene-changes in the observed scenario. The crane will also introduce small waves which makes the reflection of illumination to flicker in the water-surface. In such a situation, an image scene-change detection will have difficulties to perform well. By introducing a 2D or 3D based laser scanner we don't need to rely only on the image itself. The additional sensor will map in true dimensions a plane parallel to the water surface above the bins; and any interference with a device, rod or traversal crane can be detected and consequently an image sequence event can be stored.

There are several examples of where an added proximity sensor would assist and provide robustness, efficiency and effectiveness to a safeguards camera.

3.2 Radiation sensors

Both Neutron and gamma detectors are playing an important role for a safeguards camera to trigger when relevant scenarios occur. Most probably, future safeguards cameras would integrate such sensing capacities and, based on need, assist in the triggering of events.

3.3 Other sensors

Considering that we discuss future technologies, why not broaden the concept. Many commercial sensors; pressure gauges, noise sensors, scales, temperature and pyroelectric sensors and ID-readers could be of interest. And last but not least, the sensors which are not even commercially available yet.

4. Introducing the concept of a "Remote Safeguards Device"

When designing a new generation of surveillance cameras we should take the moment also to consider, as discussed above, the capacity to add extra sensors. The new design should be clever to handle future unknown sensors to some reasonable limit.

As the basic requirements reflect on any unattended safeguards equipment installed in a nuclear environment, some basic rules apply: a system must be able to withstand power-outages for days, store locally data and have tamper-proof enclosures. A new and future system also needs remote transmission and control. This to summarize, means that the main system must be designed with a certain number of basic capabilities.

Identifying what components that would be mandatory to implement these basic capabilities, we would have a basic box and any sensor connected could as well be 'extra sensors', even the imaging sensor.

The thing remaining without the extra sensors is a very competent base system, then "Remote Safeguards Device", which can be placed in nuclear installations which intrinsically carries all the necessary mandatory features.

4.1 Basic concept design

In figure 2, the blue box lists components and capabilities forming a fundamental Remote Safeguards device. As seen, the system module has all the capabilities to be installed in a nuclear site. All the components for command and control exists; a modular CPU for decision making and logics, exchangeable memory module, battery-back-up, remote communication for control and data-extraction which makes it a modular smart sensor. The basic system must be equipped with a state-of-the-art protection for cyber-attacks as well as configurable encryption logics for digital encryption and data-authentication. Other components needed for the execution, i.e. the 'extra sensors', are added as needed via a pre-defined electrical, logical and physical interface. This enables a concept where several sensors can interact within the same tamper-proof enclosure as a single smart sensor.

From a maintenance point of view, the system concept should allow an external actor to perform on-site activities. An installation of a pre-configured device and basic maintenance such as battery-change and memory-card substitution should be allowed by design. This would mean that safeguards organizations significantly could reduce mission costs and manpower. We could also identify a clear benefit for the operator, which would not need to plan, organize and host visits on the site.

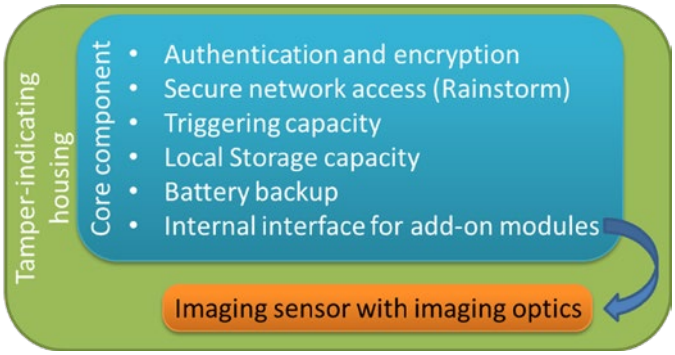

Figure 2: Schematic design of a new base unattended system with capacity to attach sensors using an internal interface

For sure, the imaging sensor will in most cases be used to enable an 'inspectors eye' in case of events. But the sensor base could also be used as a future remote data acquisition module in an extended RADAR architecture.

Ideally, the design of the system is based on existing subcomponents that are offered openly by the electronics industry or where intellectual property rights (IPR) can be guaranteed for Nuclear Safeguards. A realistic scenario would probably be to use a dedicated and optimized inner core-module together with added outer OEM or semi-commercial components. By using an existing open operating system and maintaining an open architecture, we would meet the Nuclear Safeguards community concerns and requests regarding IPR and cost-optimizations. This of course is easy said but would demand a high level of cooperation and openness between a few major players in the design and potential development phase. After all, this is a conceptual discussion where we do not need to address major hurdles but instead can focus on the functional aspects.

4.2 How concept fits into current and future remote data transmission paradigm

The ever-increasing need and request for remotely connected devices lead to the concept for unified approaches. Both remote transmission of data from device to headquarters or local servers can be implemented with this modular architecture. Streamlining the remote transfer enabling a Rainstorm [7] connection as a core component would immediately enable the strength of a compressed and adaptive network connection to a large amount of devices.

Once implementing the remote connection capacity with the core component, all systems will inherit the same communication interface and thereby unify both data-transfer and control logics.

Figure 3 shows the data-transfer scheme for a site that has several connected systems based on the concept device. As seen, different sensors can connect to remote transmission software with standardized means for data-transfer or connected to data-consolidators like RADAR. In cases where there is no remote-transmission available, data can be hand-carried using digital memories.

The same concept for unification goes for control and command. An established unified way to communicate state of health and to read/update configuration can be implemented for the common system cores which greatly simplifies control software.

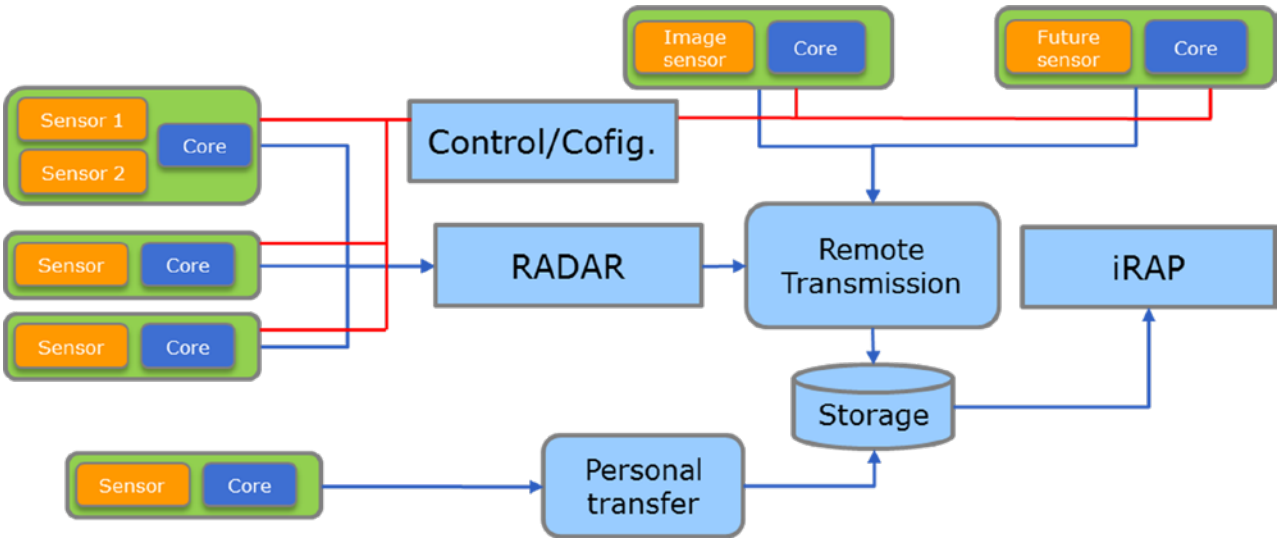

Figure 3: The concept safeguards platform in a future remote data transmission scenario. The blue arrows show the direction of data-transfer. The red lines indicate flow of command and control.

4.3 Concept usage

Future safeguards will require future technologies and new ideas. Currently, the safeguards community is facing new challenges such as an increase in dry storages and commissioned geological repositories are around the corner. New sensors and systems are entering the arena that needs to be managed regarding both installation and configuration but also related to remote data and status transmission.

This happens at the same time as efficient work-procedures are discussed. Remote sensing with less mission days as well as more effective inspections is requested.

The remote devices installed should generate a minimal footprint in volatile memory for normal situations, but when an event can be identified; higher framerates, more information and extended datasets can be accepted. The only issue is, who is deciding what is an event and when does it happen?

Sample case 1:
If we can detect an object physically entering an area of safeguards interest, we would robustly be able to consider this as a safeguards relevant event. For a Safeguards camera, adding a 2D/3D laser-based proximity sensor, we would achieve a more effective analysis following an efficient posterior review. Such system in the new concept would be based on a combination of an imaging sensor and a 2D/3D sensor.

Sample case 2:
In a transfer hall or loading cell, observation of loading events is requested. The presence of nuclear material would be detectable with either a small gamma or neutron detector. By coupling the presence of nuclear material to the imaging sensor, we would achieve a very competent surveillance system within a single tamper-proof case enabling effective and efficient posterior image review where events would reveal relevant movements.

Sample case 3:
Monitoring dry-storage casks in a storage is a fairly static operation. Very few or no movements occur over long periods. In this case, potentially no imaging capacity would be needed. Why would we need to generate video-files that show a static scenario? Instead, here a 2D laser would be able to monitor the casks and in case movements occur; an item tracking file could be extracted. An optional still image could also be acquired to document the event. Furthermore, adding also a radiation sensor could potentially add essential information to an event-data set.

Sample case 4:
Pressure, temperature, light, pyroelectric, weight, position, item counters, ID readers or other sensors already applied to a material-process by an operator could be used to confirm a normal operation. The sensor data could be bypassed in a base-system with copy functionality as described by Thomas et. Al [8], where the data transmission is read but not logically interfering with the data flow. The data copied would then be authenticated and transmitted accordingly.

Sample case 5:
Today we maybe won't care for sound, ambient temperature and light sensors or other currently not known sensors. In the future, there may be the need for a combination of such sensors. We cannot design and implement the future sensors but we can to as large degree as possible make space for them and allow a smooth integration into the future generations Remote Safeguards Device.

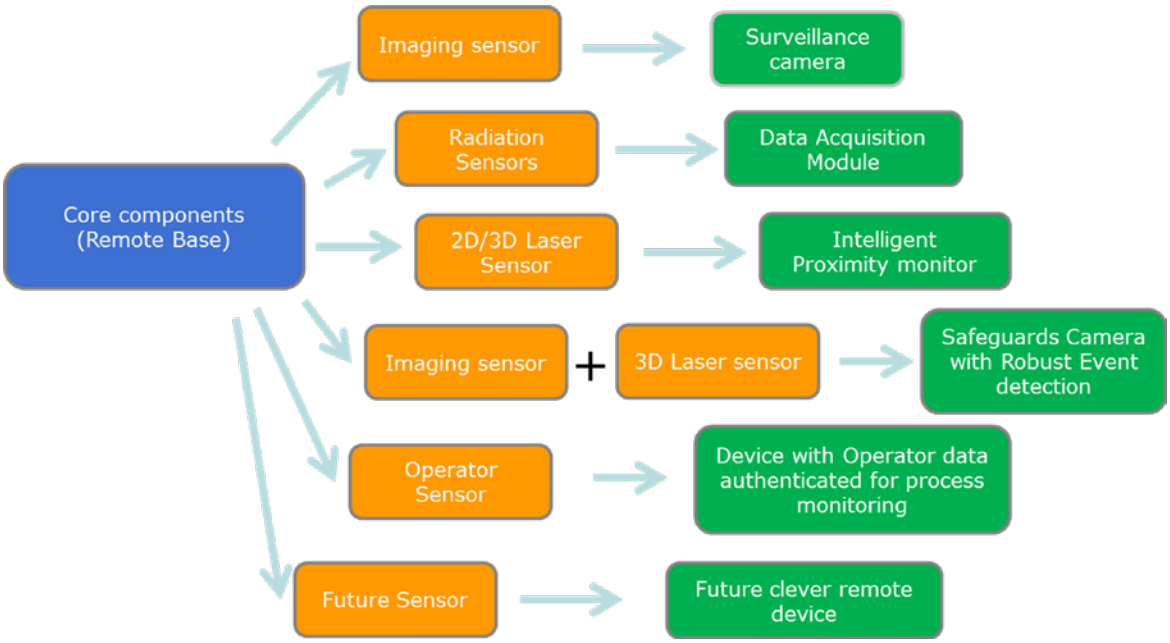

Figure 4: The base unattended system with a few conceptual sensors and there indicated use-cases.

Figure 4 describe in a single image a few realistic sensors and their indicative use which can be part of a future toolbox of devices ready to be deployed in the field when deemed necessary. The Orange boxes define a few sensor architectures which could be relevant. The green boxes briefly describe the potential use of such configurations.

5. Summary

The development of a new Safeguards instrument is a long process. There are currently a large number of different instruments in the portfolio. Not all, though, are optimized for the future. In this paper we have identified a few features that would be needed for a future device such as remote transmission, effective and clever decision making. By analyzing the prospect of a next generation of Surveillance camera, we introduce the concept of a Remote Safeguards Device which would be a modular device with the capacity to host different sensors in a tamper-proof case. Depending on the need, the basic sensor-platform and its connected sensors would enable a smart device which would be able to support the demanding requirement of an effective and efficient safeguards device. In order to sketch the requirement for a new safeguards camera a large amount of preparatory work is needed. This paper summarizes a rather visionary concept and certainly further analysis and discussions is needed.

6. Acknowledgements

The authors would like to thank J. Pekkarinen, K. Schoop and P. Schwalbach, EC Directorate Euratom Safeguards, for interesting discussion and comments within the topic of the article

7. References

[1] Smejkal A et. al., “Automated Processing of safeguards data: Perspective on software requirements for a future ‘All in One Review Platform’ based on iRAP”, Proceedings of 37th ESARDA Annual Meeting, Manchester, 2015

[2] Schoop K. at. al., “Progress and Status of Remote Data Transmission in EURATOM Safeguards”, Proceedings of 37th ESARDA Annual Meeting, Manchester, 2015

[3] Versino C. et. al., “Evaluation of a Surveillance Review Software based on Automatic Image Summaries”, Symposium on International Safeguards: Linking Strategy, Implementation and People vol. IAEA-CN-220 p. Page 224 - Paper IAEA CN220 #195, 2014

[4] http://www3.lenovo.com, Smartphone ‘Phab 2 Pro’

[5] Oddou J. et. al., “The Application of 3D Laser Scanning techniques for the efficient Safeguarding of fairly static storage facilinatural, depleted and reprocessed uranium“, INMM 51st annual meetings proceedings, July 2010

[6] Wolfart E. et. al. “Mobile 3D Laser scanning for Nuclear Safeguards”, ESSARDA Bulletin nr. 53, December 2015.

[7] Morgan K. et. al. , “Real-time And INtegrated STream-Oriented Remote Monitoring (RAINSTORM) Interface“, INMM Proceedings 2012.

[8] Thomas M. et. al., “Enhanced Data Authentication System: Converting Requirements to a Functional Prototype”, 35th ESARDA Symposium proceedings, 2013.

Status of safeguards R&D on pyroprocessing related facilities at KAERI

H-D. Kim, S-H. Park, S-K. Ahn, H. Seo, and B-H. Won

Korea Atomic Energy Research Institute, Daejeon
Daedeok-daero 989-111, Yuseong-gu, Daejeon, 305-353 Republic of Korea
E-mail: khd@kaeri.re.kr

Abstract:

The Republic of Korea (ROK) has implemented the Safeguards By Design (SBD) concept in nuclear fuel cycle facilities. Since the early 1990s KAERI (Korea Atomic Energy Research Institute) has developed several nuclear fuel cycle facilities for research activities on spent fuel treatment. Such facilities include the DUPIC Fuel Development Facility (DFDF), the Advanced spent fuel Conditioning Process Facility (ACPF), and the PyRoprocessing Integrated inactive DEmonstration facility (PRIDE). PRIDE is an engineering-scale R&D facility, handling non-irradiated depleted uranium and surrogates to develop and test key technologies for the pyroprocess. The data obtained from this facility will be used to evaluate the feasibility of a pyroprocessing facility in the future. DFDF consists of one concrete hot cell used for the technology development of the DUPIC (Direct Use of Pressurized Water Reactor Fuel in CANDU) fuel fabrication as well as for a voloxidation of irradiated PWR spent fuel rod cuts to produce a feed material for the electrolytic reduction process in ACPF. ACPF consists of two interconnected hot cells with two shielded rear doors for a material transfer designed for research on the electrolytic reduction of spent oxide fuel into a metallic form. Pyroprocessing related facilities that contain less than one significant quantity of nuclear material but that utilize technologies and equipment related to the electrochemical recycling of spent fuel have been treated as category III by the IAEA. The demand for robust safeguards applied to pyroprocessing facilities require the IAEA to develop new safeguards measures and techniques. KAERI's safeguards R&D will provide the IAEA and the international community with credible assurances regarding a state's fulfilment of its safeguards obligations.

Keywords: SBD; Safeguards Approach; Safeguards Measures; Nuclear Fuel Cycle; Pyroprocessing

1. Introduction

Since the early 1990s, KAERI has developed safeguards systems of several nuclear fuel cycle facilities for research activities on spent fuel treatment. Such facilities include the DUPIC Fuel Development Facility (DFDF), the Advanced spent fuel Conditioning Process Facility (ACPF), and the Pyroprocessing Integrated inactive DEmonstration facility (PRIDE). These facilities are now being used as facilities to develop and evaluate the pyroprocessing concept. Pyroprocessing related facilities that contain less than one significant quantity of nuclear material but that utilize technologies and equipment related to the electrochemical recycling of spent fuel have been treated as category III by the IAEA. The KAERI facilities are grouped into three categories based on the strategic value of the declared nuclear material and functional capability of the facility. The group of category I refers to self-contained capability facilities that have at least one significant quantity of suitable nuclear material and which could support undeclared plutonium production/separation activities without other supporting infrastructure. The group of category III refers to the pyroprocessing related facilities and category II is remaining facilities and LOF (Location Outside Facilities) at KAERI except category I and III facilities.

As part of a cooperative effort with the IAEA to find a safeguards approach for a pyroprocessing facility, the ROK designed a Reference Engineering-scale Pyroprocessing Facility (REPF) and developed a safeguards system for the REPF, which was reviewed by the IAEA. The IAEA plans to test the safeguards measures of REPF in KAERI pyroprocessing facilities through the member state support program (MSSP) with the ROK. The REPF is being upgraded to REPF+, which include the scale-up of the pyroprocessing facility and U/TRU fuel fabrication process. KAERI has developed a simulation program, Pyroprocessing Material flow and MUF Uncertainty Simulation (PYMUS) to assess the nuclear material accountancy system of the REPF. The PYMUS is under improvements to include the statistical analysis of Near Real Time Accountancy (NRTA).

KAERI is developing an advanced safeguards system, including nuclear material accounting technologies and a new safeguards approach for pyroprocessing facilities in parallel with the process technology development and facility design. This paper addresses the main features of the safeguards R&D status of the pyroprocessing facilities at KAERI.

2. Safeguards Systems of Nuclear Fuel Cycle Facilities at KAERI

According to the "Agreement for Cooperation between the Government of the Republic of Korea and the Government of the United States of America Concerning Peaceful Uses of Nuclear Energy" revised in 2015, KAERI has been using DFDF for preparing feed materials (porous pellets or fragments) from the spent PWR fuel generated in domestic nuclear power plants for the ACPF electrolytic reduction process. The ACPF at KAERI has been refurbished for the demonstration of pyroprocessing technologies related to the electrolytic oxide reduction process of PWR spent fuels.

Safeguards approaches for the DFDF and ACPF have been developed, which include neutron counters and containment and surveillance equipment with a process and radiation monitoring system.

The ACPF can provide a valuable opportunity to test various types of safeguards equipment for nuclear material accountancy, containment and surveillance, as well as process monitoring. At the moment, there are two types of safeguards equipment at the ACPF, i.e., ASNC (ACP Safeguards Neutron Counter) and ALIM (ACP LIBS (Laser Induced Breakdown Spectroscopy) Monitoring system).

The ASNC, based on a passive neutron coincidence measurement technique, measures the amount of ^{244}Cm [1–3]. The amount of nuclear materials in the ACPF can be determined using the Cm balance technique [4], which multiplies the measured ^{244}Cm amount by the Pu/^{244}Cm or ^{235}U/^{244}Cm ratio to calculate the amount of nuclear material of interest (Pu or ^{235}U). This kind of Cm ratio can be obtained through a destructive analysis (DA), gamma-ray spectroscopy, or burnup-code calculation. Note that the representativeness of the sample used for determining the ratios could be one of the major factors affecting the measurement uncertainty. In order to take the representative sample, several samples could be taken after the mixing process, which is a process in the head-end part to fabricate the input material for oxide reduction process, i.e., porous pellet. Additionally, the representative sampling technique using a spinning riffler has been studied for one of the possible candidates to take the representative sample without applying the mixing process.

In a previous study [5], the ASNC was installed in a hot cell of the ACPF and tested successfully with spent fuel rod cuts. However, its inner structure, with a horizontally-laid geometry, becomes deformed over the course of many years owing to the weight and ductility of the leaden gamma-ray shield. To address this problem, the ASNC was to be redesigned for a vertical-standing geometry based on the MCNP simulation and irradiation test results. Figure 1 shows the schematic and photograph of the redesigned ASNC, which has the improved remote-handling capability compared with the former ASNC. A total of 24 neutron detectors with the ^{3}He proportional counter (^{3}He-filling pressure of 4 atm, active volume of 1 in (D) x 20 in (H), and quenching gas of N_2) and the PDT 110A preamplifier were used. The cavity size for sample placement is 13.4 cm (D) × 26.0 cm (H). More detailed information can be found in [6].

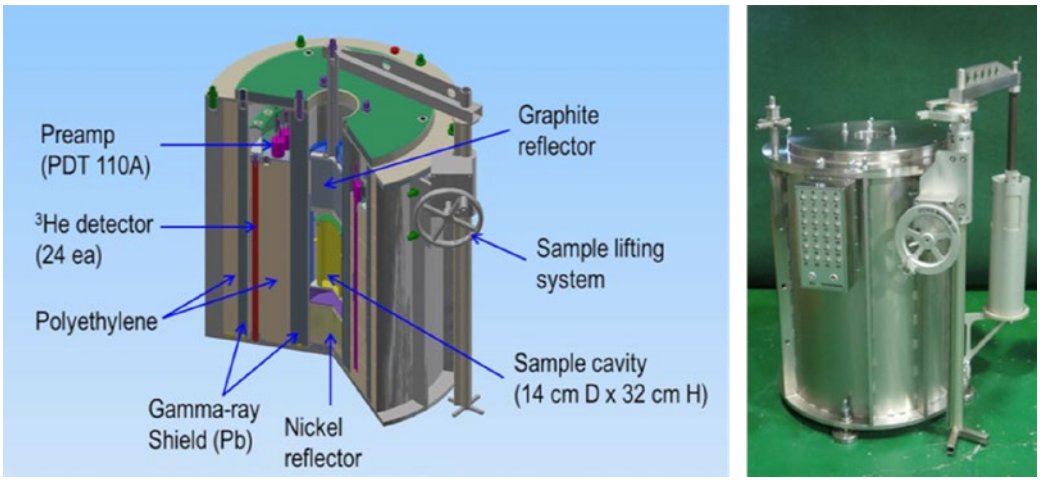

Fig. 1. Modified ACP Safeguards Neutron Counter

The detection efficiency profile of the ASNC in the axial and radial directions was measured for a ^{252}Cf standard source in order to characterize the system and verify the MCNP model. Ideally, a good system shows the same efficiency regardless of the source locations, resulting in a low measurement error. The measurements were performed over 10 cycles × 10 s/cycle for the ^{252}Cf source (intensity: ~1.92×10^{5} n/s) at different locations from -10 to 10 cm in the axial direction and from 0 to 4.5 cm in the radial direction. The measured detection efficiency was determined to be 24.4±0.07% and 24.3±0.05% in the axial and radial direction, respectively. The measurement precision errors were smaller than the plot symbols. The system showed a flat response in terms of the measured efficiency, as shown in Fig. 2. The use of LIBS based on fibre optics is a beneficial applications to remote sensing analysis, and it

has possibility of application to a hot cell environment by delivering laser energy to the target and by collecting the plasma light. The Fiber-Optic LIBS (FO-LIBS) system used to measure the Pu/U ratio of the process material of ACPF was installed in an air cell of ACPF, and the performance will be tested as the spent fuels are introduced to ACPF.

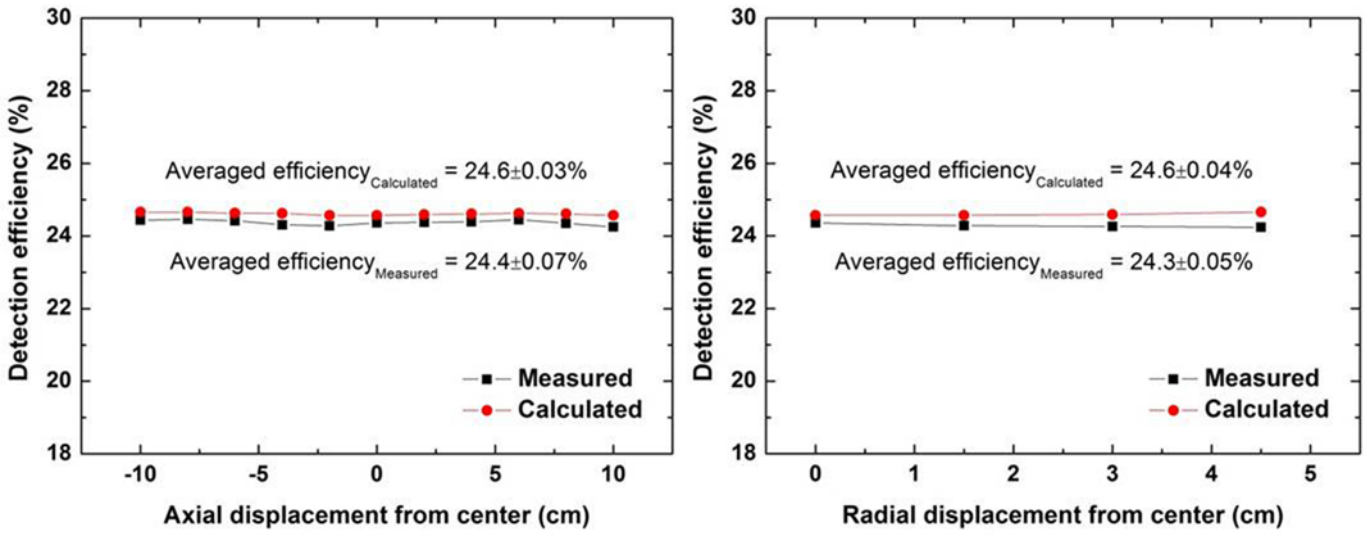

Fig. 2. Detection Efficiency Profile of the ASNC

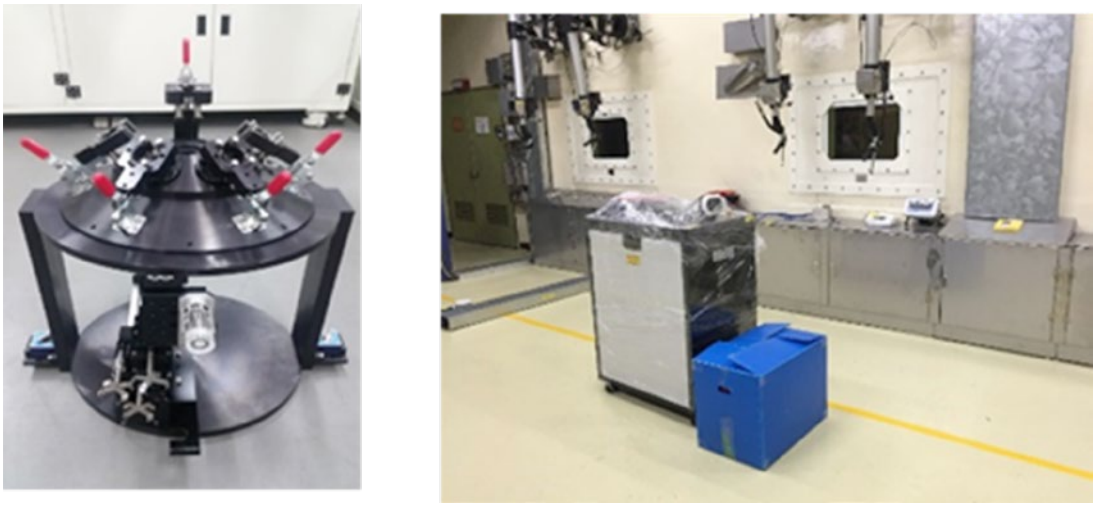

Fig. 3. LIBS installed at ACPF

PRIDE is an engineering-scale R&D facility, handling non-irradiated depleted uranium (DU) and surrogates to develop and test key technologies for pyroprocessing prior to the development and construction of an engineering-scale facility. The demand for robust safeguards applied to pyroprocessing facilities requires the IAEA to develop new measures and techniques to complement the more traditional safeguards systems. The bus bar system, together with portal radiation monitors, were selected and installed in the PRIDE facility to support the IAEA safeguards implementation (PIV, RII etc.) in this facility [9].

Process monitoring data such as the voltage, current, temperature, and humidity are collected from the process equipment. Most of the parameters relevant to the PRIDE safeguards are collected, and are displayed and provided to the IAEA. The PRIDE facility will be used for testing a way to develop the safeguards signature of the process monitoring data, containment and surveillance (C&S) device, and the training of IAEA inspectors on the engineering-scale pyroprocessing facility.

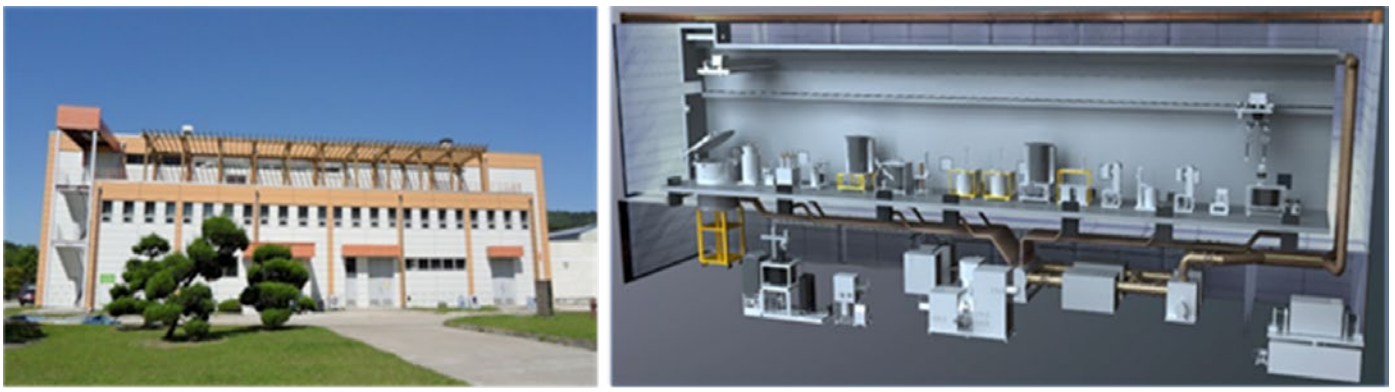

Fig. 4. Front view and working area of the PRIDE facility

3. Safeguards System of Reference Engineering-scale Pyroprocessing Facility

The ROK was working closely with the IAEA under the ROK's MSSP to develop a model SG approach for a REPF. The REPF design is part of the IAEA's effort to develop an effective safeguards approach for pyroprocessing facilities. As a result of the project, a model Design Information Questionnaire (DIQ), a model Facility Attachment (FA) and a model SG approach were prepared [10].

The concept of the REPF is now being revised to 30 MTHM throughput the facility, REPF+, to investigate the scale-up effect of the safeguards. One of key features of REFP+ is the allowance of nuclear material mixing between campaigns, whereas the material mixing was limited in the REPF. A simulation program, PYMUS, has been developed to analyse the nuclear material flow and calculate the MUF uncertainty [11]. The PYMUS is being upgraded to evaluate the detection probability based on a statistical test for the various diversion scenarios. Based on the experience with the ROK MSSP, the IAEA is well on its way to establishing effective safeguards for future engineering/commercial scale pyroprocessing facilities.

4. Conclusions

KAERI has developed several nuclear fuel cycle facilities (DFDF, ACPF and PRIDE) for research activities on spent fuel treatment. The ROK designed the REPF through IAEA MSSP and developed a safeguards system for the REPF, which was reviewed by the IAEA. KAERI is developing an advanced safeguards system, including nuclear material accounting technologies and a new safeguards approach for pyroprocessing facilities in parallel with the process technology development and facility design.

The application of Safeguards by Design (SBD) to these efforts will contribute to improving the non-proliferation and safeguards technology such that pyroprocessing technology can be realized in the future. It is expected that the deployment of these safeguards technologies will be useful for the advanced nuclear fuel cycle.

5. Acknowledgments

This work was partly supported by the National Research Foundation (NRF) grant funded by the Ministry of Science, ICT & Future Planning, Republic of Korea (No. 2017M2A8A5015084).

6. References

[1] T.H. Lee, H.D. Kim, K.J. Jung, S.W. Park, "Development of a Neutron Coincidence Counter for the Advanced Spent Fuel Conditioning Process," J. Korean Phys. Soc. 48, 218–221 (2006).

[2] T.H. Lee, H.D. Kim, J.S. Yoon, S.Y. Lee, M. Swinhoe, H.O. Menlove, "Preliminary calibration of the ACP safeguards neutron counter," Nucl. Instrum. Meth. A 580, 1423–1427 (2007).

[3] T.H. Lee, H.O. Menlove, S.Y. Lee, H.D. Kim, "Development of the ACP safeguards neutron counter for PWR spent fuel rods," Nucl. Instrum. Meth. A 589, 57–65 (2008).

[4] P.M. Rinard, H.O. Menlove, "Application of Curium Measurements for Safeguarding at Reprocessing Plants," Los Alamos National Laboratory Report LA-13134-MS, Los Alamos, USA, 1996.

[5] T.H. Lee et al., "Hot-test Results of the Advanced Spent Fuel Conditioning Process Safeguards Neutron Counter for PWR Spent Fuel Rods," Nucl. Technol. 176, 147-154 (2011)

[6] H. Seo et al., "Monte Carlo Simulations of Safeguards Neutron Counter for Oxide Reduction Process Feed Material," J. Korean Phys. Soc. 69(7), 1175-1181 (2016)

[7] D.W. Hahn, and N. Omenetto, "Laser-Induced Breakdown Spectroscopy (LIBS), Part I: Review of Basic Diagnostics and Plasma-Particle Interactions: Still-Challenging Issues within the Analytical Plasma Community", Appl. Spectrosc., 64(12), 335A (2010)

[8] M. Singh, A. Sarkar, J. Banerjee, and R.K. Bhagat, "Analysis of Simulated Burnup Nuclear Fuel by Laser Induced Breakdown Spectroscopy", Spectrochim. Acta B, 132, 1 (2017)

[9] W. Bekiert et al., "Safeguarding Pyro. Related Facilities in the ROK', Proceedings of IAEA Safeguards Symposium (2014)

[10] H.D. Kim, H.S. Lee, D.Y. Song, T.H. Lee, B.Y. Han, S.K. Ahn, and S.H. Park, "Application of safeguards-by-design for the pyroprocessing facilities in the ROK', JNMM, Vol. XL(4), 24 (2012)

[11] H.S. Shin, B.Y. Han, S.K. Ahn, J.S. Seo, and H.D. Kim, "Development of a Simulation Program for the Pyroprocessing Material Flow and MUF Uncertainty", Proc. of INMM 52th, California, USA (2011)

Feasibility study of advanced technology for monitoring plutonium in solutions with FP - Overview of Research Plan and Modelling for Simulation

M. Sekine(1), T. Matsuki(1), S. Suzuki(1), M. Tanigawa(1), T. Yasuda(1), A. Yamanaka(1), K. Tsutagi(1), H. Nakamura(1), H. Tomikawa(1), A.M. LaFleur (2), M.C. Browne (2)

(1) Japan Atomic Energy Agency (JAEA)
(2) Los Alamos National Laboratory (LANL)

Abstract:

The IAEA has proposed in its long-term R&D plan, the development of technology to enable real-time flow measurement of nuclear material as a part of an advanced approach to effective and efficient safeguards for reprocessing facilities. To address this, JAEA has previously designed and developed a neutron coincidence based non-destructive assay system to monitor Pu directly in solutions which contain little fission products after a purification process. A new detector to enable monitoring of Pu in solutions with numerous FPs is being developed as a joint research program with U.S. DOE at the High Active Liquid Waste (HALW) Storage Facility in Tokai Reprocessing Plant.

As the first step, the design information of HALW tank was investigated and samples of HALW was taken and analyzed for Pu concentration and isotope composition, density, content of dominant nuclides emitting gamma ray or neutron, etc. in order to develop a model of the HALW tank for calculation with the Monte Carlo N-Particle Transport Code (MCNP). In addition, gamma ray source spectra were given by Particle and Heavy Ion Transport code System (PHITS) calculation using extracting peaks from the analysis data with germanium detector. These outputs are used for the fundamental data in the MCNP model which is then used to evaluate the type of detector, shielding design and measurement positions. In order to evaluate available radiations to measure outside the cell wall, gamma ray and neutron measurement were carried out and the results were compared to the simulation results. The measurement results showed that there are no FP peaks above 3 MeV.

This paper presents an overview of the research plan, characteristics of HALW, development of source term for MCNP, simulation of radiation dose from the HALW tank and radiation measurement results at outside of cell wall.

Keywords: Pu monitoring, High level liquid waste, Reprocessing facility, Non-distractive analysis

1. Introduction

The IAEA has proposed in its long-term research and development (R&D) plan[1], development of improved tools and techniques to enable real-time flow measurements technology of nuclear material including Pu as an advanced approach to conduct reprocessing safeguards effectively and efficiently. The solution monitoring and measurement system (SMMS), which has been installed for continuous monitoring for reprocessing safeguards, can only monitor density, temperature and level of solution. Thus, direct Pu monitoring in the solution by SMMS is impossible. At JAEA, we have already designed and developed a neutron coincidence based non-destructive assay (NDA) system[2] to directly monitor pure Pu solution after extraction and purification. It has been confirmed that a total measurement uncertainty of less than 6% could be achieved, which could be applied as a partial defect verification. However, In the reprocessing plant, Pu including FP is being stored as inventory or retained waste. The Pu including FP has an extremely high radiation dose rate making it difficult to access and it's a challenge to develop a technology for monitoring of Pu with FP. Establishment of monitoring technology is important in order to increase transparency of material control and accountability (MC&A). Thus, JAEA has initiated development of a new technique to monitor Pu with FP, through a joint research program under the United States Department of Energy (US DOE) and the Ministry of Education, Culture, Sports, Science and Technology (MEXT) of the Japanese government.

2. OVERVIEW

2.1 Plan[7]

Although the most suitable test area is the input accountability tank or first extraction process, the JAEA's Tokai Reprocessing Plant (TRP) is no longer operating. Since HALW solutions contain both Pu and FP, the HALW tank (Fig. 1) was selected as the place where the technology will be developed and tested under this R&D program. The HALW tank is shielded by a concrete cell and it is possible to place detectors at the inside/outside of the concrete cell. Figure 1 shows the image of the Pu monitoring technology development. The purpose of the R&D is the development of a detector that can monitor Pu solutions containing FP.

The development is carried out under cooperation with U.S. national laboratories: Los Alamos National Laboratory (LANL) and Lawrence Livermore National

Laboratory (LLNL). At first, the radiation (type and intensity) from the HALW is characterized and measurement technology is selected. Then, appropriate detector is designed and developed. The optimized detectors are tested and evaluated at the HALW tank with changing liquid level as shown in Fig. 1. This technology has the potential to be applied to real time monitoring for the entire reprocessing plant.

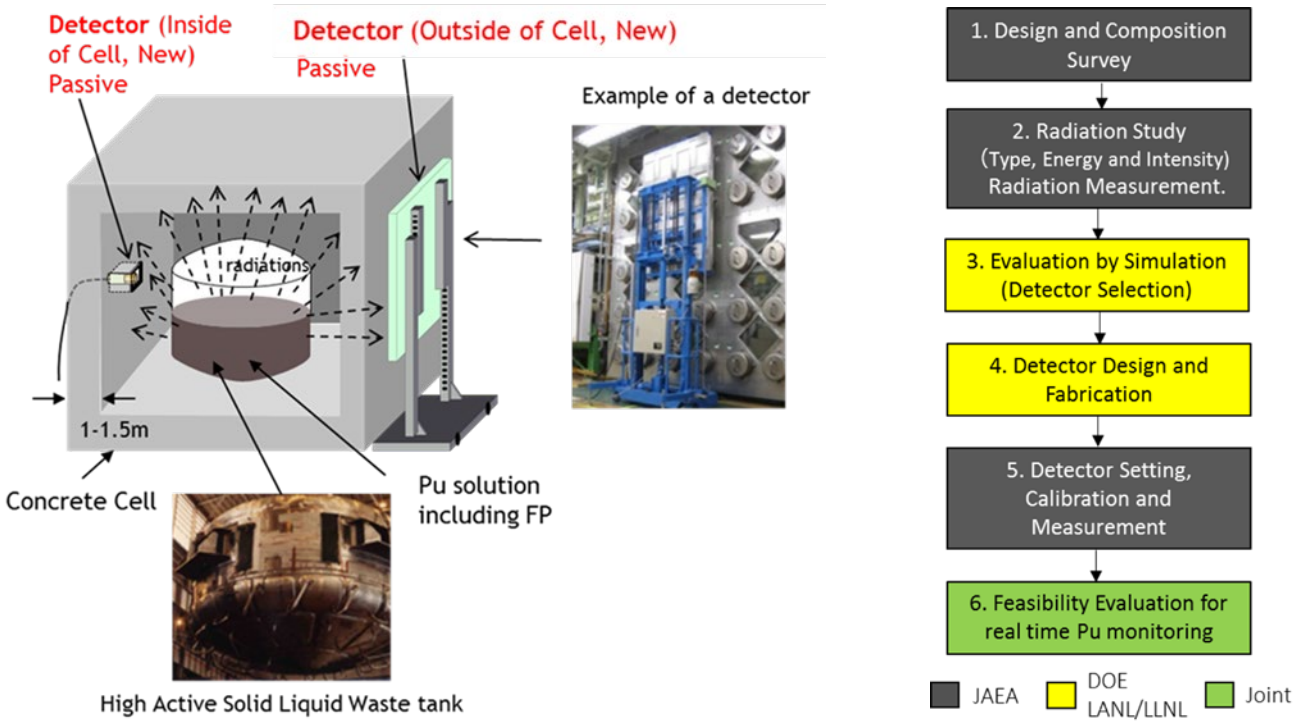

Figure 1: Image of Pu direct monitoring technology development

The study of development of a new technique to monitor Pu with FP is being carried out from 2015 to 2017. The timetable for the project is shown in Table 1.

2015	**1. Design information and composition survey of HALW(JAEA)** The design information for HALW tanks and concrete cells was reviewed to develop a simulation model. Radiation (type and intensity) using alpha spectra and gamma spectra, and composition using mass analysis were investigated to develop an input file for simulation. Using HALW analysis data of gamma spectra and neutrons, the radiation dose rate in HALW tank was estimated for the input file for simulation. **2. Radiation study (JAEA)** Gamma rays and neutrons were continuously measured outside of the concrete cell, where the HALW is located, to study placement of the detector and radiation characteristics. The detectors used were high purity germanium (HPGe) detector for gamma rays and six He-3 tubes for neutrons [3].
2016	**2. Radiation study (JAEA/LANL)** Gamma rays were continuously measured inside of the concrete cell, where the HALW is located, to study placement of the detector and radiation characteristics. **3. Evaluation by simulation (LANL/LLNL)** LLNL made a common model and simulate gamma rays to benchmark ion chamber measurements help JAEA with gamma detector design. LANL will use this common model to simulate the neutron flux from the HALW tank to support the neutron detector design development.

2017	**2. Radiation study (JAEA/LANL)** Neutrons will be continuously measured inside of the concrete cell, where the HALW is located, to study placement of the detector and radiation characteristics. **4. Detector design and fabrication(JAEA/LANL/LLNL)** Based on the analysis data, simulation analysis results, and preliminary measurement results at the inside and outside of the concrete cell, candidate technologies and Pu monitoring algorism will be considered. The test detector will also be optimized and designed. **5. Detector setting, calibration and measurement(JAEA/LANL/LLNL)** Detector test with changing high level liquid waste amount. **6. Feasibility evaluation for real time Pu monitoring(JAEA/LANL/LLNL)** The test detector will be demonstrated at HALW tank to validate its measurement capabilities.

Table 1: Timetable for establishment of Pu monitoring system (Japanese fiscal year)

In the implementation of this technology development, JAEA has received the support of LANL/LLNL based on the implementing arrangement between MEXT and DOE concerning cooperation in the field of nuclear energy-related research and development.

3. The results of composition research of HALW

3.1 Analytical tools for HALW solution

Composition research of HALW for our target HALW storage tank (V35) which has the highest concentration of Pu in HALW tanks at TRP was conducted in order to develop a model of the HALW tank for calculation with the MCNP. Especially, gamma-ray spectrum was measured in high energy range (up to 10 MeV) to understand what kind of gamma rays can be detected at the wide range. Figure 2 shows experimental setup of gamma-ray spectrometry. HPGe [COAXIAL TYPE Ge Detector (GC2020), CANBERRA] and multi-channel pulse height analyzer (MCA) [DSA1000, CANBERRA] connected to HPGe was used for gamma-ray spectrometry. Its relative efficiency was 20% at Co-60 1332 keV and crystal size is ϕ 61.9 mm, L 30.8 mm. Figure 3 and 4 show photos of HALW sample bottle and picture of experimental setting for gamma-ray measurement. HPGe detector and HALW sample is surrounded by Pb introducing to attenuate background. In order to reduce dose rate, sampled 1 ml HALW solution was diluted with nitric acid of same acid concentration to 10000 because too high dose rate cause high dead time. Other analyzed items and methodologies are shown in Table.2.

Figure 2: Experimental setup

Figure 3: Measurement chamber and sampling bottle

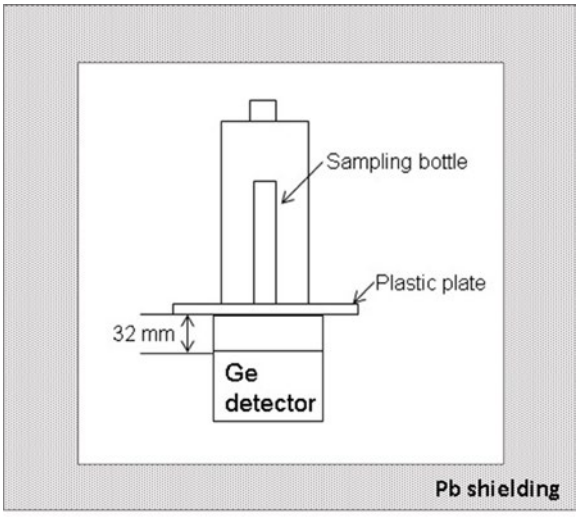

Figure 4: Image of inside of the measurement chamber

Analytical item	Unit	Methodology
Acid conc.	mol/L	Neutralization Titration with NaOH (*Hiranuma COM-1600*)
Density	g/cm^3	Density meter (*Anton-paar DMA-35*) oscillating U-tube type
Cm conc.	Bq/mL	*SEIKO EG&G* using detector *"alpha duo"*
Pu conc.	mg/L	Spectrophotometry using cerium nitrate with sludge dissolution by HF
U conc.	g/L	Spectrophotometry(*Shimazu UV-2450*) using TOPO - Ethyl acetate -Dibenzoylmethane (DBM)
Gamma measurement	Bq/mL	Canberra using detector *GC-2020*
Pu isotopic composition	wt%	Mass spectrometer(*Thermo TRITON*) with sludge dissolution by HF, TEVA resin for Pu separation
U isotopic composition	wt%	Mass spectrometer(*Thermo TRITON*) with sludge dissolution by HF, U-TEVA resin for U separation

Table 2: Analysed items and methodologies

3.2 Results of gamma-ray and neutron of HALW solution [5]

The gamma-ray spectrum from HALW solution was measured and shown in Fig.5. It is used for source file of MCNP simulation.. We estimated neutron yield in V35 with calculation based on alpha spectra and show it in Table 3. A diluted sample was dropped on the centre of a sample dish (1ml) and dried gradually as not to bump. Furthermore it was heated (it became red state) with a high frequency heater. After the cooling, Cm-243 + Cm-244 peaks and Cm-242 were measured by the α spectrum analyser and Cm amount was calculated as the sum of them. To assure the quantity, two measurement sample was prepared from same liquid. If the difference of measurement result was less than 20 %, we used the value. The rate of (α, n) reactions was calculated multiples of the analytical value, calibration constant, branching ratio, half time, spontaneous fission yield and divided by their density. The neutron yield can then be used in the input file for simulations.

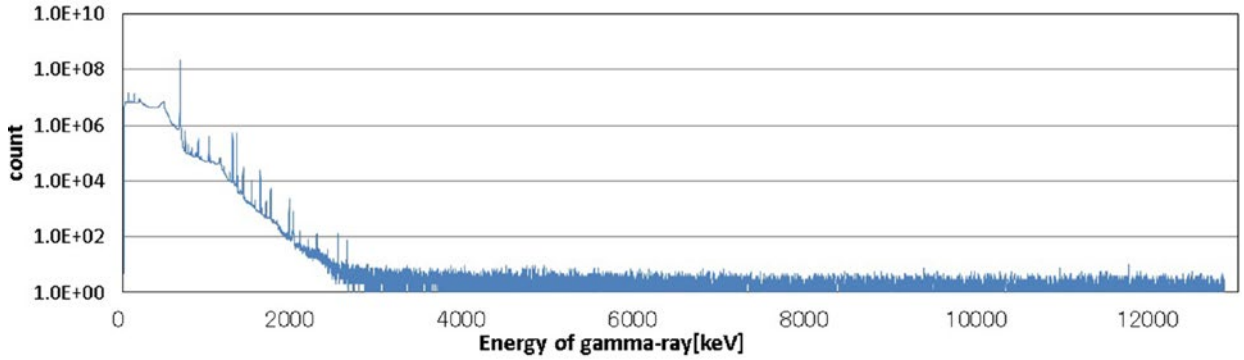

Figure 5: measured gamma-ray spectrum (Measurement time: 550000 [sec])

Nuclide	Neutron yield [n/sec]
^{244}Cm	1.09×10^{9}
^{240}Pu	8.24×10^{6}
^{242}Pu	2.10×10^{6}
^{238}Pu	8.47×10^{5}
^{241}Am	1.22×10^{4}

Table 3: Neutron generation yield in V35

4. Development of irradiation source input file in HALW tank

4.1 Gross count of each peaks

It was necessary to estimate the absolute gamma-ray counts emitted from HALW sample for the gamma-ray source data in the MCNP simulations. Key points for making source data were (1) Evaluation for gamma-ray energy emitted from HALW sample, (2) Peak count quantity, (3) Estimation for emitted gamma-ray quantity. After, we conducted more precise energy calibration for the gamma-ray spectrum and made peak count estimation. Then we calculated the absolute detection efficiency in the analysis geometry. As shown in Fig.6 each peak spectrum was cut with straight line in red. The gross counts from each peak was estimated with this original spectrum as shown in Fig.7.

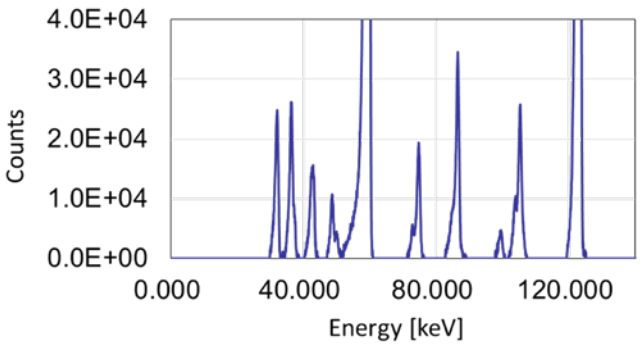

Figure 6: cutting spectrum with straight line (gross)

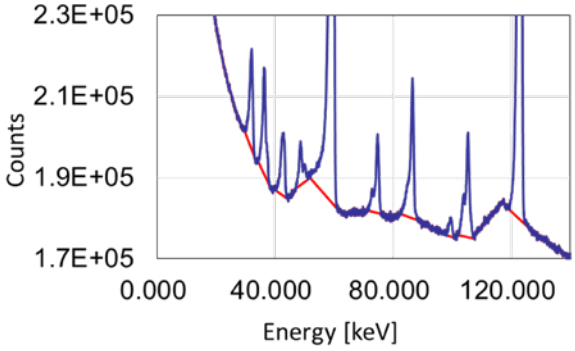

Figure 7: Net count of each peak

4.2 Calculation of absolute detection efficiency by PHITS model

In order to confirm how well the HPGe detector could detect gamma rays at the inside of the measurement chamber, a model of the measurement chamber was developed as shown in Fig.8. Because the absolute detection efficiency of each peaks was different by each gamma-ray energy, we calculated absolute detection efficiency of each gamma-ray in analysis geometry by PHITS code as shown Fig.9[9]. Cut off energy was set as 1 keV.The absolute detection efficiency multiplied to net counts (Fig.7), then gamma ray amounts at V35 tank by the each energy were calculated as shown in Table 4. The Bq values were converted to Ci to compare ORIGEN results. The ORIGEN calculation was reflected the reprocessed spent fuels of ATR(Fugen), BWR(s), PWR(s) and JPDR(s) from 1977 to 2006. The inventory of nuclear fuel calculated by the ORIGEN was multiplied the transfer ratio to each tanks obtained from liquid transfer history.The evaluated absolute gamma-ray intensities were on the same order as ORIGEN and the analysis value with gamma spectra as shown in Table 5. We succeeded to create gamma ray source file for simulation.

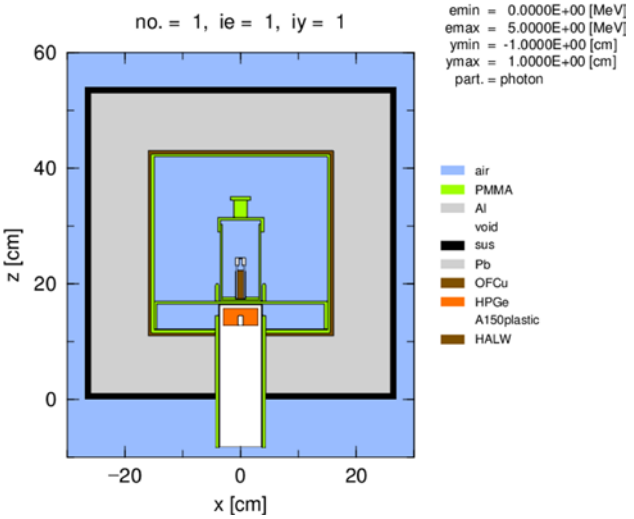

Figure 8: Model of the measurement chambe

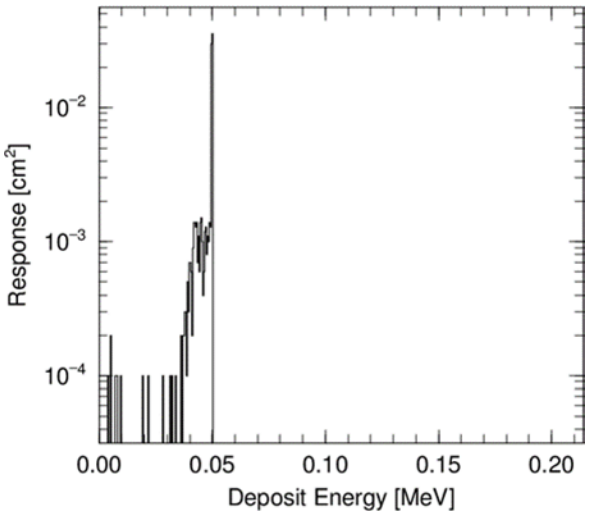

Figure 9: Case of the absolute detection efficiency of 50 [keV]

Nucleus	Energy [keV]	net counts	Absolute detection efficiency (PHITS) [deposit/source]	Sample bottle [count/ml]	Measurement time[s]	Number of disintegrations [Bq/ml]	Number of disintegrations Bq(V35)
241Am(Ci)	59.54	8.23E+06	6.084E-02	1.352E+08	5.615E+04	2.41E+07	1.85E+15
154Eu(Ci)	123.07	6.48E+06	5.785E-02	1.120E+08	5.615E+04	1.99E+07	1.53E+15
134Cs(Ci)	604.80	1.00E+05	1.432E-02	6.983E+06	5.615E+04	1.24E+06	9.56E+13
137Cs(Ci)	661.66	2.94E+08	1.343E-02	2.191E+10	5.615E+04	3.90E+09	3.00E+17
134Cs(Ci)	795.95	7.77E+04	1.144E-02	6.794E+06	5.615E+04	1.21E+06	9.31E+13

Table.4: Net counts, absolute detection efficiency, total gamma ray amounts at V35 tank

Nucleus	Evaluation value [Ci]	ORIGEN calculation value [Ci]	Analytical value [Ci]
241Am(Ci)	1.85E+15	4.40E+15	1.31E+15
154Eu(Ci)	1.53E+15	5.03E+15	-
134Cs(Ci)	9.56E+13	1.61E+14	-
137Cs(Ci)	3.00E+17	2.66E+17	6.23E+16
134Cs(Ci)	9.31E+13	1.61E+14	-

Table. 5: Evaluated absolute gamma-ray quantity, ORIGEN and analysis value

5. Results of gamma and neutron measurements on the outside surface of HALW cell

5.1 Experimental setting

The gamma-ray spectrum and neutron flux were measured outside of the concrete cell. Figure 10 shows the measurement point for the gamma-ray spectrum and neutron measurements. We chose two tanks (these call for V35, V36) for these measurements. V36 tank has only nitric acid and is a spare tank. The result from V36 was compared to the other results. V35 tank has HALW. Figure11 shows measurement setup outside the concrete cell. There is 1.9 m thickness concrete between detector and HALW tank in outside wall of HALW cell measurement. The largest solid angle point was selected for measurement point that is the same level of HALW tank liquid height.

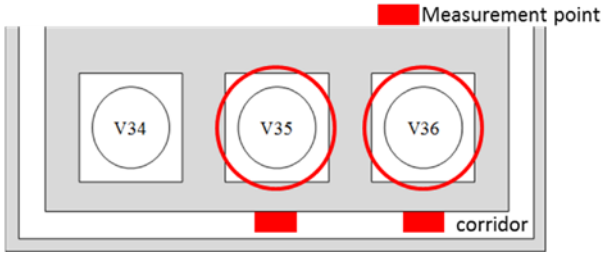

Figure 10: Measurement point (floor plan)

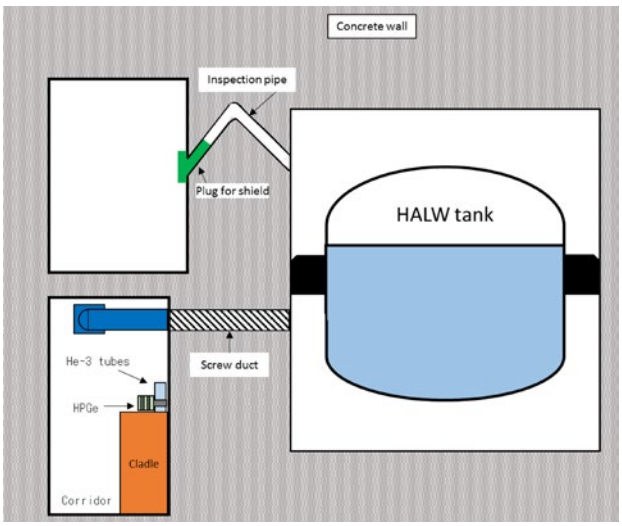

Figure 11: Measurement setup (cross section view)

Two detectors were used for the gamma-ray and neutron measurements. One was HPGe [GMX50-83-A ORTEC] for gamma-ray measurements and its energy range was up to 10 MeV. The other was six He-3 tubes in high density polyethylene to measure neutrons (singles rate). Figure 12 and 13 show the HPGe and six He-3 tubes detector setup[6].

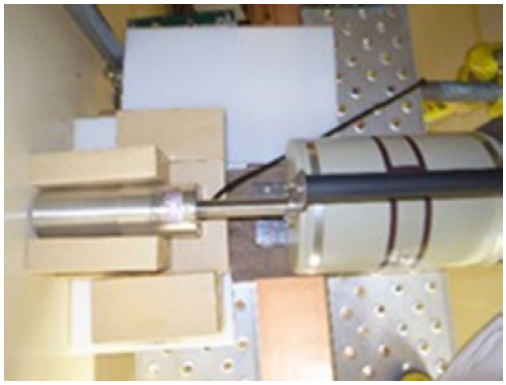

Figure 12: HPGe

Figure 13: Six He-3 tubes

5.2 Result of gamma-ray measurement

Regarding to HPGe measurement, we could find only background peaks. It was determined that the 1.9 m concreate was too thick to detect gamma-ray emitted from HALW tank and Pu monitoring of by gamma rays measurement outside of the cell cannot be conducted. Measurements should be conducted at points with less shielding such as inside penetration pipe or cell.

5.3 Result of neutron measurement

Figure 14 shows the results from the neutron measurement. The horizontal axis shows the measurement cycle number (1cycle means 1minute measurement) and the vertical axis shows neutron signal cps.Each point corresponds to the neutron count rate in each cycle. The solid lines show mean value of same color points, respectively. As you can see in Fig. 14, the neutron response in front of V35 was slightly higher than that of V36. Although this may indicate that we might be able to detect neutrons emitted from HALW tank outside cell which has 1.9 m thick concrete, these value is insufficient for Pu monitoring because the mean value of V35 was less than 0.1 cps.

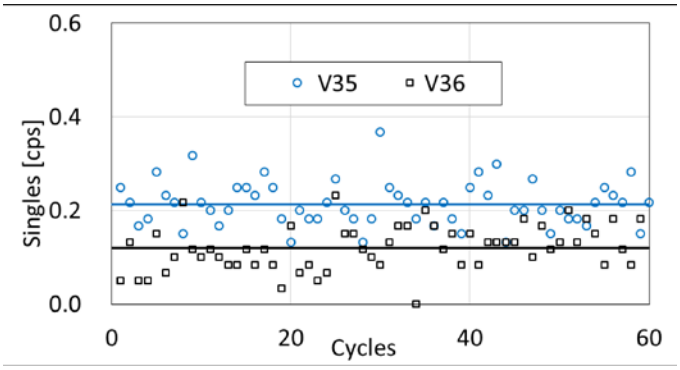

Figure 14: Result of neutron measurement.

5.4 Comparison with simulation results

Model [7]

Since Cm-244 is the dominant source of neutrons in the HALW, Cm-244 was used as the neutron source term [8] in the simulation. The input gamma ray source assumes gamma ray spectra measured with an HPGe detector multiplied by the efficiency curve calculated by PHITS code. The results described in section 3.2 and 4.2 were used as the radiation source files. We assumed the number of particles was 1 million. Dimensions and model used for the simulation are shown in Fig. 15. Radiation that passes through from the concrete cell were simulated at the floor of the 1st floor and 3.28 [m] and 1.52 m from the floor of the basement. The screw duct is depicted in Fig. 16.

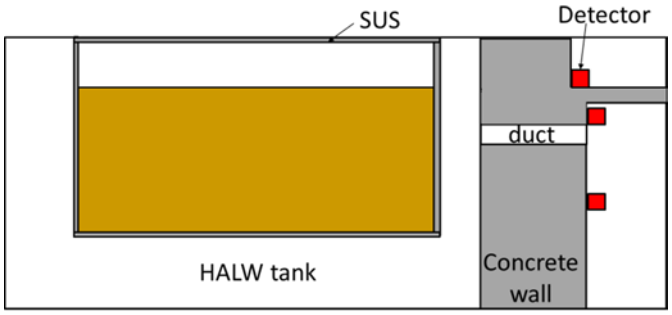

Figyre 15: Model of whole HALW tank(V35)

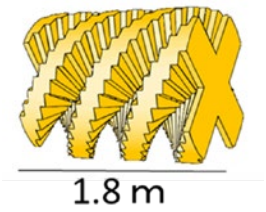

Figure 16: Structure of screw duct

Results

Gamma rays were simulated using the gamma ray destructive analysis (DA) spectrum from the measurement of the diluted HALW sample as an input file (see Fig. 17). We understood that gamma rays were almost completely shielded about 70 cm away from the inner wall. Based on the results of PHITS simulation using DA data as the input file, it seems difficult to measure gamma rays directly from the HAW tank at the outside of the concrete cell as same as measured gamma and neutron results.

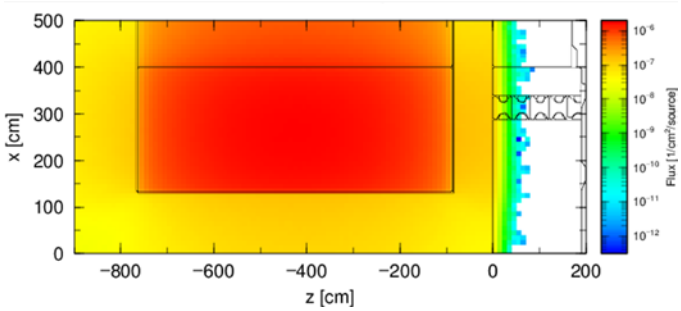

Figure 17: Gamma rays simulated using gamma ray analysis data as an input file

The neutron distribution was simulated using the neutron analysis data as an input file (see Fig. 18). Scattered neutrons were detected at 3.28 m from the basement floor based on simulation as shown in Fig. 18. We assumed that radiation could be scattered because of the structure of screw duct as shown in Fig. 16. There was no neutron detection at 1.52 m from the basement floor based on the simulation results. Regarding the difference between 5.3 Fig.14 neutron measurements and the simulations, the simulation could not help explain the different results.

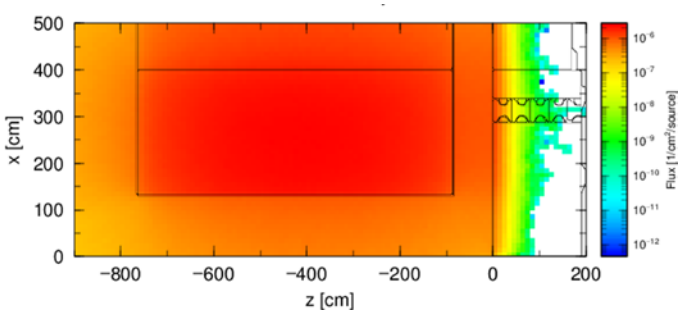

Figure 18: Neutron distribution simulated using neutron analysis data as an input file

6. Conclusion

A project of development of a new technique to monitor Pu with FP has been carried out since 2015 as scheduled. As the first step, analysis of the HALW to evaluate neutron/gamma-ray emitted from solution in the HALW tank (V35) which has the highest Pu concentration in HALW tank at TRP were conducted. Gamma-ray spectrum and neutrons emitted from 1mL HALW sample which was diluted with nitric acid of same acid concentration to 10000 was measured. Based on the HPGe analytical results, the absolute gamma-ray value was

evaluated with absolute detection efficiency calculated by PHITS and gamma-ray spectrum for the input source file.

We performed actual measurements of gamma rays and neutrons at the outside of the concrete cell. Gamma-ray peaks emitted from HALW solution were not found in measured spectrum because shielding effect of the HALW tank's cell which has 1.9 m thickness concreate was too high. So we try to conduct gamma-ray spectrum measurement at the inside the cell which is less shielding effect than outside the cell. On the other hand, Neutron response proportional to neutron generation ratio in each HALW tank was obtained by neutron measurement at the outside of the cell wall. However, it will be also necessary to conduct neutron measurements inside the cell because differences of the mean value of neutron signal on each measurement was about 0.1 cps. It is not enough count ratio to evaluate the difference because sampling error from HALW tank also has about 1% and it include the result this time. According to the PHITS simulation, detection of gamma rays and neutrons at the outside of the concrete cell is difficult. On the other hand, they could be detected at the outside of the concrete cell near the duct at the basement floor.

For the next step, we will measure gamma rays and neutrons at the inside of the concrete cell.

7. Acknowledgements

This project is being carried out under the support of the Ministry of Education, Culture, Sports, Science and Technology (MEXT) of the Japanese government.

8. References

[1] "IAEA Department of Safeguards Long-Term R&D Plan, 2012-2023," STR-375, Vienna, January 2013,https://www.iaea.org/safeguards/symposium/2014/images/pdfs/STR_375 IAEA_Department_of_Safeguards_Long-Term_R%26D_Plan_2012-2023.pdf

[2] H. Nakamura, et al., "Development and future challenge for Advanced Solution Measurement and Monitoring System (ASMS)," 52nd INMM Annual Meeting Proceedings, California, July 17-21, (2011).

[3] H. Nakamura, et al., "Concept of a New GloveBox Cleanout Assistance Tool (BCAT) by using Distributed Source-Term Analysis (DSTA)", 51nd INMM annual meeting proceedings, July 2010. http://jolisfukyu.tokai-sc.jaea.go.jp/fukyu/gihou/pdf2/n16-11.pdf

[5] T. Matsuki, et al., "Feasibility Study of Technology for Pu Solution Monitoring including FP – Composition Research of High Active Liquid Waste and Radiation Measurement Results on the Surface of Cell-", INMM Annual Meeting Proceedings. INMM-57 California.

[6] M. Sekine, et, all, Feasibility Study of Technology for Pu Solution Monitoring including FP -Overview and Research Plan- , Proc. INMM-57.

[7] J.M. Verbake, C. Hangmann, D. Wright, "Simulation of Neutron and Gamma Ray Emission from Fission," UCRL-AR-228518, Lawrence Livermore National Laboratory (2009).

[8] T. Sato, K. Niita, N. Matsuda, S. Hashimoto, Y. Iwamoto, S. Noda, T. Ogawa, H. Iwase, H. Nakashima, T. Fukahori, K. Okumura, T. Kai, S. Chiba, T. Furuta and L. Sihver, "Particle and Heavy Ion Transport Code System PHITS, Version 2.52," J. Nucl. Sci. Technol. 50:9, 913-923 (2013).

KJ-BB-18-055-EN-N